5.0 INTENSIVE CHEMICAL MEASUREMENTS AT HORSE POOL

James M. Roberts[1], Patrick R. Veres[1,2], Bin Yuan[1,2,] Carsten Warneke[1,2], Felix Geiger[3], Peter M. Edwards[1,2,] Robert Wild[1,2], William Dube[1,2], Gabrielle Petron[4], Jonathan Kofler[4], Andreas Zahn[3], Steven S. Brown[1], Martin Graus[1,2], Jessica Gilman[1,2], Brian Lerner[1,2], Jeff Peischl[1,2], Joost A. de Gouw[1,2], Rui Li[1,2], Timothy Bates[5], Patricia Quinn[5], Abigail Koss[1,2], Shao-Meng Li[6], David D. Parrish[1,2], Christoph J. Senff[1], Andrew O. Langford[1], Robert Banta[1], Randall Martin[7], Robert Zamora[8], Shane Murphy[9], Jeff Soltis[9], Robert Field[9]

1. Chemical Sciences Division, NOAA Earth System Research Laboratory, Boulder, CO.,
2. Cooperative Institute for Research in the Environmental Sciences, NOAA and University of Colorado, Boulder, CO.
3. Karlsruhe Institute of Technology, IMK-ASF, Karlsruhe, Germany
4. Global Monitoring Division, NOAA Earth System Research Laboratory, Boulder, CO.,
5. NOAA Pacific Marine Environmental Laboratory, Seattle, WA.
6. Environment Canada, Toronto, Canada
7. Department of Civil and Environmental Engineering, Utah State University, Logan, UT.
8. Physical Sciences Division, NOAA Earth System Research Laboratory, Boulder, CO.,
9. Department of Atmospheric Sciences, University of Wyoming, Laramie, WY.

5.1 Introduction and Background

The UBOS 2012 intensive campaign at the Horse Pool site took place under anomalous conditions of no snow cover, higher than normal temperatures, and no 'cold pool' events. As such, the 2012 data are most useful for source characterization, and as indicators of slow photochemistry typical of wintertime North America. The 2012 study represented a significant effort, including several groups that provided complementary measurements. The 2013 study plan was formulated so that the intensive measurements would only be deployed if and when high O_3 conditions were established. Because of this contingency, and owing to substantial field commitments later in the year by a number of groups including NOAA/CSD, the 2013 effort was smaller and more focused. The 2013 study concentrated on photochemical radical sources, associated photochemical marker species, and snow chemistry. By mid-January 2013, it was clear that conditions would be conducive to high ozone events, and the decision was made to deploy the Horse Pool intensive measurements. The results of those measurements are described in this section. As will be shown, much can be learned by contrasting the 2012 and 2013 results, as they indicate both the differences in magnitude of O_3 and radical sources, large differences in the associated photochemical product species, and the presence of a snow layer that contained high levels of deposited material.

5.2 Site Configuration and Experimental Approach

The UBOS 2013 campaign was conducted between Jan 23 and Feb 21 at the same location as the 2012 Horse Pool Intensive study. Figure 5-1 shows a photograph of the site as it was configured in 2013. The Lidar and PMEL aerosol vans were deployed essentially as they were in

2012, and the main differences were in how the gas phase measurements were configured. Most of the inlets for gas phase measurements were fixed to a moveable carriage, on the sampling tower shown in Figure 5-1, which was switched from 1m to 7.25 m above ground level (agl) every 20 minutes, for approximately 8 days during the project. Several of the instruments that had unique inlet requirements, such as the NO_3, N_2O_5 and NOy CaRD instruments used inlets that were fixed at approximately 4 m agl. The ground south and west of the tower was cordoned off to provide as natural a snow surface as possible, however servicing of the inlets did disturb the area immediately around the base of the tower somewhat. The south and west sectors were kept clear as those were the most common daytime prevailing wind sectors during the 2012 study.

The measurements deployed during the 2013 Horse Pool intensive study are listed in Tables 5-1 and 5-2. Where noted, some of the measurement methods were identical to those fielded in 2012 [*J.M. Roberts et al.*, 2013] and will not be discussed in detail here. New measurements or aspects of measurements that differed from the 2012 Study will be detailed below.

5.2.1 NO/NO_2/NOy/O_3/NO_3/N_2O_5 by Cavity Ring-Down Spectroscopy

The measurement techniques for nitrogen oxides were very similar to those used in the 2012 UBOS study, and only significant differences will be noted below. The nighttime nitrogen oxides, NO_3 and N_2O_5, were measured using a custom-built cavity ring-down spectrometer (CaRDS), the working principles of which are described in detail in the 2012 report. Only the inlet configuration was a noteworthy difference, and is discussed here. The inlet for this instrument consisted of a 1/4" O.D. teflon tube that was extended about 1 meter above the roof of the trailer, 4 m agl total. Since aerosol accumulating inside this tube can decrease inlet transmission for NO_3 and N_2O_5 [*Fuchs*, 2008], the inlet was replaced with a clean tube on a daily basis. To measure the extent of these losses, inlet transmission comparisons were made between day-old and new tubing using a synthetic crystalline N_2O_5 sample stored on dry ice. A constant flow of clean air over the sample produced a constant gas-phase output of N_2O_5. The comparison between measurement through old and new tubing showed an average 8% decrease in N_2O_5 transmission efficiency over one day of use.

A separate CaRDS instrument was used to measure NO_2, NO, NO_y, and O_3, also based on the same principles of the instrument described in 2012. It measures the concentration of NO_2 in four 50 cm optical cavities and after quantitative conversion of either NO (by reaction with excess O_3) or O_3 (by reaction with excess NO) in two of them. This instrument sampled from a fast-flow inlet attached to the moving carriage on the tower. The main difference between the 2012 and 2013 versions is the addition of a fourth channel that measures total NO_y. A quartz oven heated to 650° C serves as the inlet, with roughly 3 mm of quartz extending out of the heated metal enclosure. This ensures that the front end of the inlet stays above 100° C, minimizing losses of HNO_3 to the inlet walls. The oven temperature was chosen such that the NO_y compounds are thermally dissociated to NO and NO_2 without the need for catalytic conversion [Wild et al., 2013 in preparation, [*Day et al.*, 2002]. The addition of excess O_3, as in the channel that measures total NO_x, ensures that any NO is converted to NO_2.

One inadvertent effect of the NOy conversion oven was the creation of semi-volatile organic compounds from VOCs in ambient air. This material coated the high-reflectivity mirrors enough to cause severe degradation of the ring-down time constant. To counteract this, we installed a hydrocarbon "kicker," a tube which is permeable to hydrocarbons but impermeable to NO_x [Thermo Electron Corporation], in between the oven and the optical cavity. A sheath counter-flow transported the hydrocarbons out an exhaust line.

The NO_2 channels were calibrated as in 2012, resulting in ±3% accuracy for NO_2 and O_3, and ±5% for NO_x. We conservatively claim an accuracy for NO_y of ±10%, due to difficulty in calibrating conversion efficiencies of our heated inlet, as well as a small but non-negligible interference from NH_3. The accuracies for the NO_3 and N_2O_5 measurements are 15%, in part due to the uncertainty in determining inlet losses.

5.2.2 O_3 and Winds by Lidar

NOAA/ESRL/CSD deployed two of its lidar remote sensing instruments to the 2012 and 2013 Uintah Basin Ozone Studies (UBOS): the High Resolution Doppler Lidar (HRDL) and the Tunable Optical Profiler for Aerosol and oZone (TOPAZ) lidar. Both instruments were situated at the Horse Pool site.

5.2.2.1 HRDL Doppler Wind Lidar

HRDL provided profiles of horizontal wind speed and direction, horizontal wind speed variance, vertical wind speed and its variance and skewness, and un-calibrated aerosol backscatter at a time resolution of 20 minutes. Profiles of horizontal wind speed and its variance, wind direction, and un-calibrated aerosol backscatter retrieved with HRDL in scanning mode are measured to within 5 meters of the surface and with 5-meter vertical resolution. The maximum range of the HRDL measurements depends on atmospheric aerosol loading, and the presence of clouds, fog, and precipitation. Technical specifications of HRDL are given in Table 5-3, including 30-m range resolution, a minimum range of 190 m, a maximum range of 3-4 km, rms velocity precision of less than 20 cm s^{-1}, and azimuth-elevation scanning capability covering more than a hemisphere, because of HRDL's ability to scan to negative elevation angles. Full 360° scans in azimuth at fixed elevation provide data over a cone in the atmosphere, whereas scanning in elevation provides data over a vertical cross section or vertical slice of atmosphere. The scan data are analyzed and averaged over vertical intervals Δz and time intervals Δt to generate mean vertical profiles of the horizontal wind from near the surface to 1½ -2 km above ground, where the analyzed Δz near the surface is <5 m and the instrument precision of the *mean* wind speeds becomes <5 cm s^{-1}. For this project a scan sequence of 20 min allowed a variety of scans (conical, vertical slice, vertical staring) to be performed, so wind-profile data are available at 20-min intervals, as shown in Figure 5-2. The profiles in Figure 5-2 were composited from a sequence of 4 conical scans at 1°, 3°, 15° and 30° elevation angles. Preliminary HRDL data were posted in near real time (about 10 minutes after they were recorded) on a web site, where they were available for other study participant to use in the interpretation of their data and to plan the UBOS flight operations. Details about the HRDL instrument are given in Table 5-3 and descriptions of the retrievals of the various data products can be found in Grund et al. (2001) and Tucker et al. (2009).

5.2.2.2 TOPAZ Ozone Lidar

The TOPAZ lidar measured vertical profiles of ozone and aerosol backscatter from near the surface up to a few kilometers AGL. TOPAZ is based on a state-of-the-art, solid state, tunable laser that emits laser pulses in the ultraviolet spectrum at three wavelengths between 285 and 300 nm [*Alvarez II et al.*, 2011]. Prior to the UBOS 2012 study, TOPAZ was converted from a downward-looking airborne system into a zenith-pointing instrument that was installed into a truck with a roof-mounted two-axis scanner (Fig 3.3). The scanner permits pointing of the laser beam at several shallow elevation angles at a fixed but changeable azimuth angle. Zenith operation is achieved by moving the scanner mirror out of the laser beam path. During the UBOS studies, repeated scans at 2, 6 (2013 only), 10, and 90 degrees elevation angle were performed approximately every 5 minutes. The dwell time at each angle was 75 seconds. The ozone and aerosol backscatter profiles from the various elevation angles were spliced together to create composite vertical profiles extending from 15 m up to about 3 km AGL. The effective vertical resolution of the composite ozone profiles increases with altitude from 3 to 90 m. The ozone and aerosol profiles were reported at time resolutions of 5-15 minutes. Similar to HRDL the maximum range of the TOPAZ measurements is affected by clouds, fog, and precipitation. The airborne version of TOPAZ has been used in several air quality field campaigns since 2006 and has been extensively tested and compared with collocated in situ ozone sensors [*Langford et al.*, 2011; *Senff et al.*, 2010]. Details about the new, truck-mounted version of the TOPAZ lidar can be found in Alvarez et al. (2012).

5.2.3 CH_4, CO_2, H_2S by Integrated Cavity Output Spectroscopy

These species were measured using two different commercial systems (Picarro Instruments): a combination CH_4/H_2S instrument fielded in conjunction with the University of Wyoming; and a combination CH_4/CO_2 instrument fielded in conjunction with NOAA/GMD. The two instruments had approximately 7 days of overlap during which they compared favorably (to with-in their stated uncertainties). While the time resolution of these instruments was nominally 2 seconds, the measurements were averaged and archived as one minute averages. Higher time resolution data are available on request. The inlet for the CH_4/H_2S instrument was connected to the fast flow inlet used by the VOC instruments. The inlet for the CH_4/CO_2 instrument was connected to the same high flow inlet that the $NO/NO_2/O_3$ instrument used and so was raised and lowered as part of the tower experiment. The over-all uncertainties were (1% + 4 ppbv), (1% + 2ppbv) for the CH_4 channels that were part of the H_2S and CO_2 instruments, respectively, (0.4% + 3ppbv) for the H_2S channel, and (1% + 0.2 ppmv) for the CO_2 channel of each instrument.

5.2.4 SO_2 by UV Fluorescence

Sulfur dioxide was measured with a modified Model TEII 43s commercial instrument that operates on the principle of pulsed UV fluorescence. Modifications centered around shortening the response time by increasing the sample flow rate. The overall uncertainties in the measurement were ±(15% + 0.15ppbv).

5.2.5 Acyl Peroxynitrates/Nitryl Chloride

Measurements of acyl peroxy nitrates ($RC(O)OONO_2$) and nitryl chloride ($ClNO_2$) were acquired with the same chemical ionization mass spectrometric technique use during the 2012 study. The GC/ECD system used in 2012 was not fielded during the 2013 campaign. The inlet used for this measurement was the same configuration as 2012 and placed on the moveable carriage on the sampling tower. Calibrations of PAN (acetyl peroxynitrate = $CH_3C(O)OONO_2$) and $ClNO_2$ and inlet tests were performed in the manner as 2012, and the results of these inlet tests were used to correct the ambient data. Additional calibration efforts were done for PPN (propionyl peroxynitrate = $CH_3CH_2C(O)OONO_2$), APAN (acrylyl peroxynitrate = $CH_2CHC(O)OONO_2$), MPAN (methacrylyl peroxynitrate = $CH_2C(CH_3)C(O)OONO_2$) and CPAN (crotonyl peroxynitrate = $CH_3CHCHC(O)OONO_2$) so those species were also reported (the sum of MPAN and CPAN were reported as MPAN because they appear at the same mass). The overall uncertainties of these measurements were ±(20% + 25pptv) for $ClNO_2$, ±(15%+ 5pptv) for PAN, ±(20% + 5 pptv) for PPN, ±(20% + 5 pptv) for APAN, and ±(20% + 5 pptv) for CPAN + MPAN.

5.2.6 VOCs by PTRMS

Two proton-transfer-reaction time-of-flight mass spectrometers were deployed at the Horse Pool site during UBOS 2013, the same quadrupole-based PTR-MS deployed during the 2012 intensive, and a new instrument based on a time-of-flight mass spectrometer (PTR-TOF-MS), owned by the University of Wyoming and jointly operated with the Chemical Sciences Division (CSD) of NOAA. The PTR-TOF-MS instrument was deployed in parallel with a PTR-MS instrument operated by CSD of NOAA in order to enhance the amount of high resolution volatile organic compound (VOC) data collected as well as to validate this relatively new VOC measurement technique. Throughout the duration of the measurements, the PTR-MS and PTR-TOF-MS instruments both sampled from the same inlet manifold and were operated under similar conditions. The methods for the CSD PTR-MS were essentially the same as in 2012 and so will not be discussed in detail here, instead the following description will focus on the new instrument.

The principal of the PTR-TOF-MS is identical to that of PTR-MS with the exception of the mass spectrometric technique utilized and is described in detail elsewhere [Graus et al. 2010, and references therein]. Briefly, H_3O^+ is produced in a hollow cathode ion source and allowed to react with VOC that have a higher proton affinity (PA) than H_2O in a reaction chamber. The resulting $VOC{\bullet}H^+$ ions are detected together with the primary ions using a mass spectrometer, either a quadrupole in the PTR-MS or a time-of-flight in the PTR-TOF-MS. Compounds that are detected at high sensitivity with these techniques are oxygenates, aromatics, nitriles and alkenes. Alkanes are typically undetectable using the PTR chemistry, as the driving chemistry is relatively insensitive to this class of compounds. The time-of-flight mass spectrometer acquires full mass spectra on a sub 10-Hz timescale with a high degree of mass resolution. This allows for monitoring of all detectable species, both known and unknown, on a higher time resolution and sensitivity than the standard PTR-MS with quadrupole mass spectrometric detection. Mass detection with PTR-TOF-MS is accurate to 40 parts-per-million by mass (0.004 amu for a mass of 100 amu) whereas the standard quadrupole mass spectrometer used in PTR-MS can only obtain unit mass resolution. As such, the PTR-TOF-MS has the ability to distinguish between isobaric

compounds (e.g. compounds with the same nominal mass but different molecular formulas). One example of this is the successful separation of isoprene (C_5H_8, mass = 68.1170) and furan (C_4H_4O, mass = 68.0740) with PTR-TOF-MS where this would be impossible using the standard PTR-MS instrument.

During the UBOS intensive period, continuous PTR-TOF-MS mass spectra were obtained ranging from m/z (i.e., amu) 10 – 500 and averaged such that the time resolution of the measurements was set to 10 seconds. Post-acquisition data analysis was performed according to procedures described elsewhere [*Müller et al.*, 2013]. VOC data are reported in parts-per-billion by volume (ppbv) when calibration data is available; otherwise normalized counts per second (ncps) are reported. In all, over 60 masses and corresponding molecular formulas are reported using the PTR-TOF-MS data collected during the UBOS 2013 intensive period.

5.2.7 C_2-C_{10} HCs by GC-FID

A total of 17 volatile organic compounds (VOCs) were measured in-situ by a research-quality, single channel, gas chromatograph-flame ionization detector. The inlet for the GC-FID consisted of a 15m unheated Teflon line (0.25inch o.d. standard wall), which was positioned on a tower at the same location as other VOC instrument inlets. The inlets were attached to a movable platform that sampled between 1 and 7.25m above ground level. Ambient air was pulled continuously at a rate of approximately 5L min-1, resulting in an inlet residence time of less than 15 seconds. From this high-flow sample stream, a smaller sample flow was diverted through water and carbon dioxide traps and into a cryogenic trap for five minutes. For each sample, this smaller flow was adjusted between 10 and 70 sccm to adapt to wide variations in ambient hydrocarbon concentrations. After the five minute sample acquisition period, the analysis sequence was begun by flash heating the cryogenic trap from -160 to 110°C, injecting the sample onto a 50m Al2O3/KCl PLOT column. The column was then ramped from 75 to 200°C over 12 minutes in order to separate C2 to C6 hydrocarbons. The eluent was analyzed by flame ionization detection, which sensitively detects hydrocarbons. The sample collection (5min) and analysis sequence (25 min) repeated automatically every 30 min beginning on the hour and half-hour. The accuracy and precision were dependent on compound and sample flow rate, but were generally <20% and <5%. The GC-FID was extensively calibrated during- and post-campaign using nine individual calibration mixtures ranging from 0 to 1000ppbv. Cross-calibrations were conducted with the INSTAAR GC-MS used during the 2013 Horse Pool measurements, and the NOAA GC-MS used during the 2012 Horse Pool measurements, to ensure valid measurement comparisons.

5.2.8 Carbonyls Measured by DNPH Cartridges

For comparison with datasets collected by other investigators and to get a measure of potential Basin-wide distributions, personnel from Utah State University also measured concentrations of ambient, low molecular carbonyl compounds by collection onto commercially-purchased dintrophenylhydrazine (DNPH)-coated cartridges (Supelco, LpDNPH S10L) at Roosevelt and Vernal. The collected samples were transported to USU's Utah Water Research Laboratory (UWRL) and analyzed using high performance liquid chromatography (HPLC) following the general protocols outlined in EPA Compendium Method TO-11A [*EPA*, 1999]. TO-11A

commercially-purchased standards, and associated dilutions, were used for HPLC peak identification and quantification. Field blanks were taken once per day, and laboratory blanks and spiked samples were also analyzed.

These samples were collected from Feb. 13-25, 2013, a period in which a strong inversion and ozone buildup was observed (~130 ppb O_3), followed by a partial Basin washout during the evening of Sunday, Feb. 18th, followed by a moderate O_3 buildup (~115 ppb O_3) until the end of the overall study period. The samples at Roosevelt were collected three times per day over two hour periods (8:00-10:00, 11:00-13:00, and 14:00-16:00) using a Tisch Environmental Model 423, 3-Channel Carbonyl Sampler. The samples at Vernal were collected nominally twice per day (8:00-10:00 and 11:00-13:00) using an assembled system consisting of ¼" Teflon tubes, a mass flow controller (Cole-Parmer EW-32907-69), a vacuum pump, and a digital timer. After each 2-hr sampling period at Vernal the DNPH cartridges were manually changed. On occasion, as the opportunity presented itself, additional 2-hr samples were also obtained from the Vernal location. The Tisch system and the mass flow controller used at Vernal were calibrated prior to field deployment and sampled at a nominal flow rate of 1.0 Lpm. To guard against unwanted ozone interferences, KI scrubbers preceded each of the DNPH cartridges and were replaced approximately half way through the sampling period. Additionally, a 47 mm Teflon filter and Teflon filter housing were used at the ambient inlets to the system to protect against particle collection onto the DNPH cartridges.

5.2.9 Acids by NI-PT-CIMS

The NI-PT-CIMS fielded in 2013 is the same as the instrument fielded in 2012, with only minor changes. The instrument was connected to the same high flow inlet that supplied the PTR-MSs and GC/FID, which consisted of a 3/8"O.D. PFA tube, thermostated at 35C, and operated at a total flow rate of 20 SLPM. A smaller flow (800 SCCM) was sampled off of that into the Acid CIMS. Zeroing was accomplished by periodically switching a carbonate denuder/catalyst system inline that removed all acids, including HCl. Calibrations were performed routinely for formic acid and before and after the project for the other acids. The exception to that was a series mid-project calibration and inlet tests for HONO that confirmed the HONO response characteristics of the instrument. A series of inlet test were performed with NO_2 and H_2O to determine the presence and magnitude of any inlet production of HONO from those species. The results of those tests were consistent with previous tests [*J. M. Roberts et al.*, 2010; *VandenBoer et al.*, 2013] and confirmed that NO_2 could produce at most a 5% interference in HONO measurements. It should be noted that in contrast to many urban areas, ambient NO_2 levels were quite modest on average (4.3 ±4ppbv) and the HONO/NO_2 values measured in this study were quite high (0.21 ±0.3). Tests of another potential interfering agent, peroxynitric acid (HO_2NO_2), were performed in the laboratory after the experiment and qualitatively indicated that HO_2NO_2could produce a positive interference in the detection of HONO by this method. The precise magnitude of this interference was not yet been determined.

5.2.10 Aerosol Particle and Snow Measurements

5.2.10.1 Aerosol Measurements – NOAA/PMEL

The sampling methods and protocols for the aerosol measurements made in 2013 were essentially the same as for the 2012 intensive, and many of the details of those measurements have been described previously [*Bates et al.*, 2008]. The only significant differences was that the average temperature and RH in the sample line measured downstream of the impactors was 24.3 ± 1.9°C and 10.3 ± 3.9%, respectively in 2012 and 23.7 ± 2.6°C and 8.8 ± 3.4% in 2013.

5.2.10.2 Snow Sampling

Snow samples were collected 2 or 3 times per day during the project. Snow samples were collected in 1 L glass mason jars that had been pre-rinsed in deionized water. The snow samples (0-3cm depth) were collected from undisturbed snow at a number of sites, all within 1.3 km of the Horse Pool site. During each snow sample collection, 2 to 6 jars of snow were collected. Each sampling set included at least two samples from the top 3 cm of the snow surface. The snow was kept frozen until melting and filtering, generally 1 to 18 hours after collection. The snow was melted in a microwave oven over a period of a few minutes and the melt water was immediately filtered through a 25 mm diameter 0.4 um pore size nucleopore filter. The filtrate volume was measured and an aliquot of filtrate was collected for analysis for major ions by ion chromatography (IC). Aliquots of the filtrate were also collected in glass sample jars for TOC analysis and UV-Vis analysis. The filters were dried and stored in a freezer.

5.2.10.3 Snow Analysis

TOC/TON – Filtered snow samples were acidified with hydrochloric acid (HCl) to a pH less than 2, stored in pre-cleaned glass vials and refrigerated until analysis. Samples were analyzed for total organic carbon (TOC) and total nitrogen (TN) with a Shimadzu TOC-VCSH instrument with a TNM-1 nitrogen unit. A solution of hydrogen potassium phthalate as a carbon standard and potassium nitrate (KNO_3) as a nitrogen standard, acidified to a pH of 2, was used to generate five point calibration curves for both TOC and TN with an R^2 greater than 0.99. The instrumental method has an uncertainty of ±0.06 ppm for TOC and ±0.02 ppm for TN. The precision for these measurements was less than 2% for both measurements. A 3 ml aliquot of each sample was loaded into the instrument and sparged with zero air to remove any CO_2. Finally, 150µl was injected into the heated platinum combustion tube. The best three of five injections were averaged to obtain the final TOC and TN concentrations.

Anions and Cations – Filtered snow samples were injected directly into the ion chromatographs used for ambient aerosol sample analysis (section 3 above). The IC analysis was generally done within 48 hours of snow sample collection.

Light absorbing carbon – The transmittance spectrum of each filter was measured in an integrating-sandwich spectrophotometer that incorporates an integrating sphere as one side of the sandwich (ISSW;[*Grenfell et al.*, 2011]). The integrating-sandwich configuration is designed to minimize the effect of scattering by the aerosols on the filter, so that the measured signal is a function only of the losses due to light absorption. A set of standard filters containing known (weighed) amounts of BC in the form of Monarch-71 soot was used to calibrate the system for

conversion from measured signal to black carbon loading (μgC/cm^2 on the filter). The calibration standards were pre-filtered to produce a size distribution generally representative of atmospheric BC (0.4 μm mass mean diameter).

5.2.11 Ammonia Measurements

Ammonia measurements were made in the Uinta Basin, by the Randall Martin group at Utah State University, at several sites during the 2013 intensive. These measurements are presented in this section since they are most effectively interpreted and are most applicable in the context of detailed aerosol composition measurements as were made at the Horse Pool site.

Previous measurements identified ammonium nitrate (NH_4NO_3) and ammonium sulfate ($[NH_4]_2SO_4$) as significant contributors to the particulate mass, specifically $PM_{2.5}$, as measured at several locations throughout the Uinta Basin [*Martin et al.*, 2011; *UBWOS*, 2013]. As such, it became of interest to assess the availability of ambient gas-phase ammonia (NH_3) within the Basin for potential reaction with nitrate and sulfate species resulting on secondary particle formation.

Ogawa passive samplers (Ogawa USA, Inc., Pompano Beach, Florida) were used to determine time-averaged concentrations of ambient NH_3 at four locations: Horse Pool, Ouray National Wildlife Refuge, Roosevelt, Vernal, and Redwash. It should be noted that Horse Pool site was the location of the multi-group intensive photochemistry study for both 2012 and 2013.

The Ogawa samplers consist of a solid Teflon cylinder with two open, but sample-isolated ends, each containing a reactive glass fiber substrate impregnated with citric acid. The substrate is mounted between two stainless steel screens situated behind a diffusion-barrier end-cap containing 25 holes (open area of 0.785 cm^2). Absorption substrates can be placed in both ends for the purpose of replication, which was utilized during this study. The passive samples are more completely described in Roadman et al. (2003) and Reese (2009).

Prior to deployment, the samplers were prepared by placing a commercially-purchased, coated substrate in each end of the sampler. Once loaded, the samplers were stored in individual air-tight plastic bags inside individual, air-tight, screw-top brown vials until deployment at the sampling locations. During the sampling period, the samplers were attached to associated support clips and then covered by a cap to protect the sampler from rain, dust, and wind. Figure 5-4 shows the passive sampler in place without and with the protective cap (the latter at the Redwash site). Following the sampling periods, the total deployment time was noted and the samplers were returned to the plastic bags and vials and were stored under dark, refrigerated conditions until transfer to the Utah Water Research Laboratory (UWRL) for quantification.

At the UWRL, the samples were recovered by placing the substrates in individual 30 ml sample vials and adding 8 ml of DDW (double-de-ionized water) to each vial. The vials were then placed on a sonicator for 10 minutes. Following sonication, 10 μg of 0.5 M hydrochloric acid (HCl) was added to each sample to make certain the ionic ammonium form was maintained in the aqueous solution to prevent any re-volatilization and loss of the collected NH_3 from

solution. Four milliliters of sample solution was then filtered into IC vials for analysis using non-sterile syringes and 0.2 µm nylon filters.

Final quantification was performed via ion chromatography. The IC instrument (Dionex Corporation) was equipped with an AS 40 Automated Sampler, CE20 Conductivity Detector, GP 40 Gradient Pump, Membrane Suppressor, LC Chromatography Oven, IonPac® CS12A cation column, CG12A cation guard column, and a 500 µL sample loop. The IC method used for analysis of NH_4^+ had a 13-minute run time method and 0.03 M sulfuric acid (H_2SO_4) solution as eluent. IC standards were prepared with 0.0745 g of powdered NH_4Cl and DDW to 250 ml, creating a 100 ppm solution. This stock 100 ppm solution was then used to create standards in steps of 0.1, 0.2, 0.4, 0.6, 0.8, and 1 ppm NH_4^+ concentration, which were then analyzed on the IC instrument to create the standard curve. DDW blanks and continuous calibration verification (CCV) standards were also analyzed systematically throughout sample analysis to help ensure quality control. Conversion of liquid NH_4^+ concentrations to ambient gas-phase NH_3 concentrations are fully described in Roadmen et al. (2003).

5.2.12 Mobile Lab Measurements from 2012

The UBOS 2012 study included a ground site at Horse Pool, Utah and the NOAA GMD mobile laboratory. The Horse Pool ground site was fully equipped with a large suite of gas phase and aerosol measurements and only the instruments used in this study are described here. VOC measurements were made using PTR-MS instruments: the NOAA PTR-MS, which is described in detail by de Gouw and Warneke (2007) and the Karlsruhe Institute of Technology (KIT) ULW-PTR-MS (ultra-light weight PTR-MS). PTR-MS is an on-line mass spectrometric technique for measuring VOCs in the atmosphere. In PTR-MS, H_3O^+ ions are used to ionize the compounds of interest in a reaction chamber and the primary and product ions are detected by a quadrupole mass spectrometer [*de Gouw and Warneke*, 2007]. The NOAA PTR-MS was deployed at the Horse Pool ground site for the duration of the study in January-February 2012, while the KIT PTR-MS was used at the ground site for the first three weeks for detailed comparisons and onboard the mobile laboratory for the next three weeks. The two PTR-MS instruments had similar reaction chambers and mass spectrometers, but the KIT ULW-PTR-MS was optimized for instrument size and weight and was 130 lbs compared to the standard PTR-MS, which is about 250 lbs. At the time of the study, the KIT ULW-PTRMS had a somewhat lower sensitivity of around 100-200 cps/ppbv compared to about 500-1000 cps/ppbv of the NOAA PTR-MS. After the study, the sensitivity of the KIT PTR-MS has improved by about a factor of 3. Calibrations were performed at the Horse Pool ground site every other day using a calibration standard that included 10 different VOCs including oxygenates, aromatics and other compounds, and the MOCCS [*Veres et al.*, 2010] system for formaldehyde. The measurements at the ground site are averaged to 1-minute data and the individual compounds on the mobile laboratory were measured for 0.5 seconds every 19 seconds.

At the ground site the two instruments used the same inlet, the same calibration set-up and were located in the same trailer. The two instruments agreed for all reported VOCs within 10%, which gives a good confidence for the comparison of the ground site data with the mobile laboratory data.

VOCs were also measured at Horse Pool using an on-line gas chromatograph-mass spectrometer (GC-MS). The GC-MS sampled air for 5 minutes every 30 minutes and measured among others speciated C_2-C_{12} alkanes, C_5-C_8 cycloalkanes, C_6-C_9 aromatics and methanol. The instrument is described in more detail elsewhere [*Gilman et al.*, 2010; *Gilman et al.*, 2013].

Methane was measured at Horse Pool using a 2-channel Picarro for CO_2 and methane and on the NOAA GMD mobile laboratory using a 4-channel Picarro for CO_2, CO, methane and water [*Petron et al.*, 2012].

5.2.13 Meteorological Measurements

NOAA/ESRL/Physical Sciences Division deployed an instrumented 20 m tower, ventilated broadband solar and IR Eppley radiometers, heated tipping bucket rain gage, snow depth sensor, and a bistatic acoustic sounder (3.4 m resolution, 6.0 m minimum range) at Horse Pool for both the 2012 and 2013 campaigns. The tower instrumentation included surface pressure, air temperature and relative humidity (2, 10, and 20 m), fast response sonic anemometer/ thermometer (6,16 m), wind speed and direction (10, 20 m). Soil moisture, soil heat flux and soil temperature at 5, 10, and 20 cm depths were observed during the 2013 field season.

Data from the standard meteorological instrumentation and radiometers were archived at 1.0 min intervals. The fast response anemometer/thermometers were sampled at 10.0 Hz. The raw 10.0 Hz samples were archived. Net radiative fluxes, turbulent heat fluxes and turbulent momentum fluxes were estimated using the radiometric and sonic anemometer/thermometer data sets. Jpeg images of the backscattered power measured by the sodar were generated at 30 minute intervals.

5.3 Results and Discussion

The results of the 2013 Horse Pool intensive measurements stand in stark contrast to those from the 2012 campaign. The 2013 intensive period was characterized by snow coverage and associated persistent cold pool periods lasting a week or more, during which O_3 built up to levels over 150 ppbv. The precursors of O_3, VOCs and NOx, showed contrasting behavior relative to 2012; primary VOCs and methanol were factors of 2-4 higher and secondary VOCs were often factors of 10 higher. NOx levels (NO + NO_2) were about the same, however NOx product compounds (e.g. PAN, HNO_3) were often 10 times higher in 2013. The solar actinic fluxes were about 50% higher in 2013 owing to the surface albedo being 85 to 95% in 2013 compared to the 2012 average of 35%. Radical sources driving O_3 production were dominated by unconventional sources: HONO and HCHO, with $ClNO_2$ and O_3 being only minor contributors. Formaldehyde appears to have both primary and secondary sources, and there is some question as to whether HCHO contaminated methanol usage in the Basin is an important source of primary HCHO. Measured HONO levels were quite high in 2013 relative to 2012 and had diurnal profiles that peaked around solar noon, implying a photochemical source. Vertical gradients in HONO implied that there was often a ground/snow source of HONO in the daytime and deposition at night.

The spatial and temporal variability of the ozone and associated cold pool conditions were measured by Lidar instruments during both the 2012 and 2013 campaigns. The results provide quantitative demonstration of the meteorological factors that produce a stable surface layer under cold pool conditions, and provide some guidance concerning the slow rate of transport within and at the margins of the Basin. Ozone vertical profiling was able to provide solid evidence that the NOx from the coal-fired Bonanza Power Plant power plant is lofted above the cold pool inversion and has an insignificant immediate contribution to NOx photochemistry in the Basin. Theoretically, eventual re-entrainment of some of the NOx from the power plant into the stable surface layer could occur but this is unlikely to be a significant factor under most circumstances associated with ozone episodes, at least over the first few days after emission.

Aerosol particle and snow measurements were made during the entire 2013 intensive. In general nitrate and organic carbon were the most abundant aerosol species by mass during the high ozone periods. Nitrate and nitrite built up in the top layers of the snow during the cold pool periods when ozone was building up. The large 'clean-out' event that occurred in the middle of the intensive period, that also involved some snow fall, brought in a cleaner top layer of snow, but was accompanied by deposition of soil-derived material, based on characteristic cations that are associated with soil. The snow also contained substantial black carbon that was deposited during cold pool conditions, hence was of local origin.

The following sections will provide the details of, and some conclusions about, the observations made at the Horse Pool site during the intensive period. Analyses are an on-going process and we expect to build on and refine these results in future publications.

5.3.1 Ozone and Odd-Nitrogen Species

Figure 5-5 shows the time series of the O_3 measurements during UBOS 2013 acquired with the CaRDS system. A Thermo Electron Corp, Model 42 O_3 UV-photometer was also run for much of the UBOS 2013 campaign, and agreed with the CaRDS instrument to within 2%. The CaRDS data will be used in the following discussions as it has better time resolution and precision. Both the diurnal variation and the larger-scale ozone events are clearly visible. 2013 was a high-ozone year, with 20 out of 28 days above the 75 ppbv National Ambient Air Quality Standards (NAAQS) for ozone, shown by the dotted line. Figure 5-6 compares the diurnal averages of O_3 during the campaigns in 2012 and 2013. The shaded background regions show approximate times of daylight. Not only are the O_3 levels significantly higher in 2013, but the daytime ozone production rates (measured from about 10am to 3pm) increased roughly threefold, going from approximately 2.4 ppbv/hr in 2012 to 7.1 ppbv/hr in 2013.

The comparison of O_3 distributions measured in 2012 versus 2013, shown in Figure 5-7, reveal some interesting contrasts. The 2012 O_3 measured at Horse Pool was most often below what would be considered a regional background for this season (45 ppbv or so), due to titration by NO_x species and deposition of O_3 and NO_y species (i.e., N_2O_5). The 2013 O_3 distribution observed in 2013 was quite different, with half of the measurements above the 75 ppbv NAAQS, and minimum values of 25-30ppbv, indicated a much reduced role for titration and deposition.

The distributions of odd-nitrogen species also showed marked differences between 2012 and 2013. The distributions of total NO_y, NO_x, and the ratio NO_x/NO_y are shown in Figures 5-8a-c, for the two years. Total NO_y (Figure 5-8a) was much higher in 2013, consistent with the buildup of NO_x and NO_x product species under stable cool pool conditions. Interestingly, the NO_x levels observed in both years (Figure 5-8b) had quite similar distributions, with only slightly higher values, and an absence of very low mixing ratios in 2013 compared with 2012. As a result the ratio NO_x/NO_y was much higher in 2013, reflecting the much larger degree of photochemical processing that accompanies O_3 production. Diurnal plots of NO_x, NO_y and NO_x/NO_y (Figures 5-9&5-10) make this point quite clearly; the 2012 data show very little variation in NO_x/NO_y throughout the day; in 2013, there is a consistent decrease in NO_x/NO_y throughout the photochemical day as NO_x is converted to products in the same chemistry that made O_3. This processing results in high concentrations of product species: HNO_3, PAN, $RONO_2$, aerosol and snow nitrate, and a faster formation rate of the nighttime species NO_3 and N_2O_5.

The photochemical products of NO_x are operationally defined as NO_y-NO_x and collectively termed NO_z. The average diurnal composition of NO_z in each year is shown in Figures 5-11&5-12 for 2012 and 2013 respectively. In general the major NOz species in 2012 were PANs and alkyl nitrates in the daytime, and N_2O_5 and $ClNO_2$ at night. The major NO_z species in 2013 were HNO_3 and PANs, with some contribution from HONO in the daytime. Note that alkyl nitrates were not measured in 2013. Details of these NOz species will be covered in subsequent sections of this chapter.

5.3.2 VOCs by GC-FID and PTRMS

The section provides an overview of VOC composition measured at Horse Pool during the 2013 experiment, with some comparisons to the 2012 data set. Figure 5-13 shows VOC composition by molar abundance (volume) (A) and mass (B), and OH reactivity (C). Alkanes and unsaturated hydrocarbons were measured by GC-FID; aromatics and oxygenates were measured by PTR-MS. "OH reactivity" refers to the rate constant for reaction of the species with the OH radical, scaled by the species' molar concentration [*Atkinson and Arey*, 2003; *Atkinson and Aschmann*, 1984]. The chart of OH reactivity is not an exact measurement of how much each compound contributes to ozone production; rather, it provides a conceptual illustration of the major VOCs that contribute to chemical activity. In terms of both mass and molar mixing ratio, methane was the dominant species measured at the Horse Pool site, followed by other lightweight alkanes (ethane, propane, iso- and n-butane, and iso-and n-pentane). Due to the slow reaction rate with OH radical, methane accounts for a much smaller fraction of OH reactivity. OH reactivity was more evenly distributed amongst the longer chain alkanes, with contributions from aromatic HCs, and two of the more abundant oxygenates, methanol and acetaldehyde.

The position of the VOC instrument inlets on a movable platform allowed us to determine chemical gradients between 1 and 7.25 m. An experiment to measure chemical gradients was conducted from 7 February to 11 February by moving the inlet sampling height from 1 to 7.25m every 20 minutes. Figure 5-14 shows the results of this experiment for propane. There is no statistically significant gradient, suggesting that primary emissions are well mixed up to 7.25m, and that there is not a significant surface source or sink of propane. In general, we would not

expect a gradient for species that are not soluble in water and do not have a strong snow source.

Next, we will make a general comparison of VOC measurements at Horse Pool in 2012 and 2013. For a comparison of 2012 Horse Pool data to measurements at Red Wash, Utah, in 2011; Weld County, Colorado, in 2011; and Los Angeles, California, in 2010, refer to the 2012 Uintah Basin Winter Ozone and Air Quality Study Final Report [*Lyman and Shorthill*, 2013]. Mixing ratios of hydrocarbons in 2013 at Horse Pool were significantly higher than corresponding 2012 measurements. Figure 5-15 shows a comparison between 2012 and 2013 of the absolute mixing ratios of compounds with the highest concentrations. Figure 5-16 shows the fractional increase from 2012 to 2013 of all measured VOCs. Alkanes, aromatics, other lightweight unsaturated hydrocarbons, methanol, and formaldehyde increased by a similar amount (by a factor of 1.5 to 3.5), while other oxygenates – acetone, acetaldehyde, and MEK (methyl ethyl ketone, or 2-butanone) – increased by a much larger amount, by a factor of 8 to 12. Acetone, acetaldehyde, and MEK are photochemical products, rather than primary emissions. The much larger enhancement of these oxygenates reflects higher photochemical activity in 2013.

Compound ratios can help identify particular emission sources. Figure 5-17 shows ratios of iso- to n-butane, iso- to n-pentane, and benzene and i-butane to propane, for 2012 and 2013. Ratios did not change significantly from 2012 to 2013. Ratios of other alkanes to propane show similar agreement between 2012 and 2013. This indicates that neither the emission source for these compounds nor the chemical composition of emissions changed significantly between the 2012 and 2013 measurement periods. A time series of total OH reactivity is given in Figure 5-18. The lowest points of VOC OH reactivity (28 Jan. and 09 Feb.) correspond to “clean-out” periods and are roughly comparable to average total OH reactivity for the 2012 measurement period, about 10 s^{-1}. The highest VOC OH reactivity periods experienced in 2013 were roughly an order of magnitude higher, around 100 s^{-1}.

5.3.3 Formaldehyde

Formaldehyde is a VOC of particular interest to the Uinta Basin because it can have a variety of sources, and is potentially an important radical source. Comparisons of formaldehyde to the 2012 measurement period, and an investigation of its sources, are discussed below. In 2012, formaldehyde was found to be strongly correlated with methanol, especially in plumes of primary emissions. Figure 5-19 shows the relationship between formaldehyde and methanol for both 2012 and 2013. Compared to 2012, formaldehyde in 2013 was significantly enriched relative to methanol. This additional formaldehyde was likely photochemically produced.

Several VOC instruments deployed in 2012 and 2013, including the NOAA PTR-MS and the University of Wyoming PTR-ToF and Picarro cavity-ring-down spectrometer, were able to capture short-term peaks in a variety of compounds. These short-term peaks, which lasted over a time scale of a few seconds to 20-30 minutes, were a result of the instruments intercepting plumes of high-concentration primary emissions. Analysis of these plumes is a useful tool for distinguishing different categories of primary emissions. A 60-minute running median was subtracted from the full data set for formaldehyde, methanol, benzene, toluene, and methane,

to isolate plumes of primary emissions for closer analysis. The remaining data contains only peaks of fewer than 60 minutes duration, which excludes variation due to photochemical aging, temperature, etc. Correlations between peaks of various compounds measured by the University of Wyoming PTR-ToF mass spectrometer (formaldehyde, methanol, benzene, and toluene) and Picarro spectrometer (methane) are shown in Figure 5-20. Toluene, benzene, and methane are correlated, and methanol and formaldehyde are correlated, indicating that these compounds are emitted by two distinct processes or sets of processes. A plausible emission source of formaldehyde is industrial methanol, which is stored on wellpads and used by some operators as an antifreeze; however, we do not currently have data to definitively link primary methanol measured at Horse Pool to a specific emission source. Source attribution of formaldehyde was done using a simple linear combination model in which the primary emissions are assumed to be represented by methanol and the secondary production is assumed to be represented by O_x (= O_3 + NO_2), and there was assumed to be a background of HCHO. The results of this multivariate fit suggest that of the measured HCHO, 63% was secondary, 30% primary, and 7% was background.

5.3.4 Comparison of PTR-TOF-MS data and PTR-MS results

A comparison of the PTR-TOF-MS [*Graus et al.*, 2010; *Müller et al.*, 2013] data and PTR-MS data is shown in Figure 5-21 as a time series for various VOCs observed in the Basin (acetone, acetaldehyde, methyl ethyl ketone, and methanol). The corresponding linear regression plots for the comparisons in Figure 5-21 are shown in Figure 5-22. The agreement between the PTR-TOF-MS and PTR-MS was well within the uncertainty of the instruments with a high degree of correlation. In this particular case, the significantly reduced duty cycle of the PTR-TOF-MS technique yields improved detection limits in comparison to the PTR-MS measurements, and can be observed in the lower signal to noise ratio of the PTR-MS measurements. In addition to the species shown in Figure 5-21, Benzene was measured using PTR-TOF-MS, PTR-MS, and GC-FID, which was also present at the UBOS 2013 Horse Pool site operated by NOAA CSD. A comparison of the three benzene measurements is shown in Figure 5-23. It can be seen that compared to the PTR-TOF-MS, the GC-FID measurement is consistently 17% lower, although this difference is still within the reported uncertainties of the two techniques.

5.3.5 Carbonyls measured by DNPH Cartridges

During the USU carbonyl sampling exercise, a total of 21 and 14 samples were collected from the Roosevelt and Vernal locations, respectively. As shown in the box-whisker plots of Figure 5-24, 14 different carbonyl species, formaldehyde through 2,5-dimethylbenzaldehyde, were identified at the Roosevelt location and eight species, at typically lower concentrations were identified at the Vernal location. As can be seen, the only species at both locations consistently above 1 ppb(v) were the lowest molecular weight compounds: formaldehyde, acetaldehyde, and acetone.

Figure 5-25 shows the mean values of these species, along with comparisons of NOAA-CSD collected data from the Horse Pool location for the same corresponding time periods. The Roosevelt location showed the statistically highest, at the 95% confidence level, average concentrations of formaldehyde (8.33±0.76 ppb) and acetaldehyde (6.60±0.62 ppb) compared

to Horse Pool (5.12±0.63 ppb and 3.72±0.71, respectively) and Vernal (1.62±0.73 ppb and 1.34±0.32, respectively). While the average acetone concentration at Horse Pool was dominant (6.64±1.34 ppb), it was not statistically different from that observed at the Roosevelt location (4.96±0.69 ppb). As with the other carbonyls, the concentration of acetone observed at Vernal (1.47±0.42 ppb) was significantly lower than that observed at the other two given locations. For further comparison, carbonyl samples collected in 2012, at the Horse Pool location using the DNPH protocol described herein found much lower average formaldehyde, acetaldehyde, and acetone concentrations of 1.73±0.45 ppb, 0.63±0.28 ppb, and 0.68±0.37 ppb, respectively. The 2012 study was during a period of almost no snow cover, few, if any, identifiable inversion periods, and no elevated (exceedances) O_3 episodes [*UBWOS*, 2013] .

Formaldehyde, in particular, is well known to be both directly emitted (e.g. motor vehicles, building materials) and photochemically formed via the oxidation of various hydrocarbons, including methanol. Methanol is known to be used as a pipeline additive during freezing conditions and was observed in ambient air at high abundance during both the 2012 and 2013 field campaigns by the NOAA investigators (see above). Typical urban, rural/suburban, and remote concentrations of formaldehyde are estimated to be 1-60 ppb, 0.1-10 ppb, and 0.3-2.0 ppb, respectively [*Finlayson-Pitts and Pitts*, 2000]. This seemingly would indicate the 2013 wintertime low molecular weight carbonyl concentrations, at least at Roosevelt and Horse Pool, are similar to those in more heavily populated areas (urban or suburban/rural) as opposed to remote areas, as might be, at least demographically, suggested for the Uinta Basin.

Some additional insight may be gained into potential HCHO and related emissions or formation mechanisms by examining the typical diurnal behavior observed at the various locations during the sample period (see Figure 5-26). As can be seen, all of the carbonyl compounds displayed an apparent diurnal pattern, generally peaking during the early afternoon sample period. This would be indicative of at least some photochemical formation for some of the carbonyl species. It is also of interest to note that, the concentrations observed at the Vernal location almost always showed the lowest concentrations and the least amount of diurnal variations. Further, it can be seen that the NOAA data from Horse Pool generally showed the greatest degree of "clean out" following the small snow storm on the evening of Feb. 18, 2013, as well as the most rapid rate of build up after the storm passed. This would be supportive of the Horse Pool site being more directly located in the active source emission and photochemical center of the Basin, as opposed to areas more affected by transported air masses (Roosevelt) or more strongly impacted by localized emissions (Vernal).

5.3.6 PANs and Nitryl Chloride

Results of the iodide ion CIMS measurements of PANs were quite different in 2013 compared to 2012 while nitryl chloride results were broadly similar to those during UBOS 2012. These results are reflective of several aspects of the chemistry that produces these species. PANs are produced by the same NOx-VOC chemistry that produces O_3 and so were much more abundant in 2013. Nitryl chloride results from a combination of nighttime NOx chemistry and soluble chloride, the availability of which was the same or less in 2013 relative to 2012. The details of PANs and $ClNO_2$ observations are described below.

A summary of the PAN levels observed during UBOS 2013 is shown in Figure 5-27 in comparison with levels observed last year, and in several urban photochemical studies including the Pasadena, CA site during CalNex 2010; the LaPorte, TX ground-level site during the TexAQS 2000 study; and at the ground-level site during the Nashville, TN 1999 Study. The UBOS 2013 results were easily the highest of the data sets shown. There are likely three reasons for this: 1) active VOC-NOx photochemistry, 2) thermal stability of PAN at low temperatures, and 3) reduced deposition on snow surfaces relative to typical summertime surfaces.

There are number of PAN-type compounds that are typically observed in the atmosphere [*J.M. Roberts*, 2007], and their relative abundances are reflective of the VOCs that contribute to the VOC-NOx photochemistry in a given air basin [*Williams et al.*, 1997]. Acetyl peroxynitrate ($CH_3C(O)OONO_2$) is the most abundant PAN compound in the polluted troposphere under most circumstances. Propionyl peroxynitrate (PPN) is usually the second most abundant PAN-like compound, with relative abundances in the range of 10 to 15%. The correlation of PPN with PAN during UBOS 2013, shown in Figure 5-28, was very tight ($R^2 = 0.99$) with a high ratio (22%) compared to typical urban areas. This feature of the PANs chemistry is due to the unusual abundance of alkanes in this UBOS environment relative to other PAN-producing species such as alkenes [*Altshuller*, 1993].

The intimate relationship between PAN and O_3 formation is one of the well-known features of photochemical ozone pollution [*J Roberts et al.*, 1995]. The correlation of O_3 and PAN observed during UBOS 2013 is shown in Figure 5-29 along with correlations from UBOS 2012, the Pasadena site during CalNex 2010, and the LaPorte ground site during TexAQS 2000. Several aspects of these relationships bear commenting on. As noted in the UBOS 2012 report the O_3 PAN relationship was dominated by NOx titration and depositional losses; the TexAQS 2000 data show much higher O_3/PAN ratios because of the presence of highly reactive VOCs that don't make PAN but do make O3 (e.g. ethylene, 1,3-butadiene) and faster thermal losses of PAN; UBOS 2013 data points have the highest PAN values due to the efficiency of alkanes in making PAN and slower thermal loss of PAN; data from CalNex 2010 are in between UBOS 2013 and TexAQS because the Pasadena urban VOC mixture is not as enriched in highly reactive VOCs as in the Houston Ship Channel and CalNex conditions were intermediate in temperature. All of the data sets that have the higher concentrations showed curvature, which was evidence of less efficient O_3 production at highest NOx conditions.

Nitryl Chloride values measured during the UBOS 2013 campaign are summarized in Figure 5-30 along with data from 3 other studies. The values from UBOS 2013 were only slightly lower than those observed in UBOS 2012. These lower values imply that either chloride was less available for reaction or N_2O_5 hydrolysis to HNO_3 was faster in 2013 due to more aqueous surface area on aerosols and the ground. Another factor could be that the loss of $ClNO_2$ to the snow surface was faster than the loss of $ClNO_2$ to the bare ground that was present in 2012 [*McLaren et al.*, 2012].

Field observations of nitryl chloride are relatively new, however laboratory studies of $ClNO_2$ have been fairly extensive, some going back several decades. The uptake rate of $ClNO_2$ scales as

$Hk^{1/2}$, where H is the Henry's coefficient and k the first order reaction rate. The aqueous solubility of $ClNO_2$ is quite low (H = 0.05 M/atm), however there is potential for significant reactions on snow surfaces, especially highly contaminated surfaces as the snow surfaces in the Uinta Basin appear to be. Vertical gradients in $ClNO_2$ provide one piece of evidence for deposition of $ClNO_2$ to snow surfaces, and are shown in Figure 5-31 for the period. Unfortunately, the N_2O_5 inlet was not co-located with the $ClNO_2$ inlet, as the N_2O_5 instrument required a shorter inlet that required frequent maintenance. It is possible that significant gradients in N_2O_5 led to large gradients in $ClNO_2$ formation rates, making it impossible to derive any quantitative statements about $ClNO_2$ uptake on snow. It should be noted that there were no significant gradients in $ClNO_2$ after sunrise, so potential uptake in snow does not affect the calculation of the radical source from $ClNO_2$.

5.3.7 Acids by NI-PT-CIMS

During the UBOS 2013, an acid-CIMS was deployed at Horse Pool site to measure various acids, including hydrochloric acid (HCl), nitric acid (HNO3), nitrous acid (HONO), formic acid and pyruvic+butyric acid. Several other organic acids were also observed by the acid-CIMS, but their concentrations are not reported here due to either low values or no calibration available during the campaign. The important findings from the measurement of various acids are shown individually in the following sections.

5.3.7.1 HCl:

The average concentration of HCl during UBOS 2013 was 0.13±0.19 ppb. Comparison of the 2013 value with 2012 is not available, since concentration of HCl in 2012 was not reported as a result of high background issue. The measured HCl concentration in UBOS 2013 is significantly lower than the concentration at Pasadena site (urban site) during CalNex 2010 (0.82±1.0 ppb). HCl measurements at Horse Pool in 2013 show low concentrations at night and a peak at noontime (Figure 5-32). The peak of HCl at noontime is probably due to the displacement reaction of HNO_3, which also shows a noon peak (also seen in Figure 5-32), with Cl^- in aerosol and snow pack to form HCl. However, the enhancement ratio of HCl to HNO_3 varied from day to day, suggesting the displacement of HCl from Cl^- may also depend on availability of Cl^- and aerosol or snow pack acidity.

5.3.7.2 HNO_3:

HNO_3 can be formed from reaction of NO_2 with OH at daytime, reaction of N_2O_5 with aqueous surfaces (e.g. particles) and reaction of NO_3 with VOCs at night time. In any case, HNO_3 is regarded as a sink of NOx. HNO_3 is also an indicator of chain-terminating reaction during the daytime. The average concentration of HNO_3 in 2013 at Horse Pool was 4.5±3.2 ppb, which is 8 times larger than the value (0.54±0.41ppb) in 2012 (Figure 5-33). The diurnal variations of HNO_3 in 2013 show highest concentration around noon and lowest concentration in the evening (Figure 5-32). It is interesting that HNO_3 concentration increased steadily from 12 am to 6 am. Considering that HNO_3 deposits to the ground and aerosol surfaces continuously, the increase of HNO_3 before dawn suggests that HNO_3 production from reaction of N_2O_5 with particles occurred at a rate sufficient to overcome the loss by deposition (which is significant).

5.3.7.3 HONO:

HONO is a key species in the atmosphere because its photolysis is an important source of OH radical. However, the HONO sources are not well understood, as reflected by the unexplained daytime HONO concentrations observed in many studies (see *VandenBoer et al.,* [2013] and references therein). The possible sources include heterogeneous reaction of NO_2 with H_2O on particles or surfaces, photolysis of nitrate on particle surfaces or snow pack, and reduction of NO_2 via an organic chromophore under sunlight [*Li et al.*, 2008; *Su et al.*, 2011; *Zhou et al.*, 2011 and references therein]. The average of HONO mixing ratio in 2013 at Horse Pool was 0.55±0.58 ppb, significantly larger than the mixing ratio in 2012 (0.05±0.04 ppb) (Figure 5-33). The diurnal variation of HONO in 2013 showed higher concentrations during the daytime and lower at night, in contrast to 2012 during which the highest concentrations were at night and early morning, as shown in Figure 5-34. The HONO concentration in 2013 is far above what can be explained by reaction of NO with OH radical. Both the diurnal profile of HONO concentration and production rate from the unknown source follow very well with the intensities of solar radiation, suggesting that the unknown HONO source is related to sunlight. This high daytime HONO source presents a bit of a conundrum in that photochemical modeling of wintertime O_3 both in the UGRB [*Carte and Seinfeld*, 2012], and for UBOS 2013 [*Edwards et al*., 2014, manuscript in preparation] do not require such a HONO source to reproduce the observed O_3 and in fact substantially over-predict O_3 when the high daytime HONO levels are included.

The moveable inlet attached to the sampling tower allowed for measurement of HONO gradients between 1 and 7.25m. Minor gradients in the range 0-15% were observed for the 2.5 day period when the highest HONO values were present, as shown in Figure 5-35. The average differences between HONO measured when the inlet was down compared to up is also shown in Figure 5-35 and shows that HONO is deposited to the snow at night and emitted from the snow during the during the day. Classic turbulent diffusion theory relates the timescale of transport of a species (t) to a height above the ground (σ), with an eddy diffusivity K_z;

$$t = \sigma^2/2K_z \qquad \text{(Eq 1)}$$

The expected gradient at a height difference of 6.25m can then be calculated as a function of K_z for a chemical species that has a first order loss rate in the atmosphere, which in the case of HONO is simply its photolysis rate, J_{HONO};

$$\%\text{Gradient} = \{1-\exp(-J_{HONO}*\sigma^2/2K_z)\}*100 \qquad \text{(Eq 2)}$$

The result of this calculation for an average daytime maximum J_{HONO} of $0.0016s^{-1}$ is shown in Figure 5-36. The plot shows that the range of observed gradients (0-15%) corresponds to a range of K_z of 1000 to 10000 cm^2/sec, which is reasonable for a stable winter daytime boundary layer [*Liu et al.*, 1984]. The range of K_zs can then be used to calculate the concentration profiles with height that would be expected at the photolysis rate corresponding to mid-day (0.0016 sec^{-1}), as shown in Figure 5-37.

There are several interesting features that are illustrated by Figure 5-37. HONO concentrations fall off fairly rapidly with height for the entire range of K_zs used in the analysis. While a tower height of 7.25 m results in observable gradients, tower heights on the order of 15 to 20 m would be ideal. Conversely, it would be very difficult to obtain interpretable HONO gradient measurements at 1.8 m, as was the case in the Wyoming study simply because the differences expected will be within the variability of the ambient signals. The statements on daytime HONO sources in Rappenglück et al. (2013) are based on comparison of all data at 1.8m with all data at 10cm, not comparisons of high and low inlet measurements made consecutively, and are unconvincing for that reason. The above turbulent diffusion analysis indicates that further refinement in the conclusions about the presence or absence of daytime HONO gradients in the Wyoming study are unlikely to be forthcoming. The gradients in Figure 5-37 show that rather than being present in the entire 150m deep PBL, HONO fills only 9 to 21% of the 'box' depending on the value of K_z. This feature of the HONO source, when incorporated into the photochemical models, could at least partially resolve the HONO conundrum described above.

The fluxes of HONO emitted from the snow surface can be estimated from the estimated range of K_zs and the measured gradients. In the simplest formulation, where K_z is assumed to be constant with altitude, then the flux is simply;

$$F = -n_a K_z(dC/dz) = -n_a K_z(\Delta C/\Delta z) \qquad \text{(Eq 3)}$$

where n_a is a conversion factor, and dC/dz is the HONO gradient. The maximum flux estimated during the gradient measurements was 67 µgN/m^2-hr, (18.6 ngN/m^2-sec), corresponding to a ΔC of 200 pptv, over 6.25m, and K_z = 10,000 cm^2/sec. This value is about 2.5 times higher than laboratory measurements of snow photolysis from the Sierra Nevada mountains [*Beine et al.*, 2008], and several hundred times higher than daytime fluxes measured at Summit Greenland [*Honrath et al.*, 2002]. The UBOS 2013 snow value is about 10 times higher than the highest HONO fluxes reported for boreal forest soils [*Maljanen et al.*, 2013], however soils that have been fertilized or otherwise had substantial nitrogen deposition can be almost 100 times higher than the UBOS 2013 value according to Su et al., (2011).

A volume-concentration based analysis of HONO sources and sinks represents another means of comparison of the UBOS 2013 results with expected chemistry and with data reported by other studies, including Rappenglück (2013). The daytime formation of HONO from HO and NO, and the photolysis of HONO back to HO and NO and reaction of HONO itself with OH are often referred to the HONO "steady state":

$$OH + NO + M \Rightarrow HONO + M \qquad (k_4)$$

$$HONO + h\nu \Rightarrow HO + NO \qquad (J_{HONO})$$

$$HONO + OH \Rightarrow NO + H_2O \qquad (k_5)$$

and the HONO concentration that can be calculated by assuming these reactions are in steady state (i.e., d[HONO]/dt = 0) is referred to as [HONO]ss;

$$[HONO]ss = k_4[OH][NO]/(J_{HONO} + k_5[OH]) \quad \text{(Eq 6)}$$

where [OH] is either measured or modeled, and the other quantities are measured. [HONO]ss is usually quite low for a given air basin. For example during the UBOS 2012 study [HONO]ss was approximately 40% of the measured mid-day HONO, which was 25 pptv [*Edwards et al.*, 2013]. HONO above steady state values is assumed to be supplied by an unknown source, and because the main daytime loss is photolysis, the magnitude of this source can be estimated;

$$HONO_{source} = J_{HONO}\{[HONO]meas - [HONO]ss\} \quad \text{(Eq 7)}$$

The average [HONO]ss during UBOS 2013 was 0.06 ppbv based on a modeled [OH] of $1x10^6$ molec/cm^3 from recent chemical modeling work [*P. Edwards*, unpublished results]. The HONO volume source implied by our measured mid-day averaged conditions is 3.6ppbv/hr. This is quite a bit higher than most daytime HONO source estimates, but is on the same order as the results of Rappenglück et al, (2013) who estimated 2.25 ppbv/hr based on data from the 2011 Wyoming Study.

There is a need to understand the origin of the HONO source from snow, in order to understand whether NOx controls would be effective in reducing it. Nitrite concentrations in the snow were quite high during the campaign (0.1-0.5 µM), and increased gradually during the period from 28 Jan.-8 Feb., when ozone and other secondary species also accumulated. Nitrite in snow correlated moderately with nitrate in snow (R=0.70) see Figure 5-38, suggesting nitrite in snow might come from the photolysis of nitrate in snow. Nitrite in the snow can undergo the following reversible acid-bases reaction and HONO in the aqueous phase can partition into the atmosphere:

$$NO_2^-{}_{(aq)} + H_3O^+ \; <=> \; HNO_{2(aq)} + H_2O \quad \text{Eq(8)}$$

$$HNO_{2(aq)} <=> HNO_{2(g)} \quad \text{Eq(9)}$$

$$HONO^* = [NO_2^-]/H(1+K_a/[H^+]) \quad \text{Eq(10)}$$

The equilibrium gas phase HONO concentration ($HONO^*$) depends on snow nitrite concentrations, pH values in snow (Figure 5-39), and the Henry's Law constant, *H*. The circles in the graph show the measurement results of snow near Horse Pool site. This analysis assumes the presence of a liquid layer on the snow, which is reasonable for snow above about -25°C, and uses the balance of measured cations and anions to estimate $[H^+]$. There were two snow events during the 2013 campaign: 28 Jan. and 9 Feb. It can be seen that pH value decreased and nitrite concentration in snow increased, as the snow aged after snow precipitation. The calculated HONO* ranged from below 0.01 ppb to about 0.5 ppb, somewhat lower than measured HONO ambient concentrations. However this is based on ions measured in the top 1 cm of snow, it is quite plausible that the liquid layer on the surface of the snow is more concentrated hence of lower pH. While the ultimate mechanism remains somewhat uncertain, the HONO source from snow likely scales with nitrate deposition to the snow and would be sensitive to reduction in NOx. Whether this relationship has a linear or threshold dependence on NO_3^- deposition is unknown at this time.

5.3.7.4 Formic acid:

Direct emission of formic acid is thought to be low [*Paulot et al.*, 2011], but formic acid is also formed secondarily by oxidation of other volatile organic compounds (VOCs). Formic acid can partition into particle phase and contribute secondary organic aerosol (SOA) formation. Several studies showed that modeled formic acid using a state-of-art chemical mechanism is substantially lower than the measured concentrations in various environments [*Paulot et al.*, 2011; *Sommariva et al.*, 2011; *Stavrakou et al.*, 2012], indicating that improvements in chemical mechanisms are needed. The measured formic acid concentration in 2013 at Horse Pool was 2.34±1.27 ppb, significantly higher than the measured concentration in 2012 (0.58±0.28 ppb) (Figure 5-33). Diurnal variation of formic acid show both morning and afternoon peaks (Figure 5-40). The morning peak may be related to the several fog events during the campaign, whereas the afternoon peak is likely due to secondary formation.

5.3.7.5 Pyruvic+butyric acid:

Pyruvic acid and butyric acid were measured at the same masses in acid-CIMS. The sensitivity of butyric acid is much lower than pyruvic acid in acid-CIMS, thus the concentrations reported here are expected to be mainly from pyruvic acid. The average concentration of pyruvic+butyric acid in 2013 campaign was 47±34 ppt, also much higher than the values in 2012 (7±3 ppt) (Figure 5-33). The diurnal variations of pyruvic+butyric acid show substantially higher concentration in the afternoon (Figure 5-40), suggesting secondary formation is the important source for these two acids. The correlation between formic acid and pyruvic+butyric acid is moderately strong (R=0.68), indicating they share common sources.

5.3.8 Radical Source Calculations

The ultimate goal of the UBOS 2013 effort at Horse Pool was to determine the processes that lead to O_3 formation, especially the photochemical radical sources that are initiating VOC reactions. The main sources observed in this study, are summarized by the following equations, where $h\nu$ denotes a photon, λ is the wavelength and ϕ is the quantum efficiency (IUPAC data)[*Ammann et al.*, 2013];

OH Radicals

from O_3

$O_3 + h\nu \Rightarrow O(^1D)$ (λ <305nm, ϕ = 0.90)

$O(^1D) + H_2O \Rightarrow 2OH$

$O(^1D) + M \Rightarrow O(^3P)$

$O(^3P) + O_2 \Rightarrow O_3$

from HONO

$HONO + h\nu \Rightarrow OH + NO$ (λ <395, ϕ = 1.0)

from HCHO

$HCHO + h\nu \Rightarrow H + HCO$ ($\lambda < 375$, $\phi = 0.04 - 0.78$)

$H + O_2 \Rightarrow HO_2$

$HCO + O_2 \Rightarrow HO_2 + CO$

(note: $HO_2 + NO \Rightarrow HO + NO_2$ completes OH formation)

Cl Atoms

from $ClNO_2$

$ClNO_2 + h\nu \Rightarrow Cl + NO_2$

The measurements of the chemical precursors that form radicals are described above. Spectral irradiance, the other ingredient that is required to calculate production rates, were estimated from the average irradiances from 2012 and the measured increase in albedo from 2012 (35%) to 2013 (90%) associated with the presence of snow in 2013. The average $O_3 \Rightarrow O(^1D)$ photolysis rate (J_{O3}) for 2013 is compared to those measured in 2012 and at the Pasadena site during summer 2010 in Figure 5-41. Average photolysis rates, J_{HONO}, J_{HCHO} and J_{ClNO2} were calculated for 2013 in the same manner, in order to estimate the average radical production rate for each of the above processes.

The average production rate for each process is shown in Figure 5-41 along with the estimates from UBOS 2012 and CalNex 2010. The CalNex 2010 plot was taken from Young et al. (2012), who noted that while ozone photolysis was the largest radical source, HONO and HCHO were also apparent, indeed they roughly totaled the source from ozone. In contrast, the UBOS 2013 radical sources were much larger than either of the other studies, and were dominated by HONO and HCHO. It should be noted that the HONO radical source in 2013 is for the values measured at 7.25m above the ground, and for the reasons shown in the previous section on HONO measurements, this is an overestimate in that this source likely decreases rapidly with height, and does not exist throughout the entire boundary layer. This aspect, coupled with the uncertainties in HONO measurements, amplifies the need to better quantify HONO and its vertical distribution.

There are significant differences in the reactivities of some VOCs towards Cl atoms relative to OH radicals. For example, small alkanes are up to 200 times more reactive towards Cl atoms, and methanol is a factor of 60 more reactive towards Cl atoms. This changes the simple picture shown in Figure 5-41, making $ClNO_2$ more important, particularly in this environment in which small alkanes and methanol are especially abundant. For this reason, photochemical models need to include the appropriate Cl atom chemistry.

5.3.9 Lidar Measurements

5.3.9.1 Meteorological Processes in the Atmospheric Boundary Layer Using Doppler Lidar

Concentrations of pollutants (including ozone O_3, methane CH_4, ethane C_2H_6, etc.) are determined by emission rates and chemical transformations over a time period, by the 3-D volume occupied by those pollutants, by how well they are mixed within the volume, and by the time constants for mixing out of that volume. The volume is determined by the vertical depth and horizontal extent of distribution of the pollutants. In general, stable, light-wind, cold-surface wintertime conditions are characterized by inhibited mixing, and consequently trapping of surface-emitted species in shallow, ground-based layers, inhomogeneous or "lumpy" concentrations in the horizontal, and layered structure in the vertical.

Instrumentation was deployed to the Uinta Basin during January and February 2013 to study meteorological processes controlling the extent and transport of pollutant species in the horizontal and vertical, and their vertical distribution. Tethered balloons and ozonesondes (to measure profiles of O_3 and of atmospheric thermodynamic variables), instrumented light aircraft and mobile vans, and an O_3-profiling differential-absorption lidar (DIAL) system are described elsewhere in this report. A Doppler lidar system, NOAA's High Resolution Doppler Lidar (HRDL), described by Grund et al. (2001), was deployed to the Horse Pool site to measure flow properties at high resolution and precision in the lowest 2 km of the atmosphere; this site was in the eastern sector of the Basin. Such high resolution and precision was needed to sample the weak and often shallow flow layers affecting the horizontal and vertical distribution of atmospheric contaminants.

Within the Uinta Basin, mobile van and light aircraft measurements found source activity to be highly variable in the horizontal, as described elsewhere in this report. For example, gas-drilling operations predominantly in the eastern sector of the Basin resulted in higher concentrations of CH_4 and other substances, predominant oil extraction in the western sector produced a different mix of airborne chemicals, and significant NO_X emissions were localized in the south-central portion of the Basin near the Chapita site and other places (Figure 4-21). Such spatial source variability means that horizontal transport may play a role in the generation of secondary pollutants by mingling emissions from different source regions. So an important question is whether the weak flows in the Basin could perform this kind of transport in the strongly stable, light-wind wintertime conditions encountered during the high-O_3 episodes.

Flow in complex terrain is generally closely related to the topography. Figure 5-42 is a topographic map of the Basin with contours chosen to emphasize basin characteristics—the 1564-m contour between purple and blue represents the elevation of the Horse Pool site, and all elevations above 2164 m appear black, thus clearly outlining the Basin. It is of interest that, although the main drainage of the Uinta Basin is the northeast-southwest-flowing Green River, the Basin orientation is elongated west-east, the Green River marking the mid-basin low point.

Time-height cross sections of HRDL-measured wind profiles for a 24-hr diurnal period are shown in Figure 5-43 for 15 Feb 2013, a day on which 8-hour average ozone concentrations at Horse Pool reached 123 ppb. During nighttime hours the near-surface winds blew from an

easterly direction, but during the day they reversed to westerly. Wind speeds were very weak at 1-2 m s^{-1}. The diurnal cycle was clear on this day; on other days this tendency was also observed, although passing synoptic scale disturbances often interrupted the pattern, because the diurnal flows were so weak.

Diurnal cycles of winds in complex terrain are generally driven by the daily heating and cooling cycle at the surface. Over snow-covered surfaces at night, strong cooling occurs which drives shallow downslope drainage flows. On the scale of the Basin, this drainage flow would be from easterly directions at Horse Pool. Daytime westerly flows could be a result of daytime surface heating but this is less certain given the cold temperatures, strong stability, and snow surface. Westerly flow in this part of the Basin would be consistent with a thermally forced, up-basin wind due to surface heating. Instrumented tower data at Horse Pool provides evidence for surface heating in the form of temperature traces at 2, 9, and 18 m above ground, which show the lower-level temperatures much colder at night than higher up, but which crossed over during the morning hours to become 1-2 degrees warmer at the lower levels (Figure 5-44). Positive near-surface heat fluxes, indicative of surface heating, were also evident during the day.

When the surface is warm relative to the adjacent atmosphere, an unstable boundary layer or 'mixed layer,' sometimes referred to as a convective boundary layer (CBL), can form. A signature of a CBL is that the potential temperature profile $\theta(z)$ is approximately constant or slightly decreasing with height, and the profiles of other constituents, such as water vapor, O_3, CH_4, etc., may also become constant or nearly constant with height. Figure 5-45 shows θ and O_3 profiles from a tethered-balloon system at Horse Pool for 1409 MST (2109 UTC) on 14 Feb. The nearly constant profiles and warm surface indicate a mixed-layer structure. For boundary layers in general, a mixed-layer structure can be produced by wind shear in addition to surface heating, but here the wind speeds, and therefore the shear, are too weak to contribute significantly to the mixing through the CBL. Existence of CBL structure under these conditions is thus another indicator of surface-based heating of the atmosphere.

As discussed in Section 3, high-O_3 events coincided with the development of a strong pool of cold air in the Basin. During winter, cold air accumulates in the bottom of the Basin at night but is not mixed out during the day due to relatively weak surface heating consistent with low sun angles, highly reflective snow cover, and short days. The resulting pool of cold air builds in depth and strength, persisting through many days until the process is interrupted by a change in the synoptic pattern (e.g., [*Whiteman et al.*, 1999]) . The cold-air inversion layer, comprising this cold pool, suppresses mixing, so at night, the cold surface generates drainage flows that carry surface-released pollutants to lower regions of the Basin with little vertical mixing. During the day, the warm-surface-based CBL mixes near-surface pollutants upward through the shallow mixed layer, and the daytime flow carries the polluted layer up slope. At Horse Pool, the nocturnal flows were seen to be from an easterly direction, and the daytime up-basin flows, from a westerly direction. Also at the Horse Pool site, Figure 5-45 shows that the CBL only grew to a depth of ~70 m during the day.

Tethered-balloon soundings were taken simultaneously at two other sites in the Uinta Basin, at Ouray low in the Green River Valley (elevation 1430 m) and at Fantasy Canyon (elevation 1470 m) to the south-southeast of Horse Pool at an elevation intermediate between the other two sites (Figure 8-6). Figure 5-46 shows afternoon profiles of θ and O_3 at all three sites. A mixed-layer structure was evident at all sites, but the CBL was deepest at the lowest site (Ouray), and shallowest at the highest of the three sites (Horse Pool). Significantly, when plotted against height above sea level (ASL) as the vertical coordinate, the height of the CBL was very similar at about 1650 m ASL at all sites. The top of the inversion layer, marking the top of the cold pool, was also similar at ~1900 m, a value seen on other mid to late episode days. In other words, the cold pool was essentially a lake of cold air filling the Basin and having a relatively flat, level top, as is often evident when fog or stratus clouds occupy the cold pool. In addition, the afternoon mixed layer also tended to have a level top, even though the Basin topography rises and falls beneath it.

Interesting questions are, how do the cold-pool and mixed-layer structure evolve as an episode builds, and is the inversion at the top of the cold pool impenetrable or leaky? Figure 5-47a shows the afternoon vertical structure at the three sites at the beginning of an episode on 1 February, and Figure 5-47b shows mid-episode afternoon profiles four days later on 5 February. The θ profiles on 1 Feb show that the surface-based inversion at the top of the cold pool reached just over 1750 m ASL. As the episode proceeded, the cold pool depth grew to nearly 1950 m by 5 Feb. The afternoon CBL or mixed-layer height, however, remained the same at just under 1650 m ASL as seen in both the θ and O_3 profiles. Inversion strengths above the mixed layer of 4°/100 m (1800-1900 m on 5 Feb) to 6°/100 m (1650-1750 m on 1 Feb) represent very strong inversions, which should strongly inhibit vertical displacement and mixing into the inversion layer.

The depth of the shallow mixed layer changed little through the episode, but the layer cooled by 2°C and the O_3 produced from concentrated pollutants, which were emitted into and then trapped within this layer, increased by ~40 ppb over the 5-day period (Figure 5-47-left panels). Above the cold-pool inversion on 1 Feb, O_3 concentrations were ~50 ppb, which coincided with background values measured during the previous basin clean-out period (29 January) and at rural sites in Utah, such as Canyonlands NP. These low concentrations are seen above 1750 m MSL, corresponding to the cold-pool top. Just below the top of the cold pool, O_3 concentrations were significantly above background, indicating that “leakage” of pollutants upward into the strong inversion layer has occurred, most likely as a result of complex flow interactions within the Basin cold pool, as opposed to direct diffusion up through the inversion. This upward displacement of pollutants continued through the episode, as O_3 concentrations on 5 Feb exceeded 90 ppb below 1850 m and were well above background up to the top of the cold pool at 1900 m MSL. Such upward escape of pollutants into the inversion layer would have to be accounted for in performing basin-wide pollutant budgets.

Concentrations of many pollutants besides O_3 were found to be very high, even when compared with highly polluted urban areas, most notably ethane (Section 6.0). The vertical trapping of pollutants within the Basin by the cold-air inversion layer is a major factor, but the

light-and-variable nature of the winds also contributed. Light winds allow for large doses of emissions into an atmospheric volume as it passes over a source, and the variable winds allow the volume to pass over many sources, sometimes back and forth over a source region. The displacement of a small volume or "parcel" of air can be traced by calculating and plotting layer-averaged trajectories from the 20-min wind profiles (e.g., Figs. 5-2 and 5-43). For flows exhibiting a diurnal cycle, Allwine and Whiteman (1994) have argued that the net trajectory displacement over a 24-hr period is a measure of a "ventilation" effect of these flows. Measured trajectories have been used in prior studies to determine overnight transport of O_3 plumes [*Banta et al.*, 1998] and the effects of sea-breeze wind reversals on pollutant transport [*Banta et al.*, 2004; *Banta et al.*, 2011]. Here we use 24-hr forward trajectories to investigate transport and ventilation effects in the Basin.

Examples of 24-hr trajectories calculated from 20-min HRDL winds are given in Figure 5-48 for 30-31 Jan and 14 Feb., starting at about sunset (1700 MST or 0000 UTC). It is important to note that these are single-station trajectories, and the locations of the endpoints in time assumes that the winds over the relevant portions of the Basin are uniform, which is unlikely, especially as the trajectory height is closer to the ground and the location moves farther from the Horse Pool measurement site. The trajectories should be viewed as an indicator of the potential for transport and redistribution.

On 30 January (Figure 5-48a) the easterly drift of the low-level trajectories (black, red) early in the evening (closest to the measurement site) reflect the continuation of the daytime westerly-component flow. This flow reversed to the easterly drainage direction after 2100 MST (0400 UTC; see Figure 5-2). Over the next 9 hr the trajectory traveled more than 70 km to the west, until predawn and daytime flow became more variable and light. Another day showing large trajectory displacements was 31 January (Figure 5-48b). On both days O_3 concentrations were less than 80 ppb. In contrast, 14 February was one of the highest pollution days, ozone concentrations exceeding 140 ppb at the Ouray UDEQ monitoring site. Figure 5-48c shows that the 24-hr trajectory displacements below 200 m AGL were ~30 km or less indicating low ventilation factor. The weak, variable winds caused the trajectories to wander about within ~20 km of their origin, accumulating emissions from many sources—and presumably many *types* of source—in this area. The fact that the trajectories maintained direction for a few to several hours—in drainage or upslope flows, for example—means that transport of a few tens of km could occur, even though the winds were light. These distances would be sufficient to expose a traveling volume of air to several types of source within the Basin. In the western part of the Basin, where many sources are above the top of the high-pollution layer coinciding with the daytime mixed-layer (1650 m ±50 m), persistent downslope drainage flows are a potential mechanism for bringing emissions down into the lower levels of the Basin.

Another way to use wind data to trace air movement is backward trajectories, which are constructed by starting at a desired time and height, and using the observed winds to trace air-parcel locations backwards in time. Backward trajectories are useful for inferring potential sources for events occurring at a site. For example, on several occasions, anomalously low ozone concentrations were noted at 300-350 m above the Horse Pool site as described in

Section 8 and also shown in the TOPAZ lidar results below. Figure 5-49 shows backward trajectories for 300 m above Horse Pool passing over the Bonanza Power Plant power plant for one such occurrence. The trajectories passing over the power plant indicates that the O_3 "hole" was likely caused by titration of O_3 by NO emissions from the plant, as described in the section on TOPAZ results below. In particular, 14 Feb was a day exhibiting high ground-level O_3 concentrations at sites within the Basin, but the Bonanza Power Plant effluent plume was *above* the cold-pool inversion and thus completely isolated from the near-surface pollutant layer, at the short time scales involved in the transport of the plume across the Basin. This further illustrates that the Bonanza Power Plant power plant plume did not contribute to the high ground-level O_3 during the highest wintertime O_3 events.

5.3.9.2 TOPAZ Lidar

The primary objective of deploying the TOPAZ lidar at the UBOS studies was to characterize the vertical structure of ozone from near the surface to a few kilometers AGL at high temporal and spatial resolutions. In the lowest few hundred meters, the TOPAZ ozone profiles complemented the collocated ozone tether sonde measurements at Horse Pool by providing temporal continuity between tether sonde launches. The lidar ozone profile measurements above 500 m AGL provided information about the ozone structure beyond the maximum altitude reachable with the tether sondes. This was critical for detecting ozone layers aloft, which may be associated with long-range transport of ozone in the lower free troposphere or downward mixing of stratospheric ozone. Under the right conditions, these ozone layers aloft can be mixed down to the surface and can impact surface ozone concentrations. One hypothesis that had been put forth prior to the UBOS studies was that the high surface ozone concentrations often observed during the winter months in the Uinta Basin were at least partly caused by long-range or stratosphere-to-troposphere transport of ozone. The ozone lidar observations were crucial for confirming or disproving this hypothesis. During the two UBOS studies, numerous comparisons were performed between the lidar measurements and observations from the tethered ozone sondes, the surface in situ ozone sensors, and the free-flying ozone sondes (2012). Generally, the lidar measurements compared well with the other ozone measurements, and the observed discrepancies were within the stated instrument accuracies of the lidar and the in situ sensors.

UBOS 2012

The TOPAZ ozone lidar was operated on 14 days between 3 and 29 February 2012 and recorded 62 hours of ozone and aerosol backscatter profile data. In the absence of any high ozone events, the sampling strategy consisted of operating TOPAZ for several hours at a time and covering different segments of the diurnal cycle on different days. TOPAZ ozone data are posted at http://www.esrl.noaa.gov/csd/groups/csd3/measurements/ubwos/topaz/. Figure 5-50 shows a 5-minute average ozone profile observed in the early afternoon on 7 February 2012. This ozone profile was typical for the vertical ozone structure observed during UBOS 2012, which was characterized by unusually warm and snow-free conditions, and fairly deep, well-mixed boundary layers. Figure 5-50 also illustrates how the lidar ozone observations from three elevation angles were spliced together to create a composite vertical profile extending from 15 m to about 3 km AGL.

Figure 5-51 shows all ozone lidar measurements from the 2012 study displayed as normalized probability distribution functions (PDFs) for three altitude ranges: 15 – 200 m AGL, 200 – 1000 m AGL, and 1000 – 3000 m AGL. The mean ozone values for these altitude ranges were approximately 46 ppbv, 48 ppbv, and 52 ppbv, respectively. Figure 5-51 shows that no ozone values above about 75 ppbv were measured with the lidar at any altitude below 3000 m AGL. In particular, no exceedances of the 8-hour National Ambient Air Quality Standard were observed. This lack of high ozone episodes was likely due to the fact that the boundary layer was generally rather deep and well-mixed, which prevented a buildup of high concentrations of ozone and its precursors. The almost complete absence of any snow cover during the UBOS 2012 study prevented the formation of a shallow cold-air pool and the development of strong temperature inversions. As a result, the boundary layer was much deeper and much better ventilated than during typical wintertime conditions in the Uinta Basin. Figure 5-51 also reveals that on average ozone concentrations were increasing slightly with altitude during UBOS 2012. The mean ozone value of about 52 ppbv in the upper altitude bin is typical for background ozone conditions in the lower free troposphere for the western US. The slightly lower ozone values in the two altitude ranges below 1000 m are probably due to titration and surface deposition of ozone. The slight vertical gradient of ozone and the similarity of the ozone PDFs for the three altitude ranges are consistent with the generally well-mixed conditions observed during UBOS 2012.

A few times during the 2012 study, very low ozone values due to titration were observed with the in situ sensors at the Horse Pool site. TOPAZ showed that these low ozone values extended to several hundred meters AGL throughout the well-mixed BL. A trajectory analysis using HRDL lidar wind observations indicated that in these cases the Bonanza Power Plant power plant plume was advected to the Horse Pool site, thus linking the observed ozone titration to the NOx-rich power plant plume.

UBOS 2013

TOPAZ was operated on 22 days between 22 January and 18 February 2013 and recorded approximately 230 hours of ozone and aerosol backscatter profile data. Data were collected during most of the diurnal cycle. The ozone and aerosol profiles typically extended up to 2.5 km AGL, except when low clouds were present, which restricted the maximum range of the lidar to the base of the clouds. The lidar was not operated during periods of precipitation and fog. TOPAZ ozone data are posted at http://www.esrl.noaa.gov/csd/groups/csd3/measurements/ubwos13/topaz/. Figure 5-52 gives an overview of all ozone profiles measured during UBOS 2013. Ozone profiles are only shown up to 1000 m AGL to depict the details of the ozone structure in the lowest few hundred meters. Strong lidar signal attenuation due to the high ozone and aerosol concentrations observed in 2013 resulted in small gaps in the spliced ozone (and aerosol backscatter) profiles, shown as white horizontal bars in Figure 5-52. TOPAZ captured the evolution of several high ozone episodes, including their multi-day buildup followed by a partial or complete cleanout of the Uinta Basin due to passing synoptic scale storms. Two complete episodes during the first half of February, the last couple of days of the late January episode, and the first day of ozone buildup starting on 18 February were captured. No data were taken during the 27 January and 8-11 February storms, which were accompanied by precipitation and low clouds. However,

TOPAZ documented the cleanout by a dry cold front on 17 February followed by a quick rebound in ozone (albeit in a very shallow layer) on the next day (see bottom panel of Figure 5-52). From 1 – 7 February, thick fog occurred at the Horse Pool site at night and in the morning, which limited the times when the lidar could be operated.

In contrast to 2012, winter weather conditions during 2013 in the Uinta Basin were more typical, with snow-covered ground and a persistent, shallow cold-pool layer. The strong inversion capping the cold-pool layer coupled with very light boundary layer (BL) winds caused a buildup of pollutants at the Horse Pool site, which after several days led to very high afternoon ozone concentrations of 120 to 150 ppbv. The high ozone episodes came to an end when high winds and strong mixing associated with the storm systems on 27 January, 8 February and 17 February diluted and flushed out the high ozone concentrations. Figure 5-53 shows the time-height cross section of ozone mixing ratio measured with TOPAZ on 17 February when a dry cold front passed over the Horse Pool site around 18:30 MST. This figure also shows the horizontal wind speed and direction profiles observed with the HRDL lidar, which are depicted as wind barbs, color-coded according to wind speed. Strong westerly winds were present above 400 m AGL in the afternoon, which dropped down to the surface in the wake of the passing cold front. As a result, the pollutants in the BL were flushed out and near-surface ozone concentrations dropped from about 130 ppbv to around 50 ppbv in less than one hour. The in situ surface ozone observations from the TECO and NOx cavity ring down instruments at Horse Pool also show this precipitous decrease in ozone.

Figure 5-54 shows 15-minute average ozone profiles for each day TOPAZ was operational. The profiles were observed when BL ozone peaked in the afternoon and are grouped by ozone episode. Despite the snow cover and cold temperatures, the TOPAZ observations show well-mixed ozone profiles up to about 100 m AGL. After several days of pollutant buildup, BL ozone values reached 120-150 ppbv. Above the mixed layer, ozone values gradually decreased to tropospheric background values of around 50 ppbv throughout the several-hundred-meter-deep cold-pool layer and then stayed constant above that up to about 3 km AGL. During the ozone episodes, the lidar observations show no indication of either vertical or horizontal transport of high ozone levels to the surface. This disproves the hypothesis that transport of ozone from outside the Uinta Basin contributes in a significant way to the wintertime high ozone episodes and instead supports the notion that ozone is locally produced in the Uinta Basin.

Just as in 2012, TOPAZ occasionally observed ozone titration as the NOx-rich plume from the nearby Bonanza Power Plant power plant was advected over the Horse Pool site. As an example, Figure 5-55 shows a two-hour time-height cross section from near the surface to 600 m AGL measured with TOPAZ in the evening of 14 February with the coincident ozone tether sonde measurements overlaid. Both lidar and ozone sonde show ozone values below 30 ppbv between 300 and 400 m AGL during a 30-minute period. Contrary to 2012, low ozone values were confined to the upper part of the cold-pool layer above the BL. This suggests that power plant NOx was very likely not part of the precursor mix that led to the high surface ozone values observed in 2013.

5.3.10 Ammonia Measurements

The ammonia sampling took place essentially the last week of the inter-group cooperative study, with integrated samples collected February 18-21, 2013. Samples were collected at the Utah Division of Air Quality sites in Vernal (40.45313°N, 109.50971°W) and Roosevelt (40.29419°N, 110.00897°W), the EPA/Golder Associates site located at Redwash (40.19716°N, 109.35250°W), at the entrance to the Ouray National Wildlife Refuge (40.12827°N, 109.66359°W), and at the main site of the cooperative intensive study, Horse Pool (40.14327°N, 109.46801°W). The samplers were all approximately 1.5 – 3.5 m above ground level and covered with the protective rain/wind cap (refer to Figure 5-4).

As can be seen in Figure 5-56, the observed ambient NH_3 concentrations were quite low, ranging from 0.12 ppb at Horse Pool and Redwash to 1.03 ppb at Vernal, the Uinta Basin's main population center. The Basin-wide average NH_3 concentration was 0.46 ppb. The uncertainty bars in Figure 5-56 represent the range about the median of the duplicate samples at each location; ranges varied from ±0.01 ppb (1.8%) at Roosevelt to ±0.30 ppb (29.6%) at Vernal. Overlaying a contour map of the observed NH_3 concentrations onto a relevant Google Earth image (Figure 5-57) shows that the maximum NH_3 concentrations are observed in the population center of Vernal. The next highest values were observed at the Ouray location, the lowest elevation site, and in Roosevelt the next most significant population center in the Basin. Observed NH_3 concentrations were lowest at the two locations within the oil and gas production areas, Redwash and Horse Pool.

For comparison, Seinfeld and Pandis (1998) and others suggest that typical atmospheric ammonia concentrations are in the range of 0.1 to 10 ppb. Although during inversion episodes it is not expected that that long-range transport would contribute to significant pollutant levels within the Uinta Basin, it can still be informative to examine regional NH_3 levels. The National Atmospheric Deposition Program (NADP) which has been monitoring nationwide precipitation chemistry, including ammonium (NH_4^+), at more than 250 sites since 1978 [*NADP*, 2013a]; unfortunately there is not a monitoring location within the Uinta Basin. However, as can be seen from Figure 5-58, regional NH_4^+ deposition surrounding the target area is expected to be on the low end of the range of observations. In 2007, NADP initiated the Ammonia Monitoring Network (AMoN) which uses passive samplers to determine 2-week integrated ambient NH3 concentrations at about 50 sites around the United States [*NADP*, 2013b]. Once again no sites are located within the Basin, but several sites are within the region and may give insight into regionally expected ambient NH_3 values. Table 5-4 shows AMoN NH_3 concentrations at various nearby locations for February 12-16, 2013, the time period encompassing the study described herein.

As with the NH_3 concentrations observed within the Uinta Basin, Table 5-4 shows the higher, yet still quite low, NH_3 levels associated with the more urban areas. However, the Logan, UT location appears to be an anomaly. The area is a relatively small isolated valley, with a population of approximately 115,000 people and a very strong agricultural base, and with a documented history of high ambient ammonia concentrations [*Moore*, 2007; *Zhu*, 2006].

Sources of atmospheric NH_3 are well-known and include mobile sources (NH_3 is created under reducing conditions in catalytic converters), so-called "slip" from selective catalytic reduction (SCR) systems for NO_x control at power plants, public works such as landfills and wastewater treatment facilities, and agricultural processes. Of these, the agricultural processes are estimated to account for over 80% of the total U.S. ammonia emissions [*EPA*, 2010]. A 2011 emissions inventory for Uintah and Duchesne Counties estimated the annual NH_3 emissions of 684.6 and 715.7 tons/yr, respectively [*P. Barickman*, personal communication, 2013]. Similar to the national statistics, it can be seen in Figure 5-59 that agricultural practices are responsible for the largest fraction of NH_3 emissions. In Uintah County, livestock production accounts for 64.4% of the total annual emissions, while cropped-related practices account for another 10.6% of the NH_3 emissions. For Duchesne County, the two agricultural segments account for 71.9 and 11.5%, respectively.

5.3.11 Aerosol Particle and Snow Measurements

The $PM_{2.5}$ dry mass during UBOS 2012 (January 16- February 27, 2012) varied from 1 to 27 μg m^{-3} with an average during the study of 7.5 ± 6.8 μg m^{-3} (Figure 5-60). The $PM_{2.5}$ gravimetric dry mass was well correlated with the sum of the chemically analyzed mass (slope = 0.97, r^2=0.89), indicating that the chemically measured species accounted for all of the aerosol mass. The average $PM_{2.5}$ dry mass during UBOS 2013 (January 30- February 21, 2013) was 11.7 ± 4.6 μg m^{-3}. The $PM_{2.5}$ gravimetric dry mass was again well correlated with the sum of the chemically analyzed mass (slope = 1.03, r^2=0.94). With the lack of snow in 2012, soil was the dominant aerosol component (44%). However, excluding the larger diameter soil particles, the mass fractions of particulate organic matter (POM), $(NH_4)_2SO_4$, and NH_4NO_3 were very similar in 2012 and 2013 (Figure 5-61). Excluding soil, the average $PM_{2.5}$ concentration in 2013 was 3 times higher than that measured in 2012 (11.3 ± 4.4 μg m^{-3} vs 3.5 ± 2.1 μg m^{-3}). The higher aerosol concentrations are most apparent during the two periods of stagnation centered at February 6 and 15 (Figure 5-60). The mean diameter of the ambient humidity number size distribution was larger in 2013 than in 2012 (Figure 5-62). The larger diameter led to increased aerosol light scattering and a mean $PM_{2.5}$ aerosol surface area that was 4.5 times higher in 2013 than in 2012 (270 μm^2 cm^{-3} vs. 60 μm^2 cm^{-3}). The larger surface area increases the potential for heterogeneous reactions.

Snow chemistry and optical properties were measured during the 2013 study. Nitrate and nitrite concentrations in the surface snow increased with time between snowfalls (Figure 5-63), increasing the acidity of the surface snow and providing a nitrogen source for the potential formation of atmospheric HONO. The increases with time of nitrate and nitrite in the snow were much greater than the other chemical components relative to the component ratios in the atmospheric aerosol suggesting a gas phase source of nitrogen to the snow. Deposition of soil dust during a period of atmospheric turbulent mixing, mid-experiment, increased aerosol light absorption in the snow.

5.3.12 Meteorological Measurements

During the 2012 campaign the lack of snow cover allowed most of the incoming solar radiation to be absorbed by the ground. The resulting surface sensible heat flux driven by this surface heating helped establish well mixed boundary layers that at times exceeded 1.0 km and were documented by the sodar and the NOAA/ESRL/CSD HRDL . Typical peak afternoon surface sensible heat fluxes were on the order of 200 W m^{-2} (Figure 5-64). Snow cover was observed on 19 and 29 February 2012. During those time periods the observed upwelling solar irradiance exceeded 300 W m^{-2} (Figure 5-65). The average surface broadband (.28 – 2.8 μm) albedo measured at Horse Pool during the 2012 intensive observing period was experiment was 0.3.

The first snowfall of the 2012-2013 winter occurred on 18 December 2012. By 10 January 2013 over 10 cm of snow covered the ground at Horse Pool and the ground was frozen to a depth of 20 cm. This snow cover led to strong radiative heat losses from the surface and the formation of strong surface based temperature inversions. Typical daytime surface heat fluxes observed during the 2013 intensive operations period were on the order of 40 W m^{-2} or nearly a factor of five lower than the same period in 2012 (Figure 5-66). The turbulent latent heat fluxes were negligible during the 2013 intensive operations period. The average broadband solar albedo measured at Horse Pool during the 2013 campaign was 0.82 (Fig 5-67). In contrast during the 2012 field season the average albedo was 0.3. The peak down-welling broadband solar irradiance measured at solar noon during the 2013 intensive observation period averaged 650 W m^{-2} (Figure 5-68). Albedos measured over snow covered ground have little spectral dependence in the UV and visible. While the PSD pyranometers do not measure either upwelling or downwelling solar irradiance at wavelengths less than .28 μm, the lack of spectra dependence suggests that albedos at wavelengths associated with photochemistry were at least .80.

5.3.13 Further Analysis of the 2012 Mobile Lab VOC Measurements.

The emissions of volatile organic compounds (VOCs) associated with oil and natural gas production in the Uinta Basin, Utah were measured at the Horse Pool ground site with two PTR-MS instruments, and from the NOAA GMD mobile laboratory with the smaller portable PTR-MS instrument. The NOAA GMD mobile laboratory measured immediately downwind of individual sources: (1) gas well production company A, (2) gas well production company B, (3) oil wells, (4) gas wells in Rangely, CO, (5) a flow back pond of a recently hydraulically fractured well, (6) a newly producing gas well and (7) other point sources including compressor stations, injection wells, tank batteries, evaporation ponds and water treatment plants. This allowed investigation of the emissions from point sources in the Uinta Basin that were responsible for the large mixing ratios of VOCs observed at the Horse Pool ground site.

The track of the mobile laboratory is shown in Figures 5-69b-e color-coded by methane, methanol, toluene, and NO_2, respectively as it moved in close proximity and downwind (indicated by the wind barbs) of a gas well. The corresponding time series are shown in Figure 5-69a. Over 10 ppm of methane, 40 ppbv of toluene and 500 ppbv of methanol were detected close to this particular gas well. These three compounds illustrate the high mixing ratios close to the well and also that different parts of the gas well are responsible for different emissions.

Methane is high downwind of the separator, toluene and other aromatics downwind of the condensate tanks, methanol downwind of the methanol tank and the condensate tanks, and NO_2 downwind of the compressor.

During UBOS 2012 38 different gas wells, 12 oil wells, a newly producing well, a flow back pond from a fracking site, and 17 other point sources such as evaporation ponds, storage tanks and compressor stations were investigated in a similar way as described for the gas well in Figure 5-69. The maximum observed mixing ratios close to the sources for some selected VOCs are shown in Figure 5-70. The mixing ratios of the measured VOCs were averaged during the time the mobile laboratory spent in close proximity, generally within 300 feet, of the wells or the other emission sources and the results are shown in Figure 5-71, summarized for all source categories. Highly elevated mixing ratios of the measured VOCs were found at almost all source locations, but very large differences even between similar point sources existed. The largest relative differences were observed between individual gas wells.

Quantitative comparison of the mobile lab data with the WRAP inventory and with the Horse Pool VOC data is not possible at his time since the mobile lab data did not generate emission rates. However, some qualitative conclusions can be drawn. VOCs emitted by oil wells consisted of heavier compounds compared to gas wells, due to the heavier composition of the liquid extracted by oil wells compared to gas wells. The gas well pad emissions resembled most closely raw gas, but were heavier in composition (i.e, had a higher proportion of larger HCs). Oil well emissions were still heavier, and the main differences compared to gas wells were the aromatic compounds. Collectively, the measurements from oil and gas wells and at Horse Pool were a mixture of raw gas (from the pneumatic devices and pumps and other venting sources) and tank flashing and dehydrator emission, similar to what the WRAP inventory shows. The measurements were broadly consistent with the WRAP inventory: (1) the inventory correctly identifies dehydrators, tank flashing and the pneumatic devices as the major VOC emission sources from the gas and oil wells, (2) oil and condensate tanks emit heavier compounds such as toluene and (3) wellhead, dehydrator and pneumatic devices emit lighter compounds such as methane and light alkanes.

5.4 References

Allwine, K. J., and C. D. Whiteman (1994), Single-station integral measures of atmospheric stagnation, recirculation and ventilation. , *Atmos. Eviron.*, *28*, 713-721.

Altshuller, A. P. (1993), PANs in the atmosphere, *J. Air & Waste Manag. Assoc.*, *43*, 1221-1230, doi:10.1080/1073161X.1993.10467199.

Alvarez II, R. J., et al. (2011), Development and application of a compact, tunable, solid-state airborne ozone lidar system for boundary layer profiling, *J. Atmos. Oceanic Technol.*, doi:10.1175/JTECH-D-10- 05044.1.

Alvarez, R. J., C. J. Senff, A. M. Weickmann, S. P. Sandberg, A. O. Langford, R. D. Marchbanks, W. A. Brewer, and R. M. Hardesty (2012), Reconfiguration of the NOAA TOPAZ Lidar for Ground-based Measurement of Ozone and Aerosol Backscatter, paper presented at The 26th International Laser Radar Conference, Porto Heli, Greece, 25-29 June, 2012.

Ammann, M., R. Atkinson, R. A. Cox, J. N. Crowley, R. Hynes, M. E. Jenkin, W. Mellouki, M. J. Rossi, J. Troe, and T. Wallington (2103), Evaluated Kinetic Data*Rep.*, IUPAC Subcommittee for Gas Kinetic Data Evaluation.

Atkinson, R., and J. Arey (2003), Atmospheric degradation of volatile organic compounds, *Chemical Reviews*, *103*(12), 4605-4638, doi:10.1021/cr0206420

Atkinson, R., and S. M. Aschmann (1984), Rate constants for the reactions of O_3 and OH radicals with a series of alkynes, *Int. J. Chem. Kinet.*, *16*, 259-268, doi:10.1002/kin.550160308.

Banta, R. M., L. S. Darby, J. D. Fast, J. O. Pinto, C. D. Whiteman, W. J. Shaw, and B. D. Orr (2004), Nocturnal low-level jet in a mountain basin complex. Part I: Evolution and implications to other flow features, *J. Appl. Meteor.*, *43*, 1348-1365.

Banta, R. M., et al. (2011), Dependence of daily peak O3 concentrations near Houston, Texas on environmental factors: Wind speed, temperature, and boundary-layer depth, *Atmos. Environ.*, *45*, 162-173.

Banta, R. M., et al. (1998), Daytime buildup and nighttime transport of urban ozone in the boundary layer during a stagnation episode, *J. Geophys. Res.*, *103*, 22,1598-1522,1544.

Bates, T. S., et al. (2008), Boundary layer aerosol chemistry during TexAQS/GoMACCS 2006: Insights into aerosol sources and transformation processes, *J. Geophys. Res.*, *113*, D00F01, doi:10.1029/2008JD010023.

Beine, H., A. J. Colussi, A. Amoroso, G. Esposito, M. Montagnoli, and M. R. Hoffmann (2008), HONO emissions from snow surfaces, *Environ. Res. Lett.*, *3*, 1-6, doi:10.1088/1748-9326/3/4/045005.

Day, D. A., P. J. Wooldridge, M. B. Dillon, J. A. Thornton, and R. C. Cohen (2002), A thermal dissociation laser-induced fluorescence instrument for in situ detection of NO_2, peroxy nitrates, alkyl nitrates, and HNO_3, *Journal of Geophysical Research-Atmospheres*, *107*(D5-6), 4046, doi: 4010.1029/2001JD000779.

de Gouw, J. A., and C. Warneke (2007), Measurements of volatile organic compounds in the earths atmosphere using proton-transfer-reaction mass spectrometry, *Mass Spectrometry Reviews*, *26*(2), 223-257.

Edwards, P. M., et al. (2013), Ozone photochemistry in an oil and natural gas extraction region during winter: Simulations of a snow-free season in the Uintah Basin, Utah, *Atmos. Chem. Phys.*, *13*, 8955-8971.

EPA, U. (1999), Compendium of Methods for the Determination of Toxic Organic Compounds in Ambient Air, 2nd Edition, Compendium Method TO-11A, Determination of Formaldehyde in Ambient Air Using Adsorbent Cartridge Followed by High Performance Liquid Chromatography (HPLC) - [Active Sampling Methodology].*Rep. EPA/625/R-96/010b*.

EPA, U. (2010), Our Nation's Air: Status and Trends through 2008*Rep.*, pp6. pp.

Finlayson-Pitts, B. J., and J. N. J. Pitts (2000), *Chemistry of the Upper and Lower Atmosphere*, Academic Press, San Diego.

Gilman, J. B., et al. (2010), Ozone variability and halogen oxidation within the Arctic and sub-Arctic springtime boundary layer, *Atmos. Chem. Phys.*, *10*(21), 10223-10236, doi:10.5194/acp-10-10223-2010.

Gilman, J. B., B. M. Lerner, W. C. Kuster, and J. A. de Gouw (2013), Source Signature of Volatile Organic Compounds from Oil and Natural Gas Operations in Northeastern Colorado, *Environ. Sci. Technol.*, *47*(3), 1297-1305, doi:10.1021/es304119a.

Graus, M., M. Muller, and A. Hansel (2010), High resolution PTR-TOF: Quantification and formula confirmation of VOC in real time, *J. Am Soc. Mass. Spectrom.*, *21*, 1037-1044.

Grenfell, T. C., S. J. Doherty, A. D. Clarke, and S. G. Warren (2011), Light absorption from particulate impurities in snow and ice determined by spectrophotometric analysis of filters, *Appl. Opt.*, *50*, 2037-2048.

Grund, C. J., R. M. Banta, J. L. George, J. N. Howell, M. J. Post, R. A. Richter, and A. M. Weickmann (2001), High-resolution Doppler lidar for boundary layer and cloud research, *J. Atmos. Ocean. Technol.*, *18*, 376-393.

Honrath, R. E., Y. Lu, M. C. Peterson, J. E. Dibb, M. A. Arsenault, N. J. Cullen, and K. Steffen (2002), Vertical fluxes of NO_x, HONO, and HNO_3 above the snowpack at Summit, Greenland, *Atmos. Environ.*, *36*, 2629-2640.

Langford, A. O., C. J. Senff, R. J. Alvarez II, R. M. Banta, R. M. Hardesty, D. D. Parrish, and T. B. Ryerson (2011), Comparison between the TOPAZ airborne ozone lidar and in situ measurements during TexAQS 2006, *J. Atmos. Ocean. Technol.*, *28*, doi:10.1175/JTECH-D-10-05043.1.

Li, S., J. Matthews, and A. Sinha (2008), Atmospheric Hydroxyl Radical Production from Electronically Excited NO_2 and H_2O, *Science*, *319*(5870), 1657-1660, doi:10.1126/science.1151443.

Liu, S. C., J. R. McAfee, and R. J. Cicerone (1984), Radon 222 and tropospheric vertical transport, *Journal of Geophysical Research: Atmospheres*, *89*(D5), 7291-7297, doi:10.1029/JD089iD05p07291.

Lyman, S., and H. Shorthill (2013), Final Report 2012 Uintah Basin Winter Ozone & Air Quality Study Rep., Utah State University, Vernal, UT.

Maljanen, M., P. Yli-Pirila, J. Hytonen, J. Joutensaari, and P. J. Martikainen (2013), Acidic northern soils as sources of atmospheric nitrous acid (HONO), *Soil Biol. & Biochem.*, *in press*, doi:10.1016/j.soilbio.2013.08.013.

Martin, R., K. Moore, M. M., S. Hill, K. Harper, and H. Shorthill (2011), Final Report: Uinta Basin Winter Ozone and Air Quality Study: December 2010 – March 2011*Rep.*, Energy Dynamics Laboratory, Bingham Research Center, Utah State University Research Foundation (USURF), , Vernal, UT.

McLaren, R., et al. (2012), Vertical profiles of $ClNO_2$ at a remote terrestrial site: evidence of dry deposition of N_2O_5 as a source of $ClNO_2$?, in *Fall Meeting of the American Geophysical Union*, edited, San Francisco.

Moore, K. D. (2007), Derivation of agricultural gas-phase ammonia emissions and application to the Cache Valley, Utah State University, Logan, UT.

Müller, M., T. Mikoviny, W. Jud, B. D. D'Anna, and A. Wisthaler (2013), A New Software Tool for the Analysis of High Resolution PTR-TOF Mass Spectra, *Chemomet. Intell. Lab Sys.*, doi:10.1016/j.chemolab.2013.06.011.

Paulot, F., et al. (2011), Importance of secondary sources in the atmospheric budgets of formic and acetic acids, *Atmos. Chem. Phys.*, *11*(5), 1989-2013, doi:10.5194/acp-11-1989-2011.

Petron, G., et al. (2012), Hydrocarbon emissions characterization in the Colorado Front Range: A pilot study, *J. Geophys. Res.*, *117*, D04304, doi:10.1029/2011JD016360.

NADP (2013a), National Trends Network (NTN), , edited.

NADP (2013b), National Trends Network (AMoN), edited, doi:http://nadp.sws.uiuc.edu/AMoN/.

Rappenglück, B., et al. (2013), Strong wintertime ozone events in the Upper Green River Basin, Wyoming, *Atmos. Chem. Phys. Discuss.*, *13*, 17953-18005, doi:10.5194/acpd-13-17953-2013.

Reese, E. (2009), Comparison of Agricultural Area Source Ammonia Gas Concentration and Measurement Fluxes, MS Thesis, Utah State University, Logan, UT.

Roadman, M. J., J. R. Scudlark, J. J. Meisinger, and W. J. Ullman (2003), Validation of Ogawa passive samplers for the determination of gaseous ammonia concentrations in agricultural settings., *Atmos. Environ.*, *37*, 2317-2325.

Roberts, J.M., et al. (1995), Relationships between PAN and ozone at sites in eastern North America, *Journal of Geophysical Research*, *100*(D11), 22821-22830.

Roberts, J. M. (2007), Peroxyacetic Nitric Anhydride (PAN) and Related Compounds, in *Volatile Organic Compounds in the Atmosphere*, edited by R. Koppmann, pp. 221-268, Blackwell, London.

Roberts, J. M., et al. (2010), Measurement of HONO, HNCO, and other inorganic acids by negative-ion proton-transfer chemical-ionization mass spectrometry (NI-PT-CIMS): Application to biomass burning emissions., *Atmos. Meas. Tech.*, *3*, 981-990, doi:10.5194/amt-3-981-2010.

Roberts, J. M., et al. (2013), Chapter 3. Intensive Measurements at the Horse Pool Site, in *Final report: 2012 Uintah Basin Winter Ozone & Air Quality Study*, edited by S. Lyman and H. Shorthill, pp. 97-174, Utah State University.

Seinfeld, J. H., and S. N. Pandis (1998), *Atmospheric Chemistry and Physics: From Air Pollution to Climate Change*, John Wiley & Sons, Inc., New York.

Senff, C. J., R. J. Alvarez II, R. M. Hardesty, R. M. Banta, and A. O. Langford (2010), Airborne lidar measurements of ozone flux downwind of Houston and Dallas, *J. Geophys. Res.*, *115*, D20307, doi:10.1029/2009JD013689.

Sommariva, R., J. A. de Gouw, M. Trainer, E. Atlas, P. D. Goldan, W. C. Kuster, C. Warneke, and F. C. Fehsenfeld (2011), Emissions and photochemistry of oxygenated VOCs in urban plumes in the Northeastern United States, *Atmos. Chem. Phys.*, *11*(14), 7081-7096, doi:10.5194/acp-11-7081-2011.

Stavrakou, T., et al. (2012), Satellite evidence for a large source of formic acid from boreal and tropical forests, *Nature Geosci*, *5*(1), 26-30, doi:http://www.nature.com/ngeo/journal/v5/n1/abs/ngeo1354.html - supplementary-information.

Su, H., Y. Cheng, R. Oswald, T. Behrendt, I. Trebs, F. X. Meixner, M. O. Andreae, P. Cheng, Y. Zhang, and U. Pöschl (2011), Soil Nitrite as a Source of Atmospheric HONO and OH Radicals, *Science*, doi:10.1126/science.1207687.

Tucker, S. C., W. A. Brewer, R. M. Banta, C. J. Senff, and S. P. Sandberg (2009), Doppler lidar estimation of mixing height using turbulence, shear, and aerosol profiles, *J. Atmos. Ocean. Technol.*, *26*, 673-688.

UBWOS (2013), Final Report: 2012 Uintah Basin Winter Ozone & Air Quality Report, *Rep.*, 65-68, 153-154, 163-165 pp.

VandenBoer, T. C., et al. (2013), Understanding the role of the ground surface in HONO vertical structure: High resolution vertical profiles during NACHTT 2011, *J. Geophys. Res.*, *118*, doi:10.1002/jgrd.50721, 2013.

Veres, P., J. B. Gilman, J. M. Roberts, W. C. Kuster, C. Warneke, I. R. Burling, and J. de Gouw (2010), Development and validation of a portable gas phase standard generation and calibration system for volatile organic compounds, *Atmospheric Measurement Techniques*, *3*(3), 683-691, doi:10.5194/amt-3-683-2010.

Whiteman, C. D., X. Bian, and S. Zhong (1999), Wintertime evolution of the temperature inversion in the Colorado Plateau Basin., *J. Appl. Meteor.*, *38*, 1103-1117.

Williams, J., et al. (1997), Regional ozone from biogenic hydrocarbons deduced from airborne measurements of PAN, PPN, and MPAN, *Geophysical Research Letters*, *24*(9), 1099-1102.

Young, C. J., et al. (2012), Vertically resolved measurements of nighttime radical reservoirs in L

Los Angeles and their contribution to the urban radical budget, *Environ. Sci. Technol.*, *46*, 10965-10973, doi:10.1021/es302206a.

Zhou, X., et al. (2011), Nitric acid photolysis on forest canopy surface as a source for tropospheric nitrous acid, *Nature Geosci*, *4*(7), 440-443.

Zhu, D. (2006), Analysis of wintertime gas- and particle-phase ammonia in association with $PM_{2.5}$ formation in the Cache Valley,, MS thesis, Utah State University, Logan, UT.

TABLES

Table 5-1. Chemical measurements made during the 2013 Horse Pool Intensive Study

Measurement	Method	P.I.	Time Resol.	Det. Limit, ppbv
Gas-Phase Measurements				
O_3, NO, NO_2, NO_3, N_2O_5,	Cavity Ring-Down Spectroscopy	Brown	1 sec	0.01 – 0.1
O_3	Lidar	Senff/Lang-ford	15 min	N/A
Acyl Peroxynitrates Nitryl Chloride ($ClNO_2$)	Iodide ion Chemical Ionization Mass Spectrometry	Roberts/ Veres	1-5 sec	0.005
CO_2, CH_4, H_2S	Integrated Cavity Output Spectroscopy	Soltis/ Roberts/ de Gouw	1 sec	10 – 1000
SO_2	UV fluorescence	Roberts/ Williams	1 min	0.1 ppbv
Formaldehyde, Oxygenates, Aromatics, Acetonitrile	Proton-Transfer Reaction Mass Spectrometry Quadrupole MS Time-of-Flight MS	Warneke/ de Gouw Murphy/ Veres	10sec - 1 min 0.1sec-10sec	0.01
C_2-C_{10} VOCs	On site GC/FID,	Koss/ de Gouw	30 min	0.005 - 0.01
Acids: HNO_3, HCl, HONO, HNCO, carboxylic acids,	Negative Ion Proton Transfer Mass Spectrometry	Yuan/ Warneke/ de Gouw/ Roberts	1- 10 sec	0.01
Aerosol/Condensed Phase Measurements				
Size-Resolved Aerosol Surface Area	Scanning mobility particle sizer, aerodynamic particle sizer	Bates/ Quinn	5 min	
Organic carbon/ Elemental carbon	Impactor/denuder sampling, thermal/optical analyzer	"	1 min	
Cations/anions	Impactor sampling/ion chromatography	"		
Cations/anions	Particle-into-liquid-sampler/ion chromatography	"		
Gravimetric mass Trace Elements	Impactor/microbalance/x-ray emission spectrometry	"		
Condensation Nuclei	Condensation nuclei counter	"	1 min	
Light scattering and absorption	Nephelometer, absorption photometer	"		
Aerosol Backscatter	Lidar	Senff/ Langford		
SnowComposition:		Bates/ Quinn		
Anions/Cations	Grab Sampling, Ion chromatography	"	N/A	

Measurement	Method	P.I.	Time Resol.	Det. Limit, ppbv
Organic Carbon/ Total Nitrogen	Combustion/catalytic oxidation	"	N/A	
Light Absorbing Aerosols	Integrated-sandwich spectrophotometer	"	N/A	

Table 5-2. Meteorological measurements made during the 2013 Horse Pool Intensive Study.

Measurement	Location	P.I.	Time Resol.
High resolution 3-D Winds	Range 2-5km	Banta	15-20 min
Air Temperature	2, 9, 18 meters	King/ Zamora	1 min
Soil Temperature	5, 10, 20 cm	"	
Pressure		"	
Snow Depth		"	
Wind Speed/Direction	Sonic Anemometers, 9 and 18 meters	"	1 sec
Precipitation		"	1 min
PBL depth	SODAR	"	1 min
Net Radiation/Albedo		"	1 min
Photolysis Rates	Filter Radiometry, Down-welling	Hübler	1 min

Table 5-3. High Resolution Doppler Lidar technical specifications.

Wavelength	2.0218 µm
Pulse energy	1.5 mJ
Pulse rate	200 Hz
Pulse width	200 ns
Scan	Upper hemisphere
Range resolution	30 m
Time resolution	0.02 s
Velocity precision	5 cm s^{-1}
Minimum range	0.2 km
Maximum range	2- 9 km (typically 3 km)
Laser	Tm:Lu, YAG diode-pumped, injection-seeded laser

Table 5-4. AMoN ambient ammonia concentrations from areas near the Uinta Basin (NADP, 2013b).

Site Name	NADP ID	Air miles from Vernal, UT	NH_3 (ppb)
Logan, UT	UT01	150	38.2
Salt Lake City, UT	UT97	132	3.6
Grand Teton National Park, WY	WY94	238	0.6
Brooklyn Lake, WY	WY95	182	0.4
Craters of the Moon National Monument, ID	ID03	294	1.0
Ft. Collins, CO	CO13	230	3.0
Rocky Mtn National Park (Long's Pk), CO	CO88	210	0.4

FIGURES

5-1. A picture of the UBOS 2013 Horse Pool Intensive site facing North. The individual components are (A) sample tower with automated inlet, (B) NOAA/CSD nitrogen species trailer, (C) NOAA/CSD VOC trailer, (D) NOAA/PMEL aerosol and snow lab, (E) NOAA/CSD HRDLS trailer, (F) NOAA/CSD TOPAZ trailer. Photo credit, Scott Sandberg.

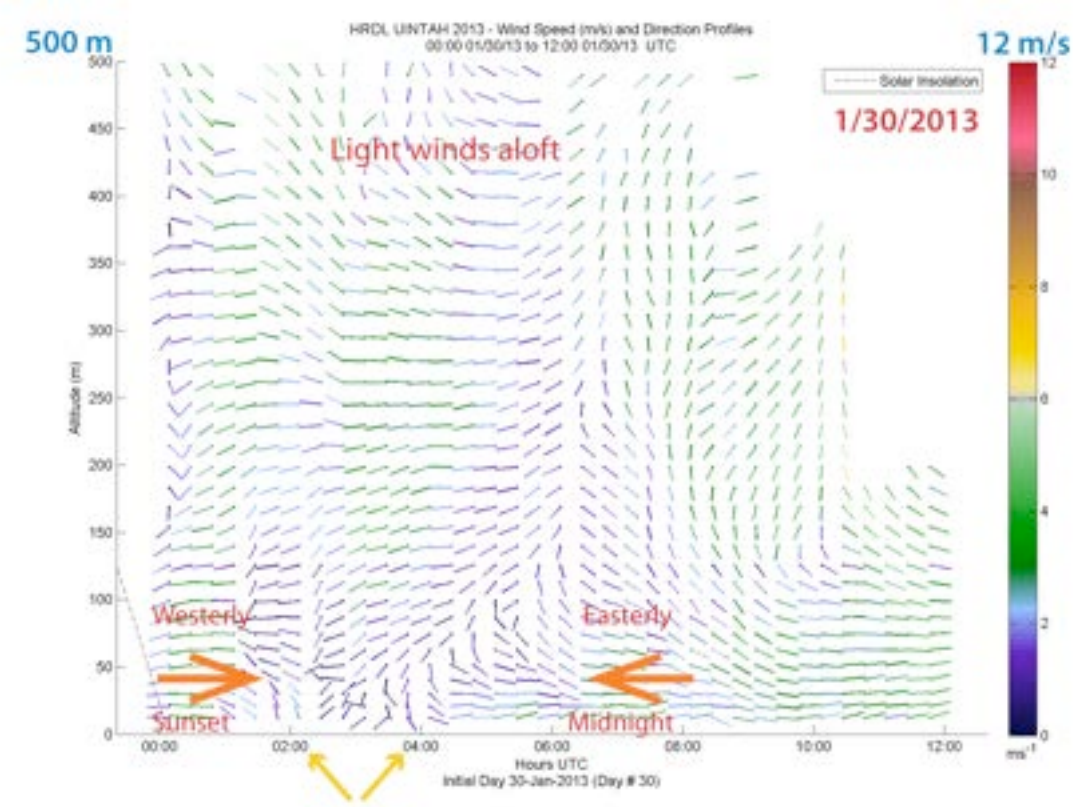

5-2. Time-height cross section of wind speed and direction on 30 January for 0000-1200 UTC (29/1700-30/0500 MST), using 20-min vertical profiles from HRDL conical scans. Wind barbs point toward direction from which winds were blowing, and color of barbs indicates wind speeds (m s^{-1}) as shown in color bar at right. Dashed line (left side of figure) indicates relative solar insolation, declining in late afternoon.

5-3. Truck-mounted TOPAZ ozone lidar with roof-top, two-axis scanner.

5-4. Deployed Ogawa passive sampler without and with rain/wind cap.

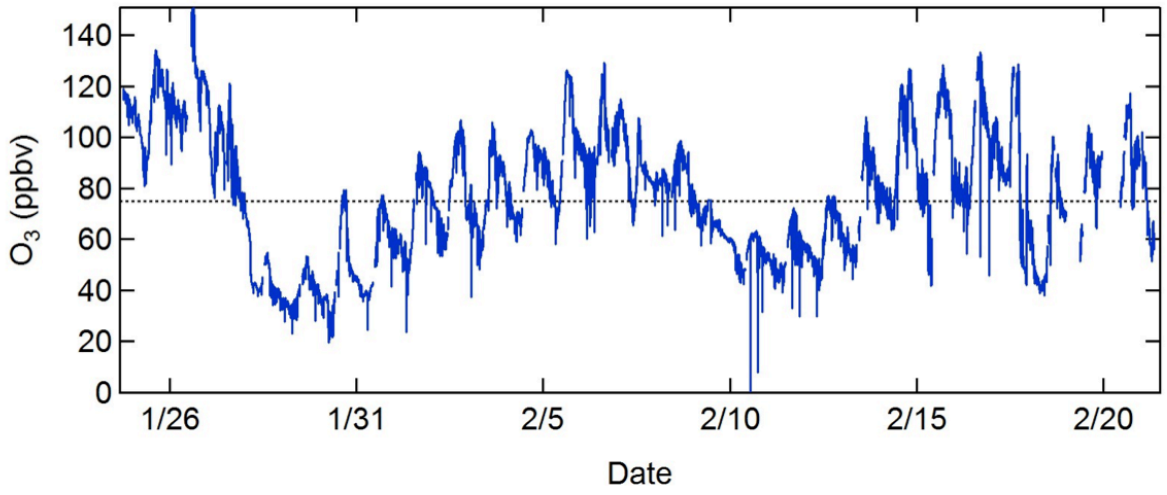

5-5. Times series of O_3 measured at the Horse Pool site by the CaRDS instrument during the UBOS 2013 campaign.

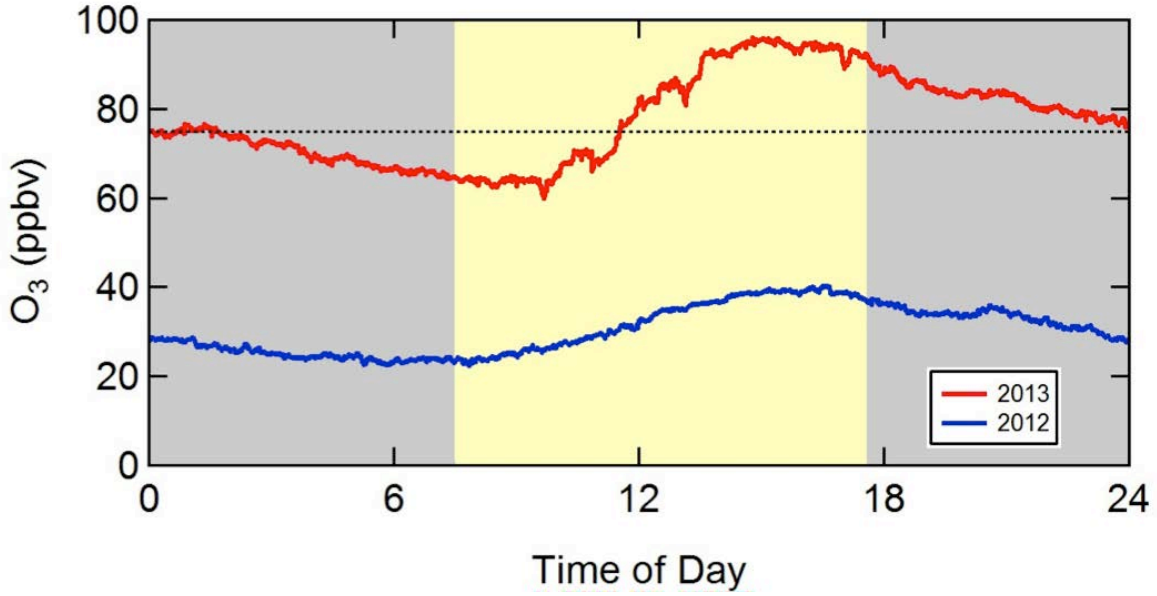

5-6. Diurnal averages of O_3 during the campaigns in 2012 (blue) and 2013 (red). The average daylight period is shown in yellow.

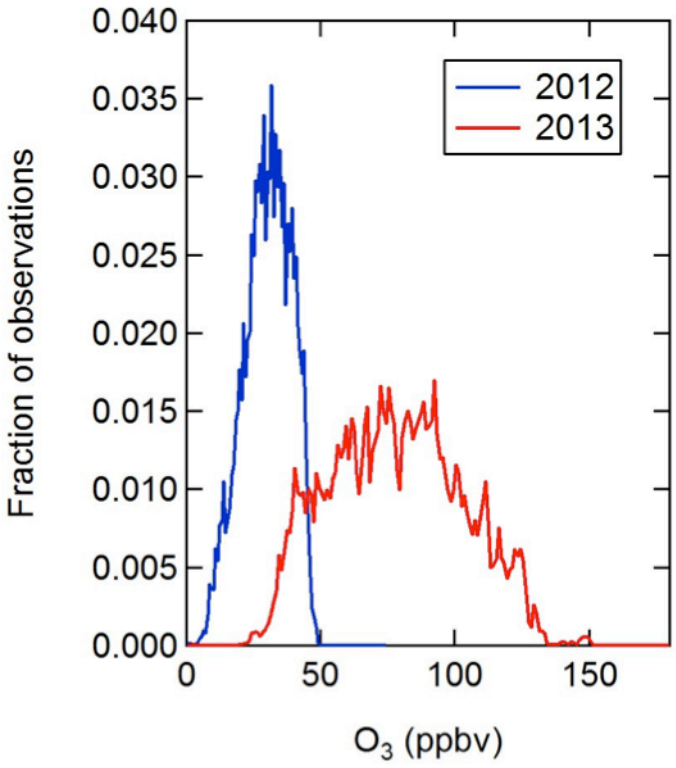

5-7. Comparison of O_3 distributions measured in 2012 (blue) versus 2013 (red).

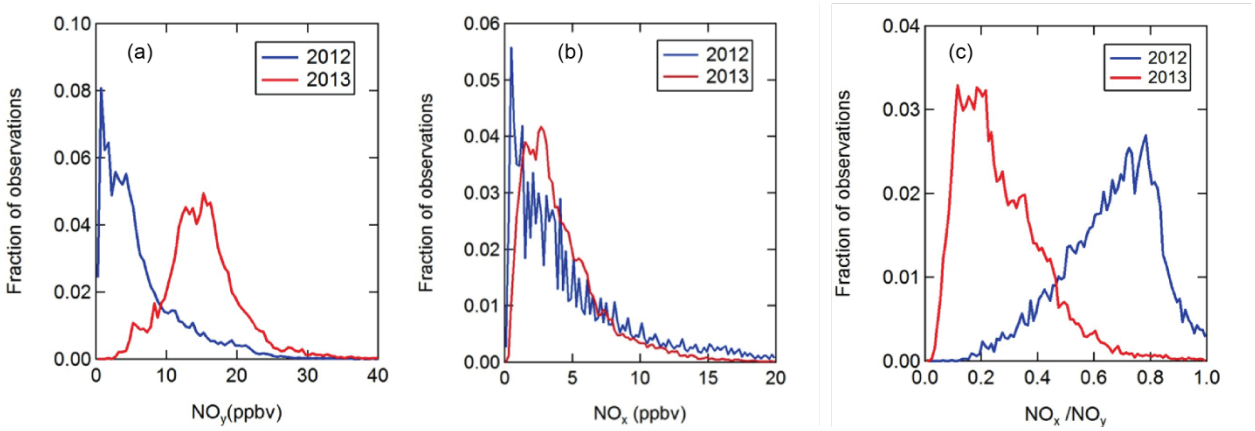

5-8a-c. The distributions of (a) total NO_y, (b) NO_x, and (c) the ratio NO_x/NO_y. The UBOS 2012 data are in blue and the UBOS 2013 data are in red.

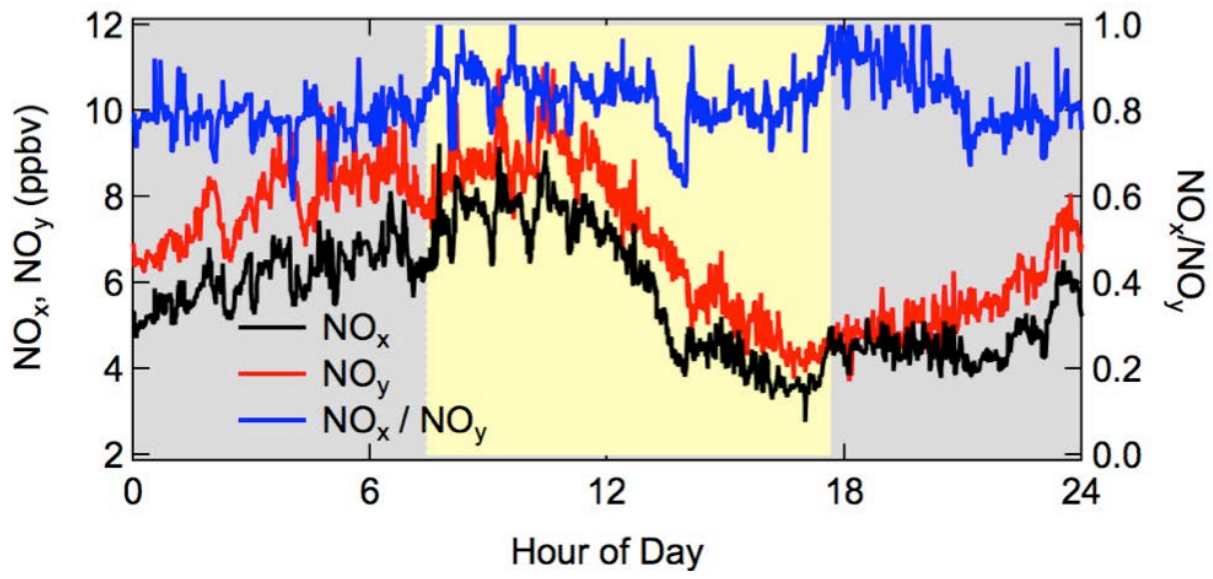

5-9. Diurnal plot of NO_x, NO_y and NO_x/NO_y measured during the 2012 campaign.

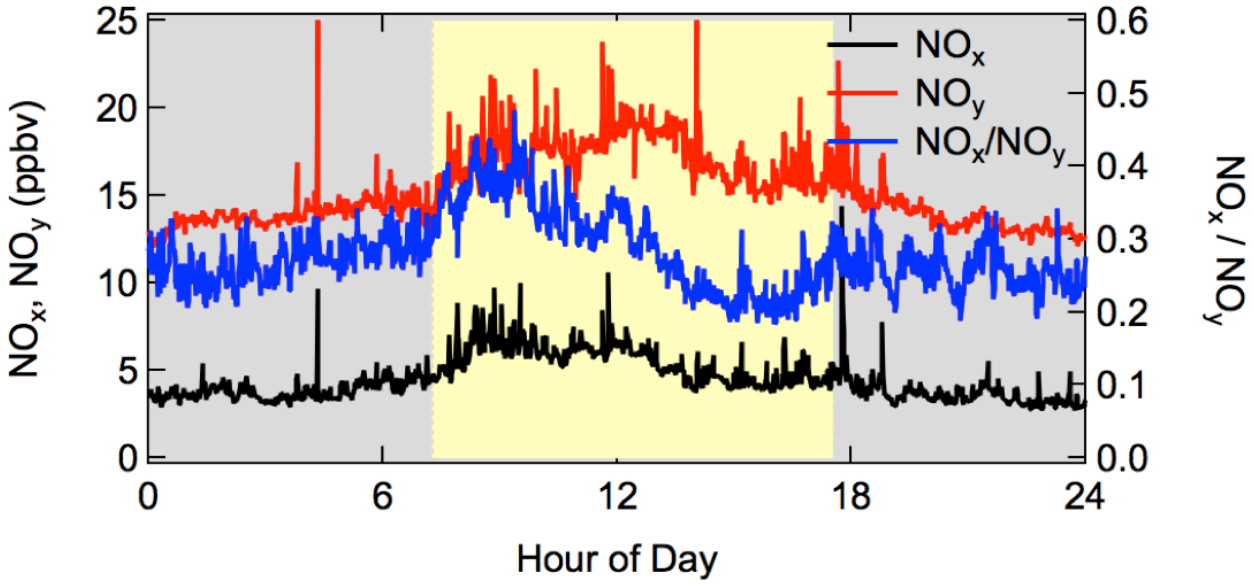

5-10. Diurnal plot of NO_x, NO_y and NO_x/NO_y measured during the 2013 campaign.

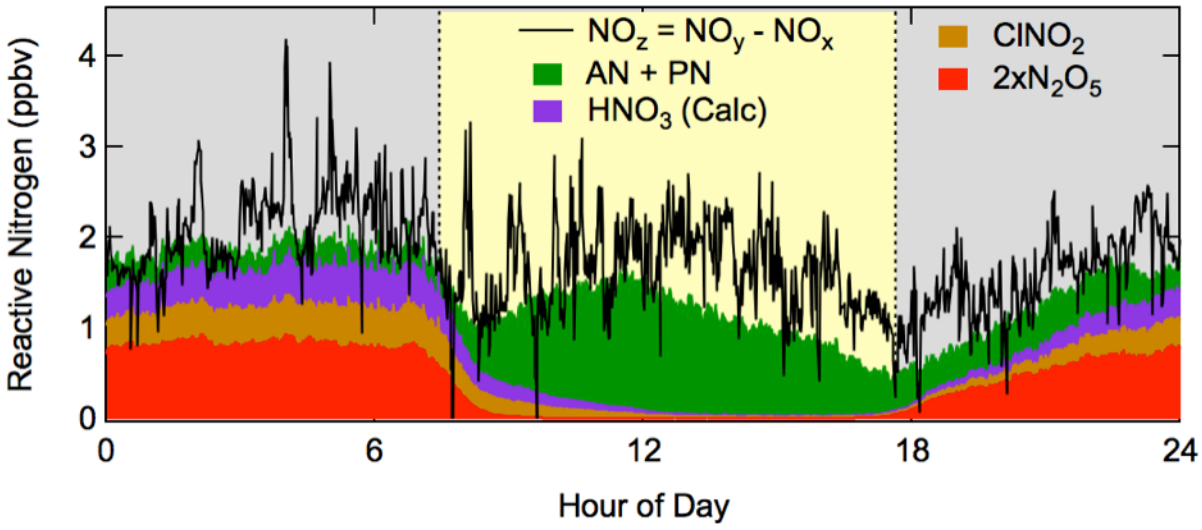

5-11. The average diurnal composition of NO_z measured during the UBOS 2012 campaign. NOx is in black, NOy is in red and the ratio NOx/NOy is in blue.

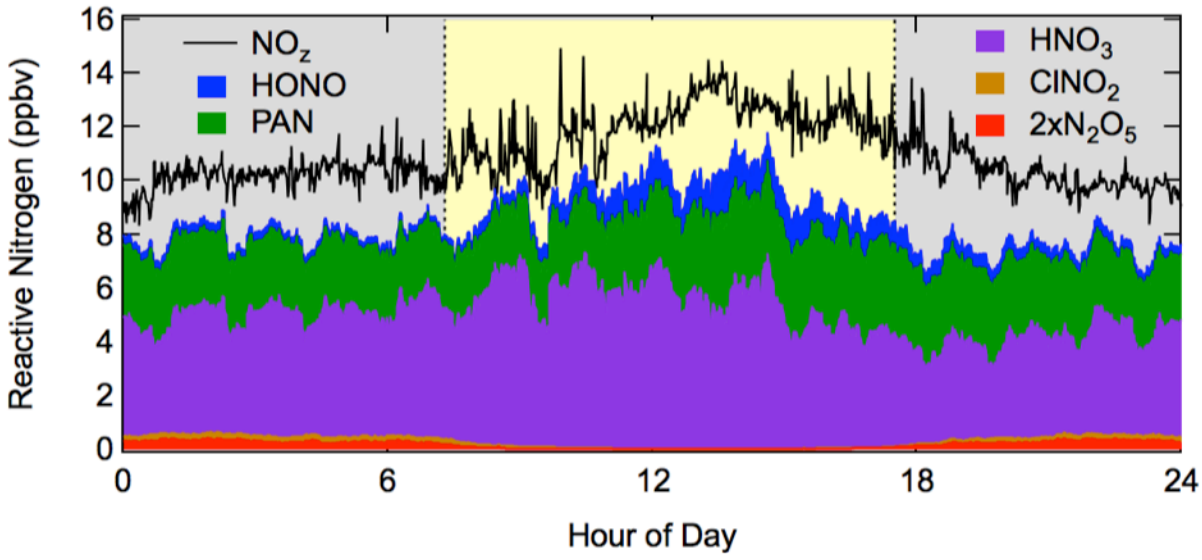

5-12. The average diurnal composition of NO_z measured during the UBOS 2013 campaign. NOx is in black, NOy is in red and the ratio NOx/NOy is in blue.

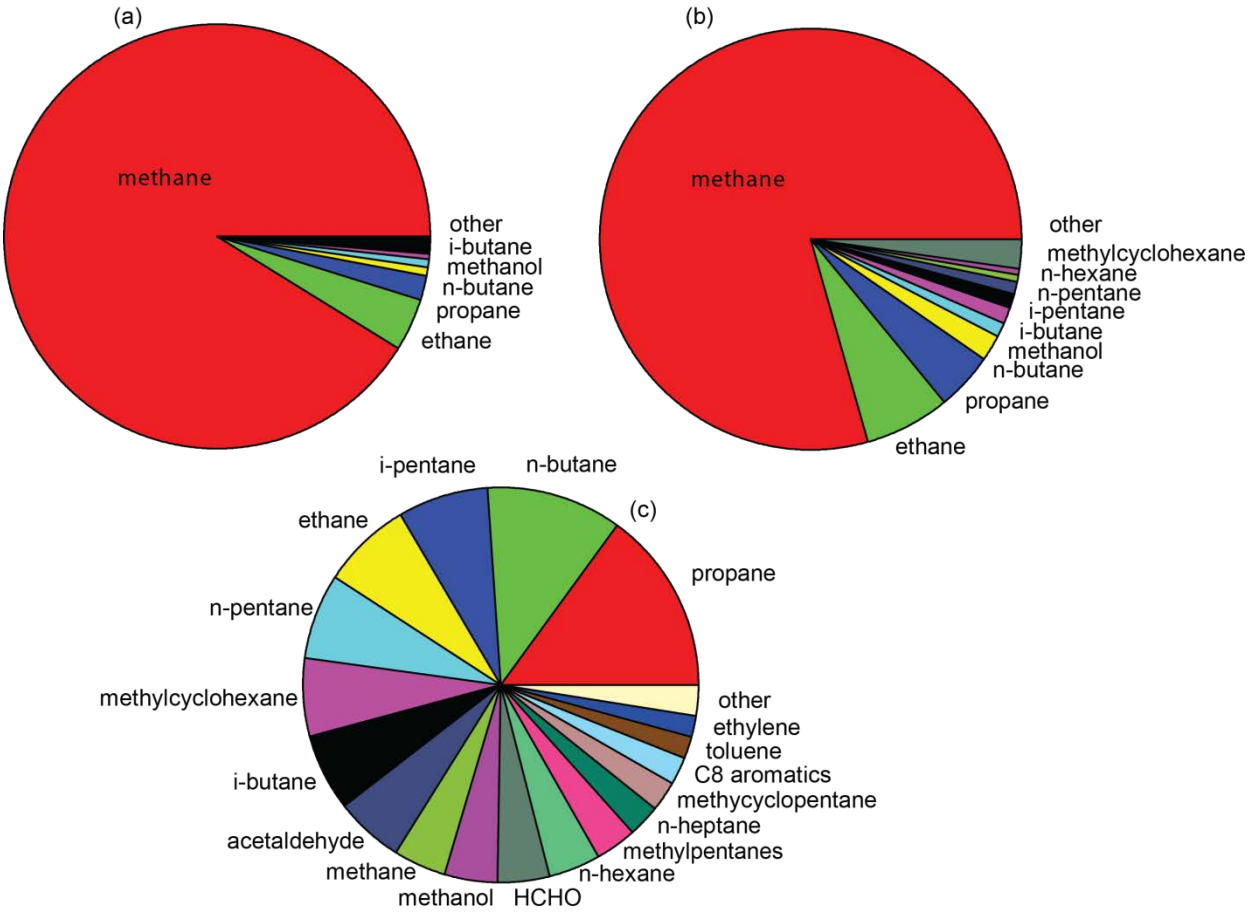

5-13. VOC composition by molar abundance (volume) (A) and mass (B), and OH reactivity (C) measured during UBOS 2013.

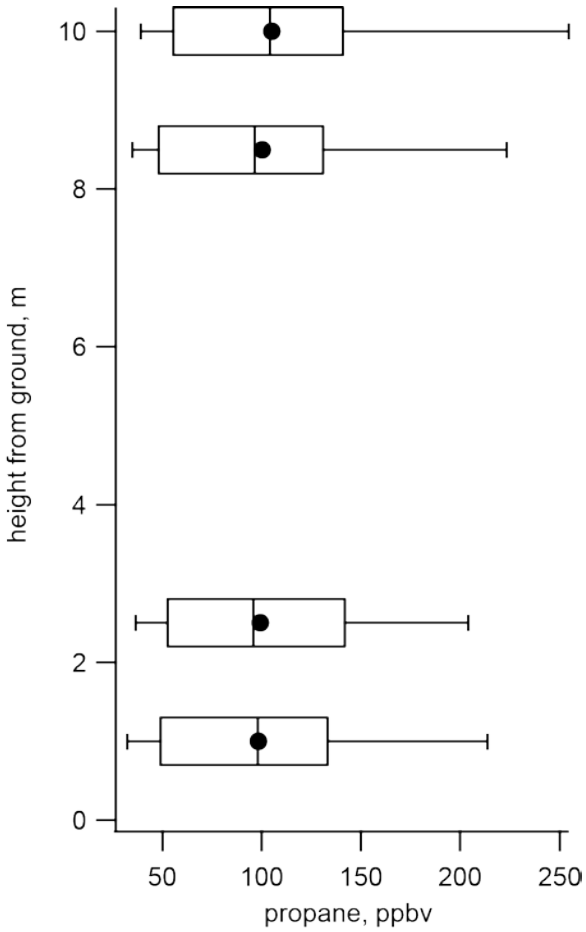

5-14. Propane measured as a function of inlet height during the periods of height profiling.

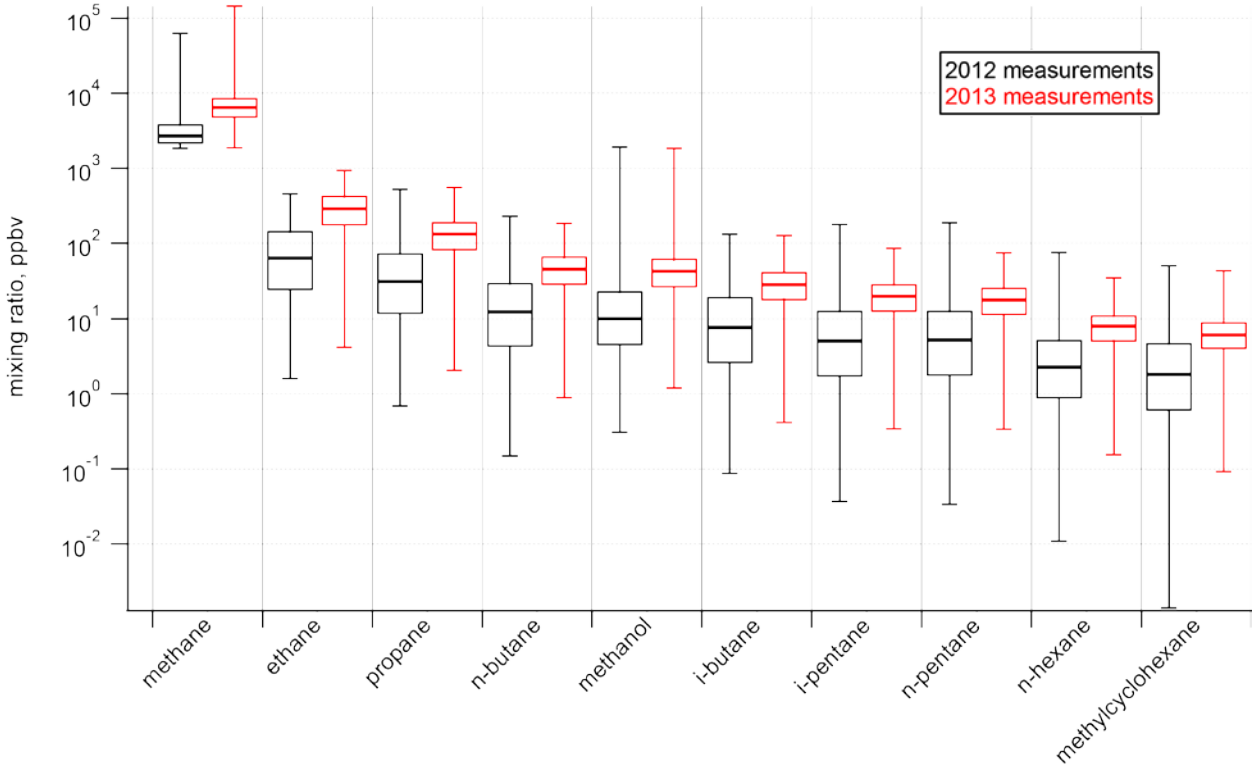

5.15. Comparison between UBOS 2012 (black) and UBOS 2013 (red) of the absolute mixing ratios of compounds with the highest concentrations.

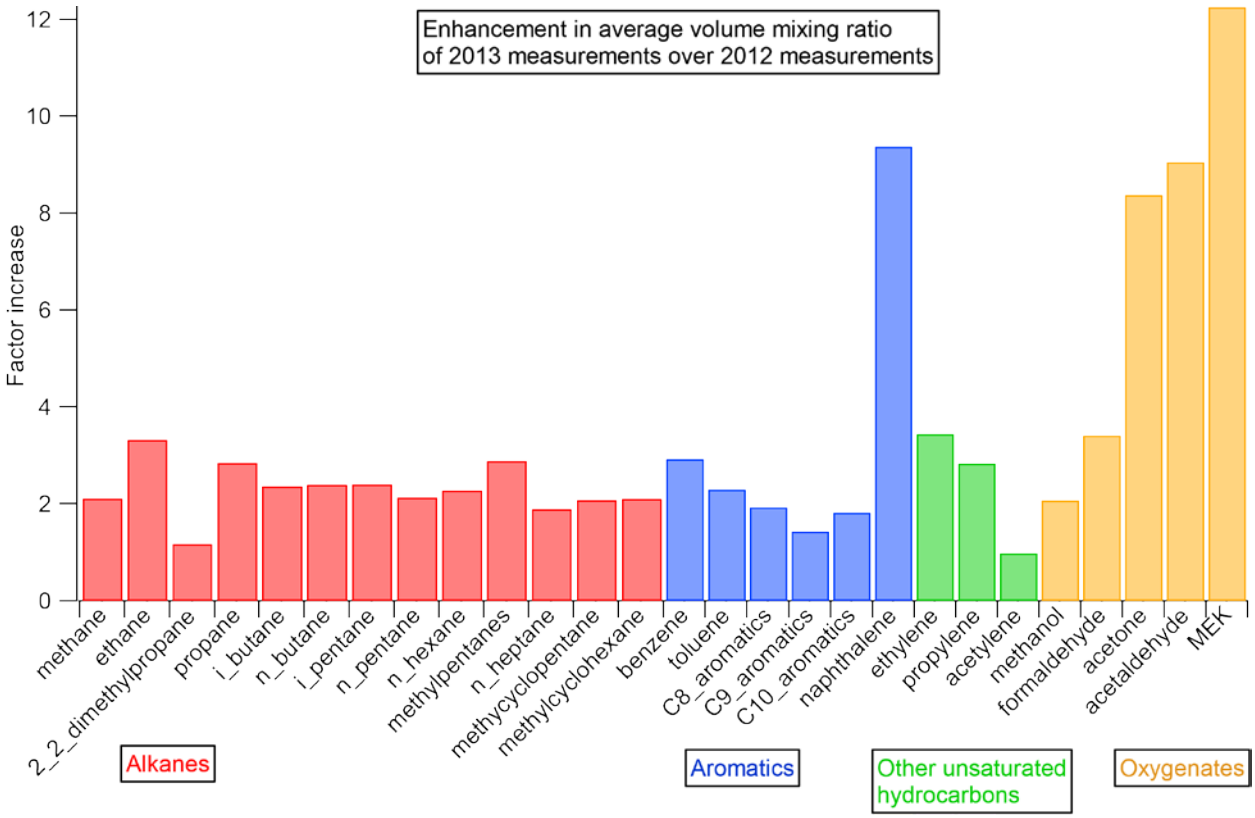

5-16. The fractional increase from 2012 to 2013 of all measured VOCs.

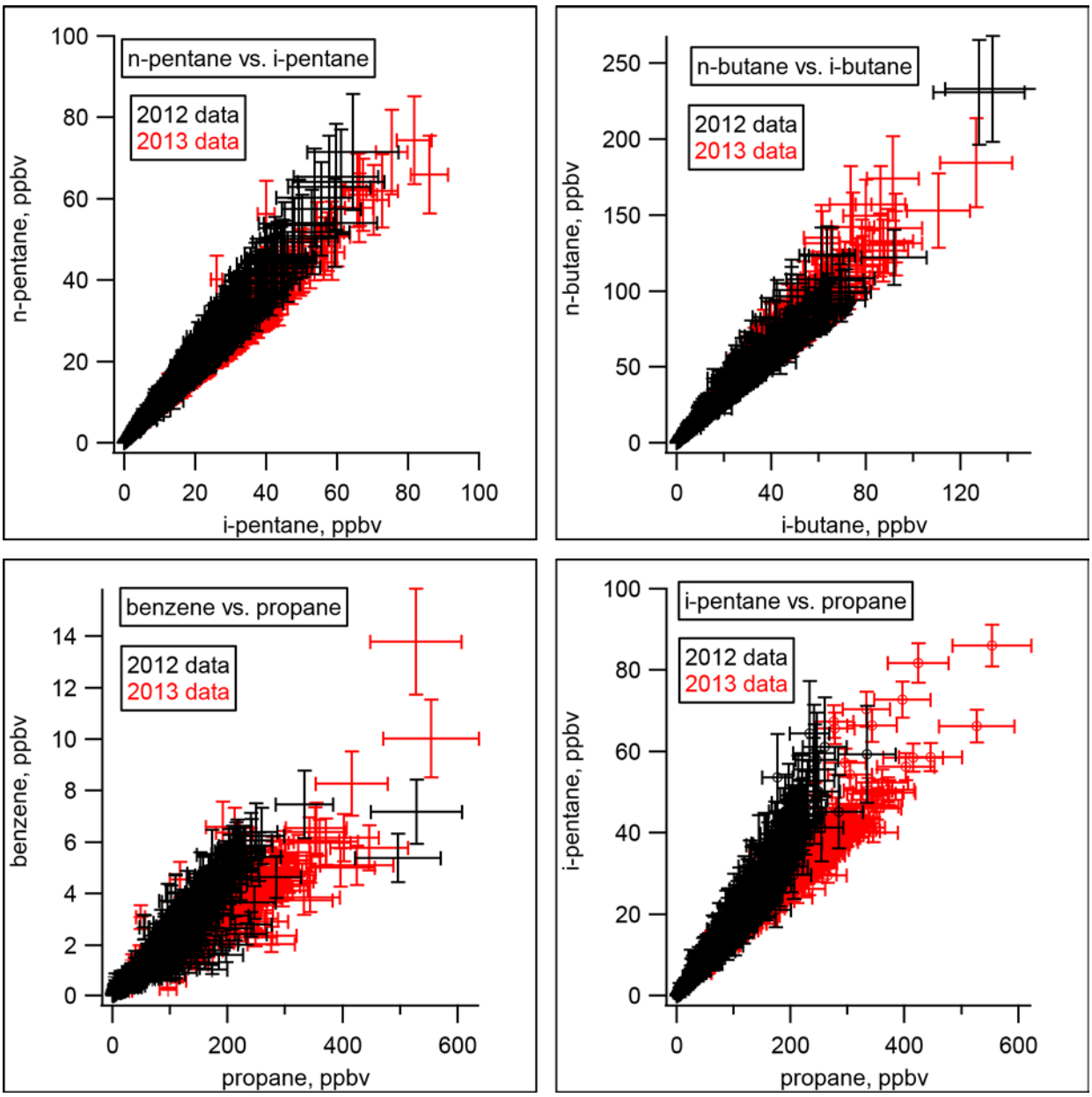

5-17. Ratios of iso-to n-butane, iso- to n-pentane, and benzene and i-butane to propane, for 2012 and 2013. The black symbols are for 2012 and the red symbols are for 2013, and the error bars are 1s of the measured data.

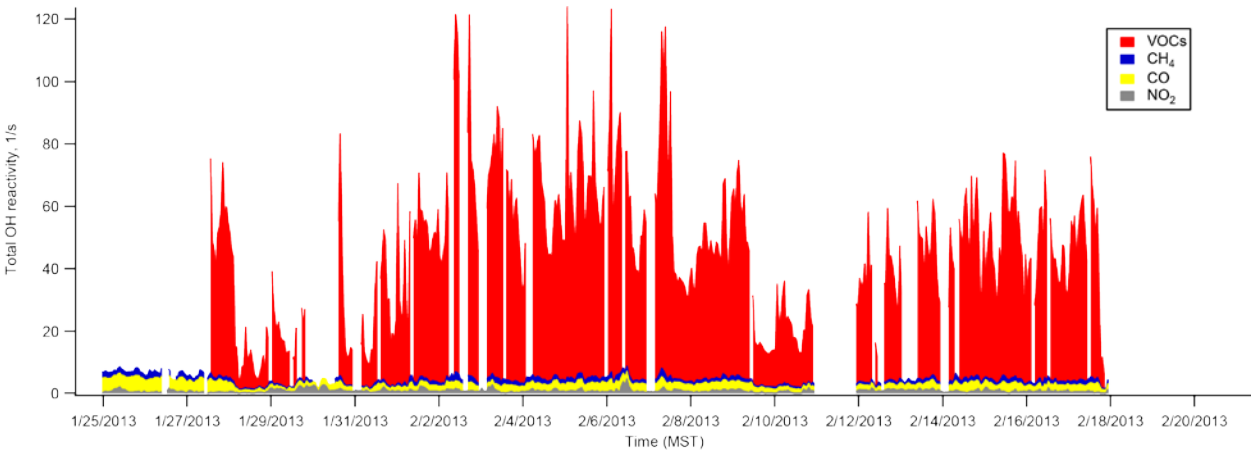

5-18. Time series of total OH reactivity of VOCs (red), methane (blue), carbon monoxide (yellow) and NO_2 (grey).

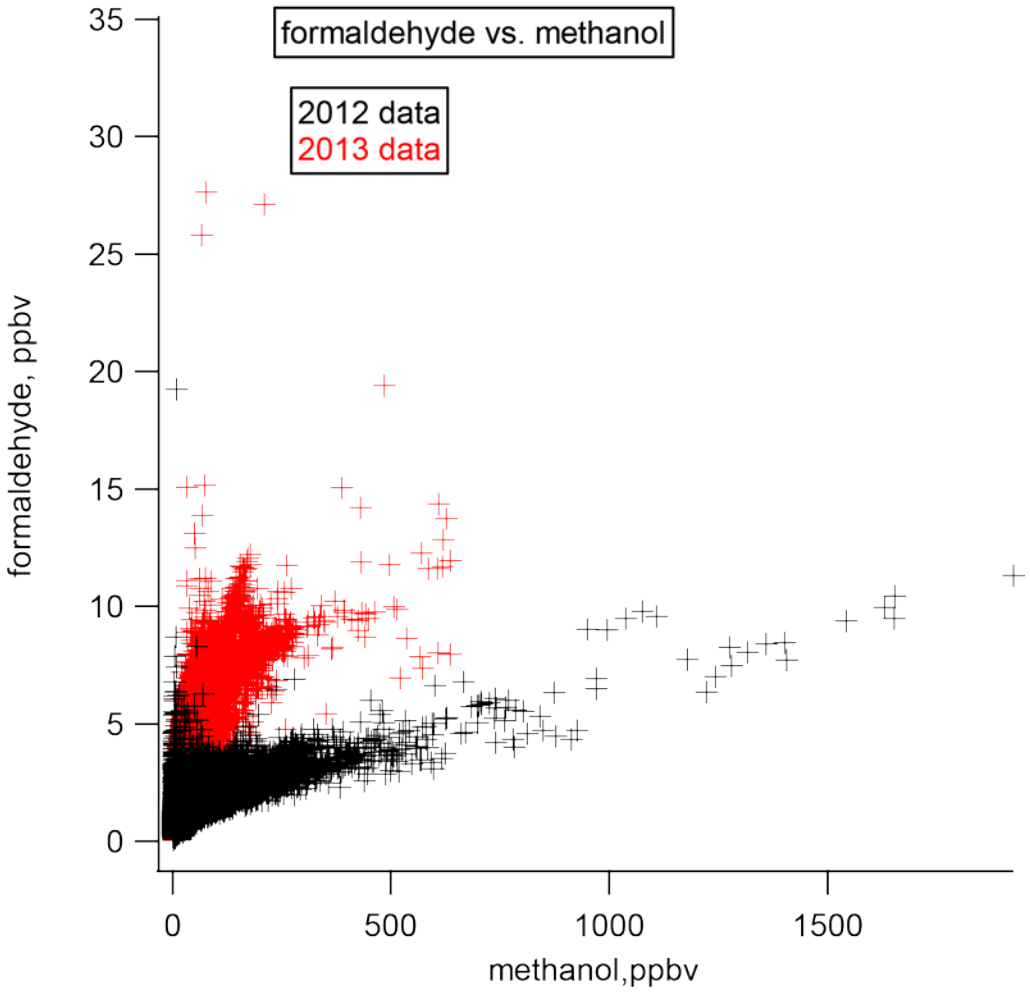

5-19. The relationship between formaldehyde and methanol for both 2012 (black) and 2013 (red).

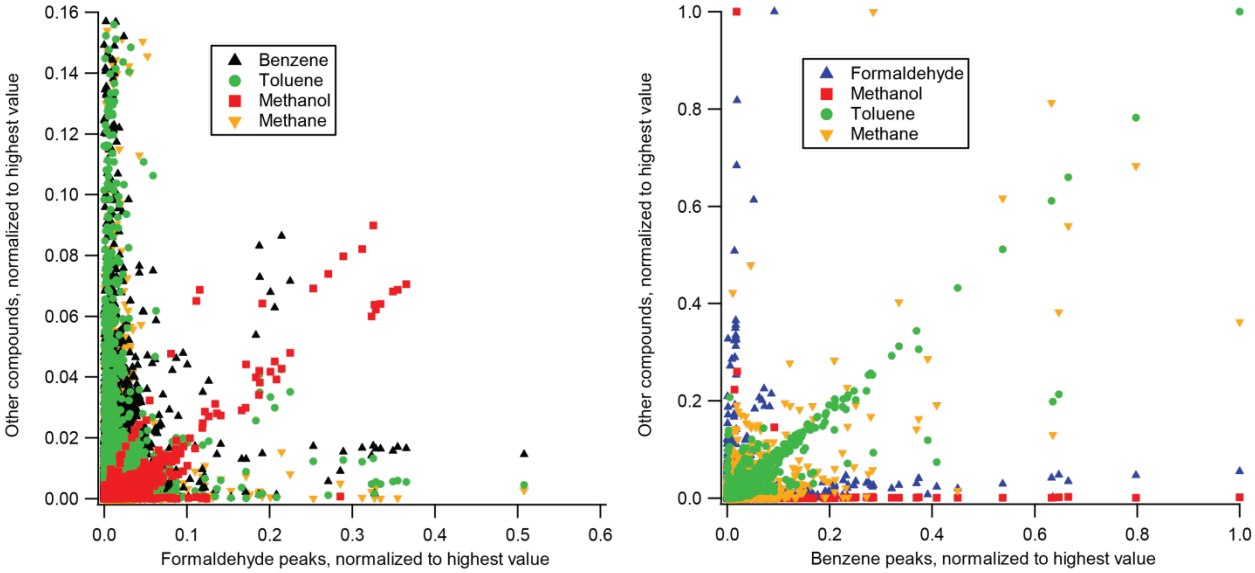

5-20. Correlations of marker compounds to (a) Formaldehyde, and (b) Benzene.

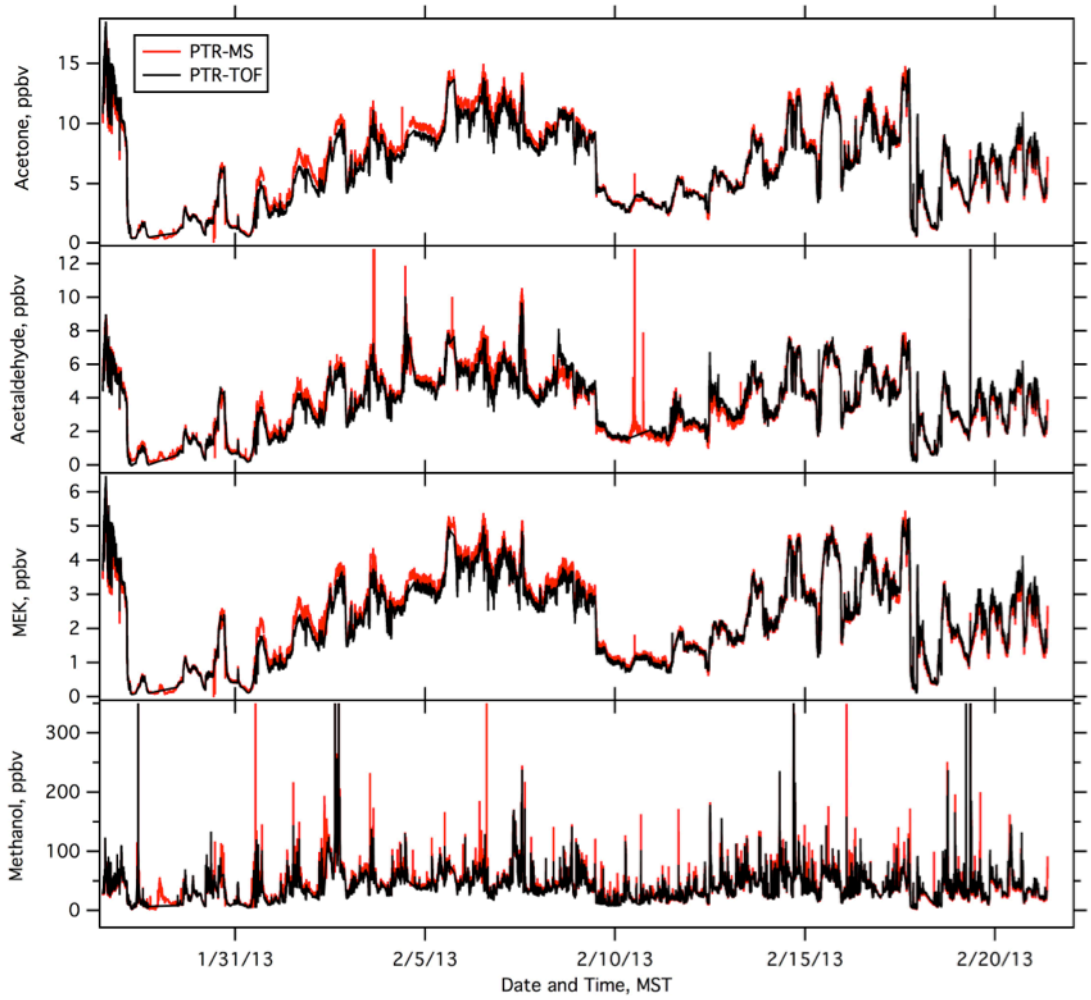

5-21. Time series of PTR-TOF-MS (black) and PTR-MS (red) VOC measurements made during the UBOS 2013 intensive period. The top three measurements (acetone, acetaldehyde, and methyl ethyl ketone (MEK)) are photochemically produced secondary pollutants formed throughout an ozone event. Methanol (bottom panel) is more indicative of a local emitted primary pollutant.

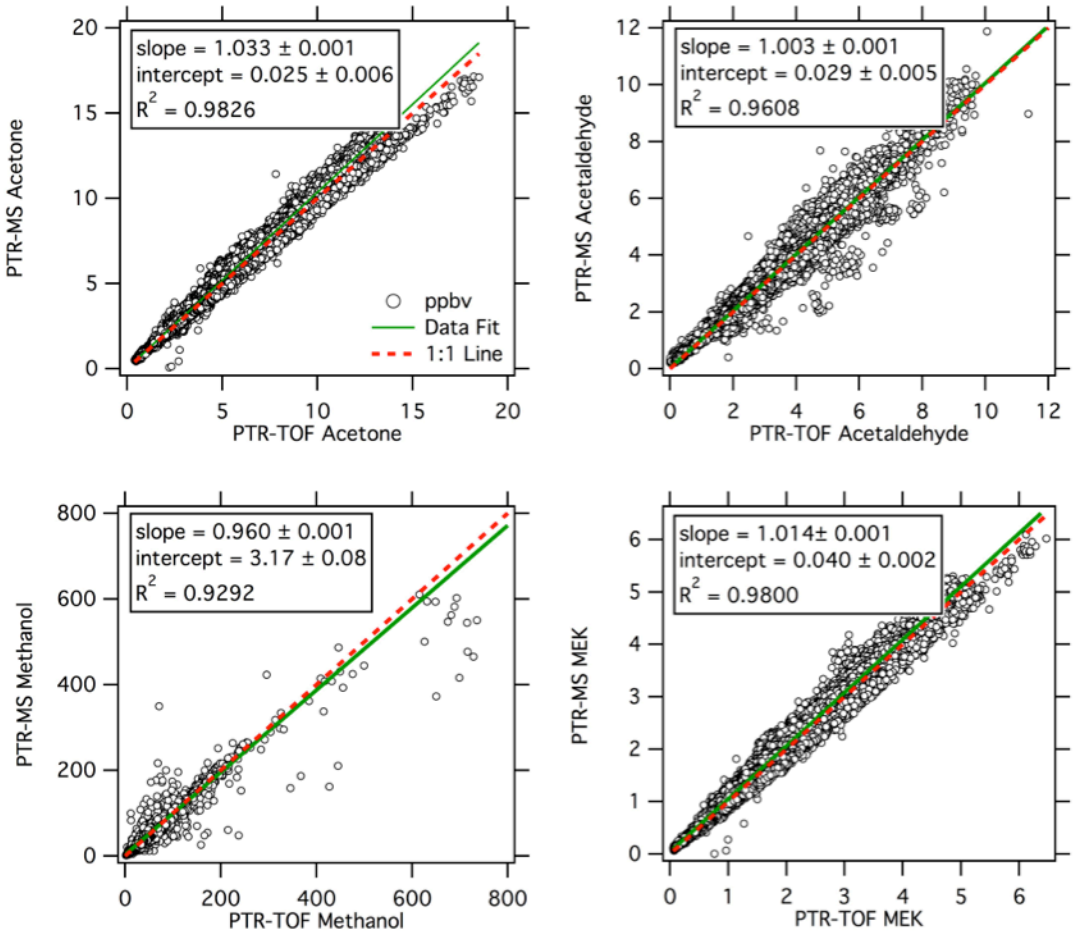

5-22. Linear regression plots of the PTR-MS and PTR-TOF VOC data collected during the UBOS 2013 intensive period and shown in Figure 1. These measurement techniques show agreement to within 5% for all of the VOC species quantified by both instruments.

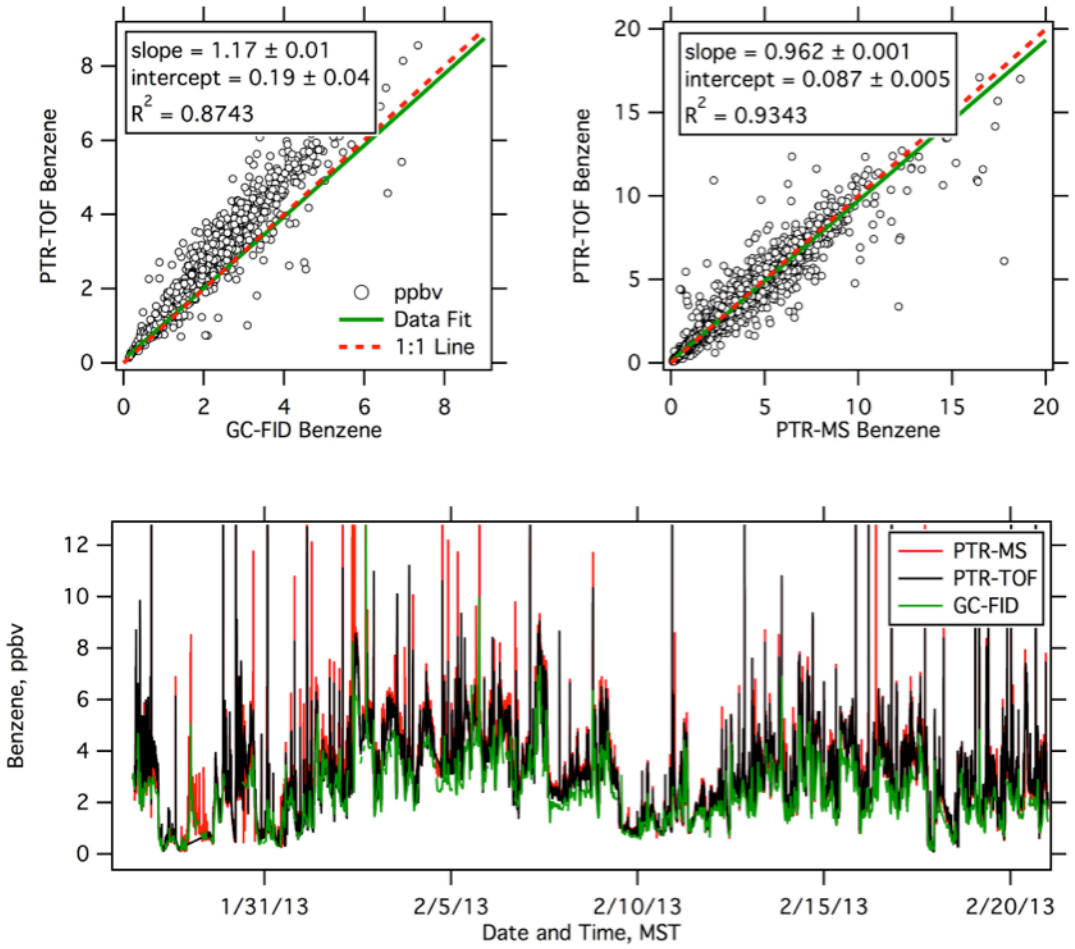

5-23. A comparison of PTR-TOF-MS, PTR-MS, and GC-FID measurement of benzene during the UBOS 2013 intensive period. The top two panels show linear regression fits of the PTR-TOF to GC-FID (left) and the PTR-TOF to PTR-MS (right) for the data shown in the time series provided in the bottom panel.

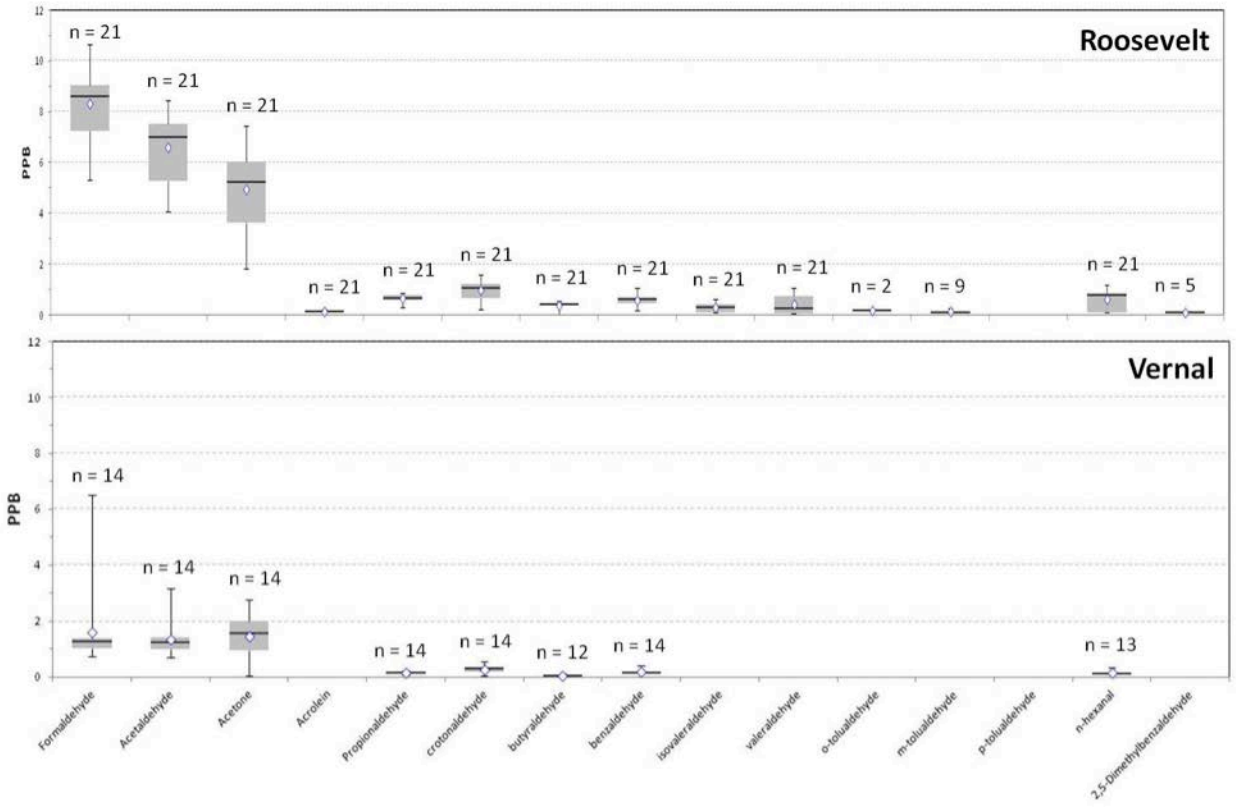

5-24. Box-whisker plots carbonyl compounds as measured at Roosevelt and Vernal (Feb. 13-25, 2013). The "n" indicates the number of times a particular compound was identified (21 total samples from Roosevelt, 14 total from Vernal).

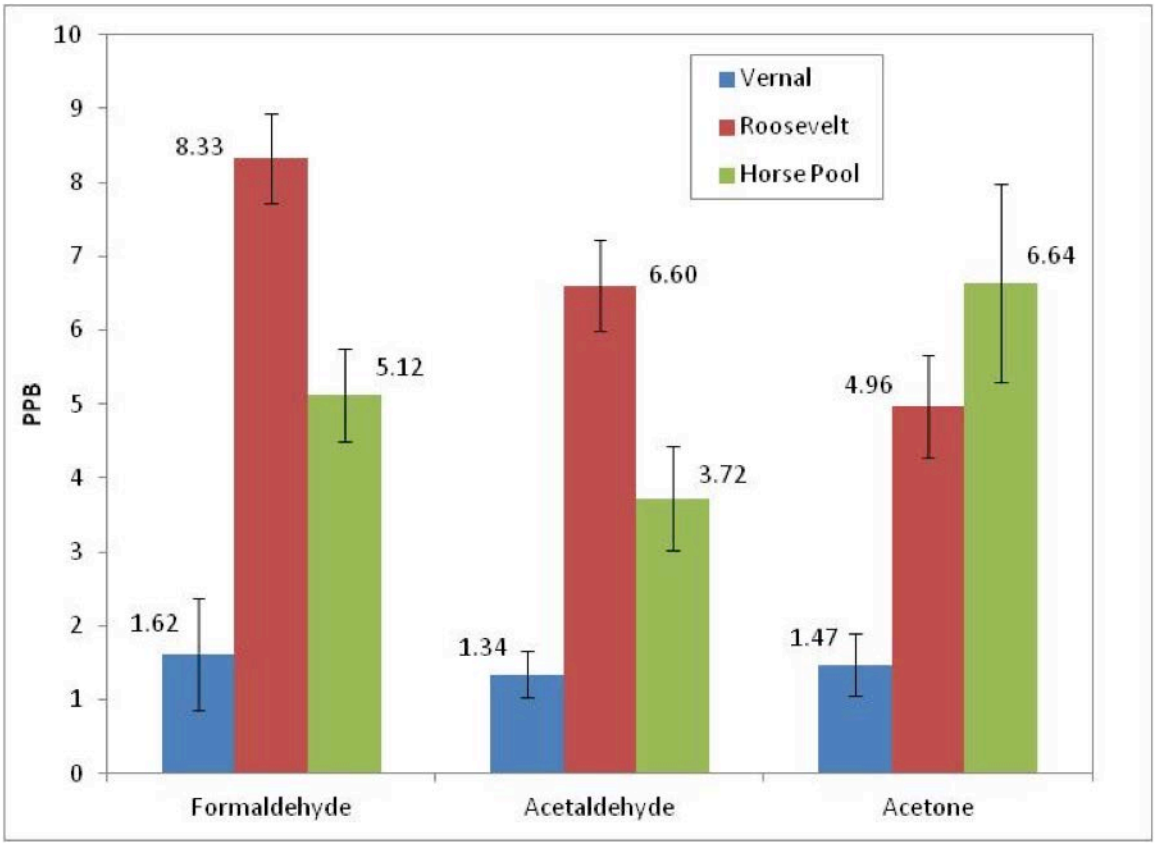

5-25. Comparison of average ambient formaldehyde, acetaldehyde, and acetone from Roosevelt, Vernal, Horse Pool-NOAA (Feb. 13-25, 2013). The error bars represent the 95% confidence intervals.

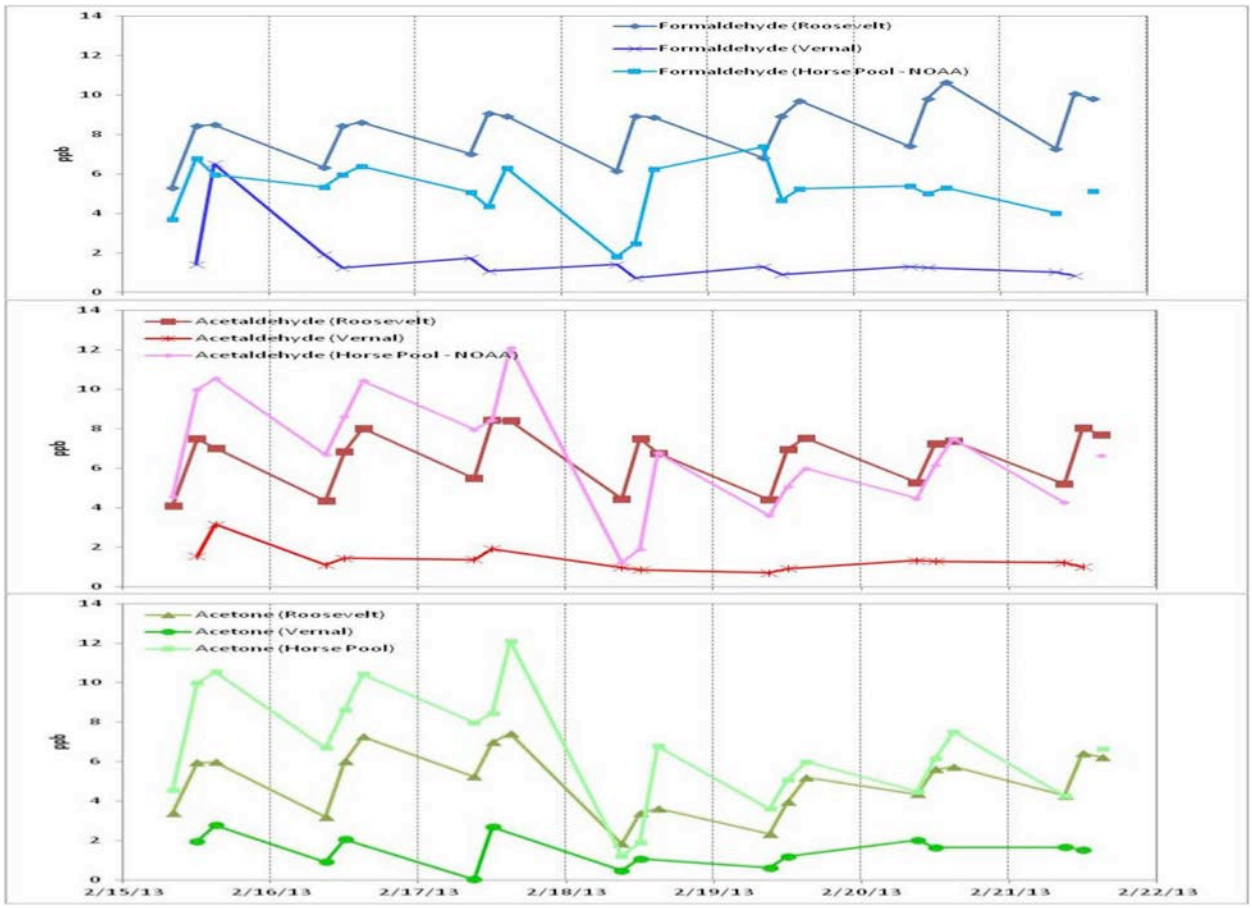

5-26. Diurnal, time series plots for formaldehyde, acetaldehyde, and acetone as measured at Roosevelt, Vernal and Horse Pool-NOAA (Feb. 13-25, 2013).

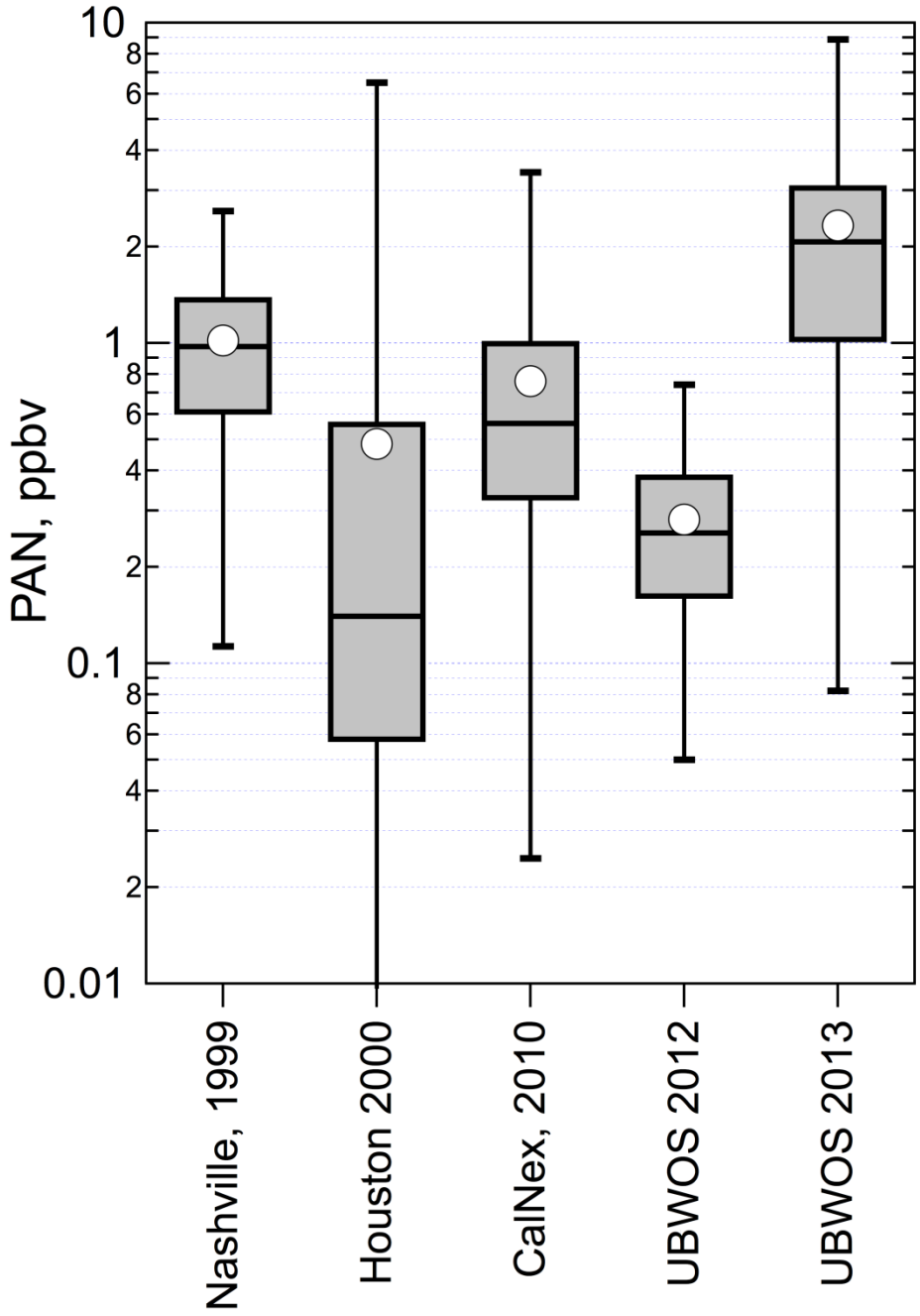

5-27. Distributions of PAN measurements for the two UBOS studies along with 3 other ground-based studies.

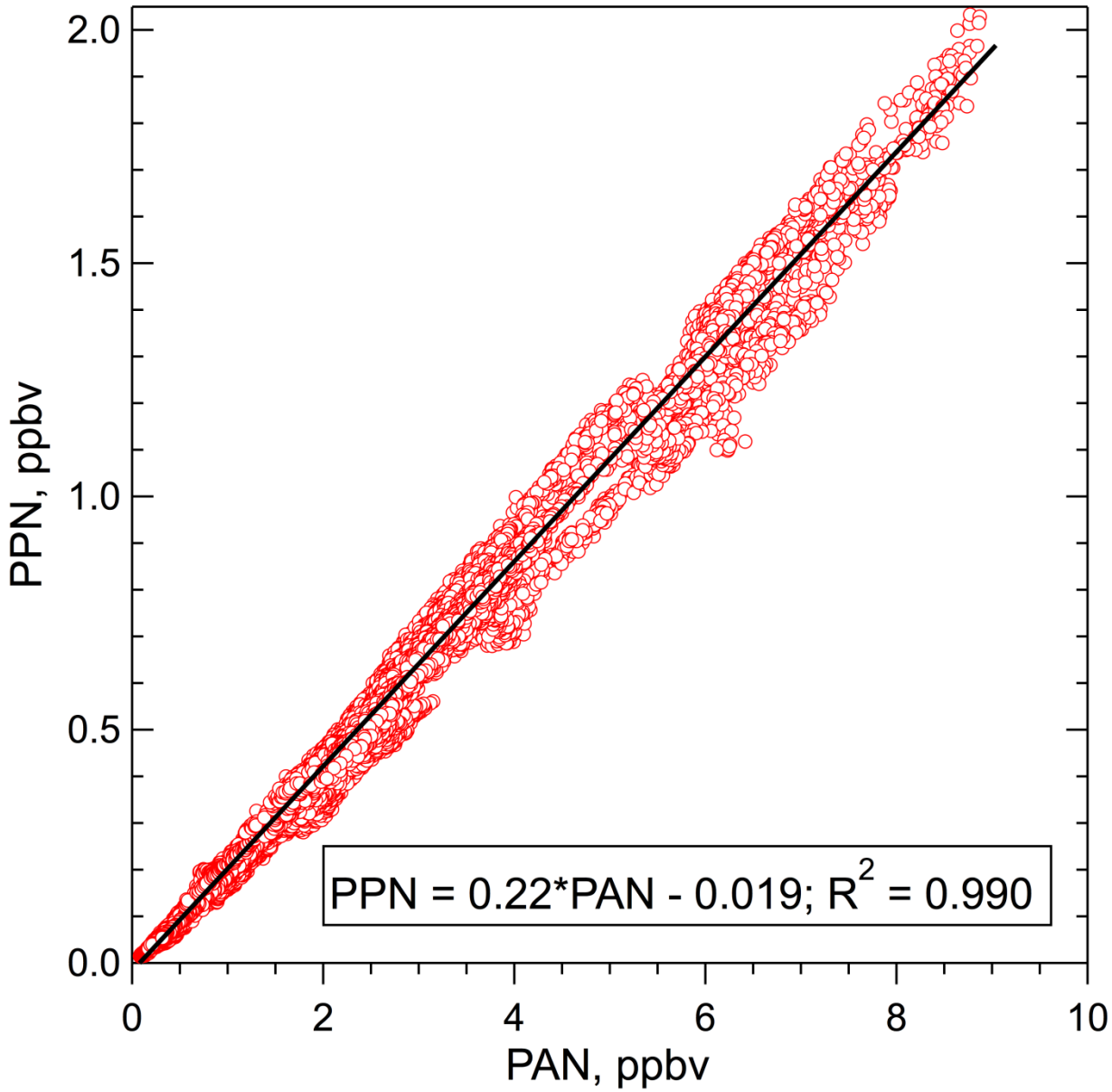

5-28. The correlation of PPN with PAN observed during the UBOS 2013 intensive.

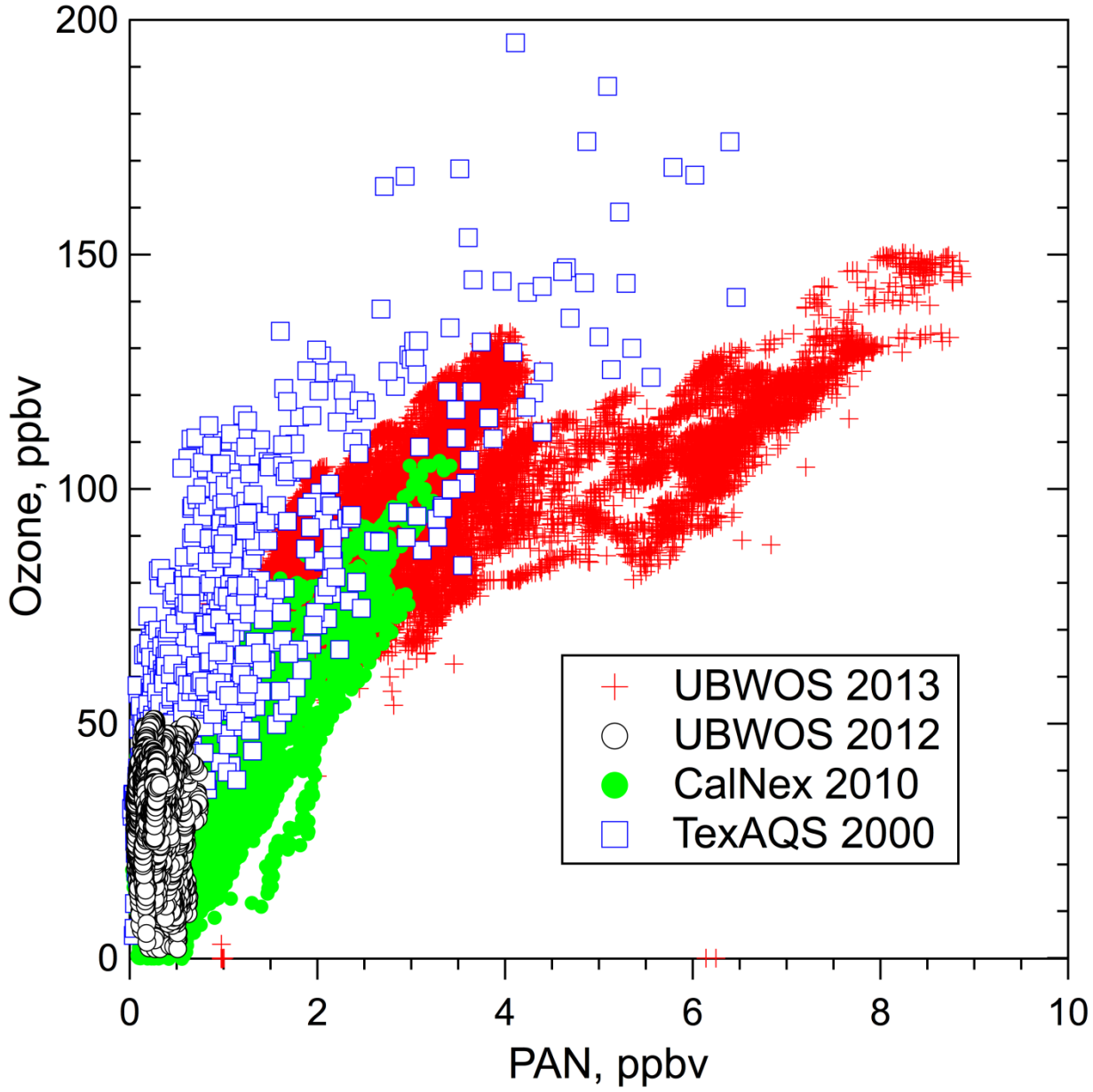

5-29. The correlation of O_3 with PAN for UBOS 2012 (open black circles), UBOS 2013 (red crosses), TexAQS 2000 (open blue squares) and CalNex 2010 (solid green circles).

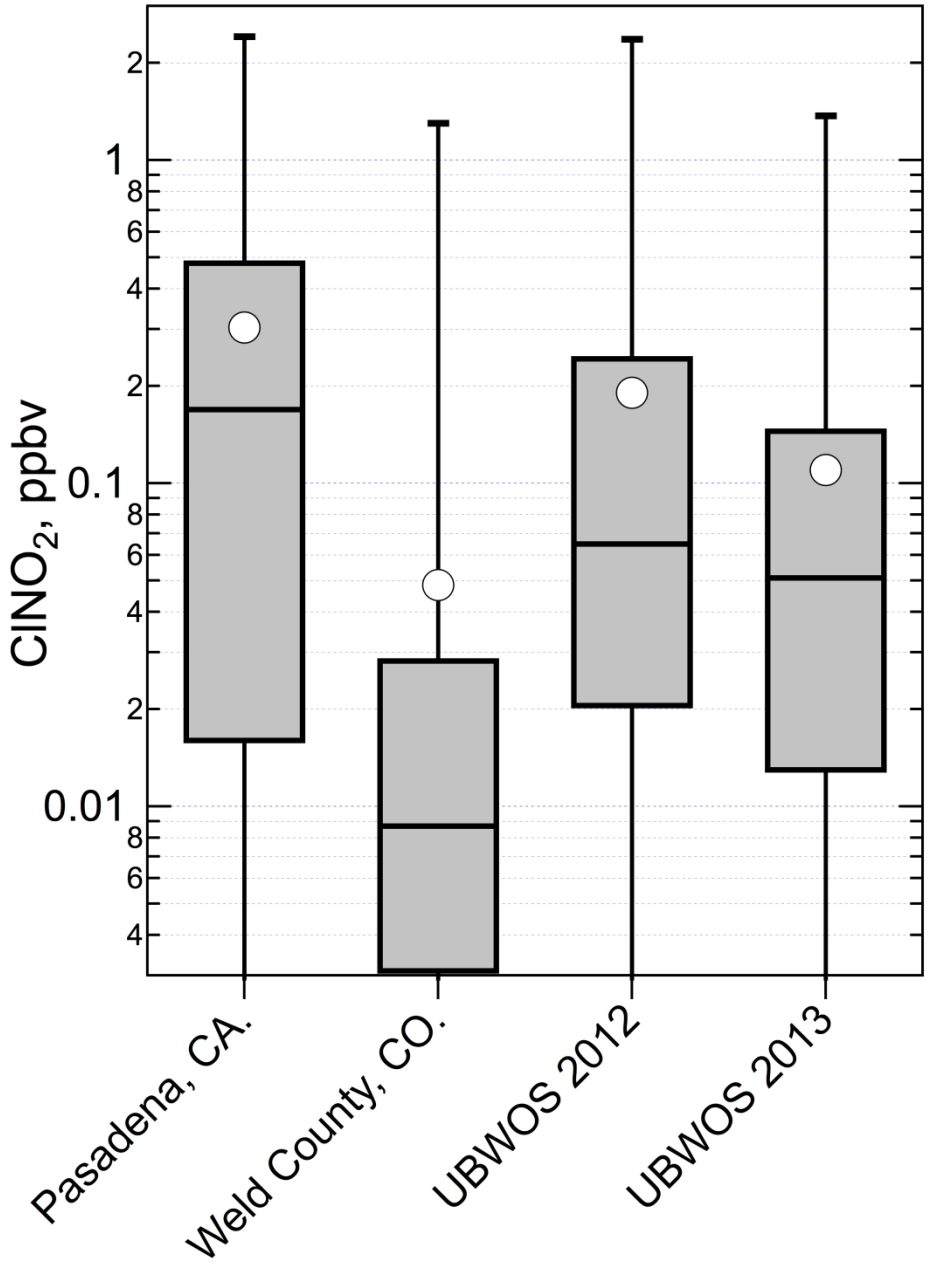

5-30. Distributions of $ClNO_2$ measurements for the two UBOS studies along with 2 other ground-based studies.

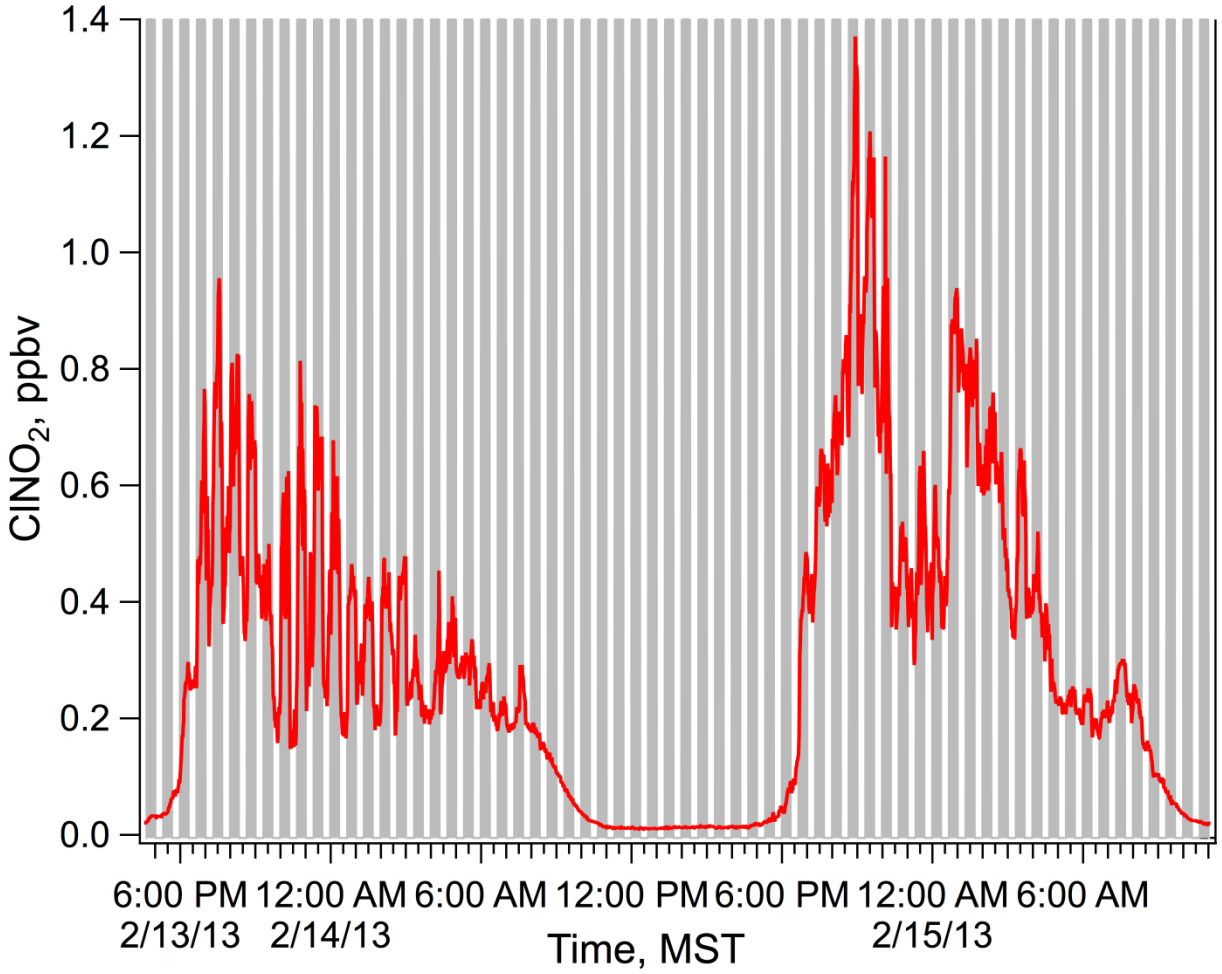

5-31. Gradients in $ClNO_2$ mixing ratio during the inlet profiling experiment. The grey bands denote when the inlet was at the upper height (7.25 m).

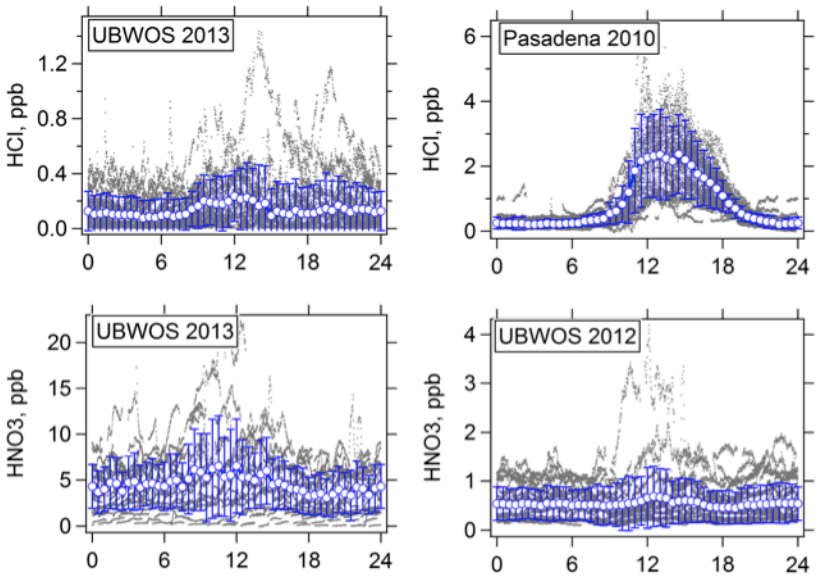

5-32. Diurnal variations of HCl and HNO_3 in 2012 and 2013 at Horse Pool.

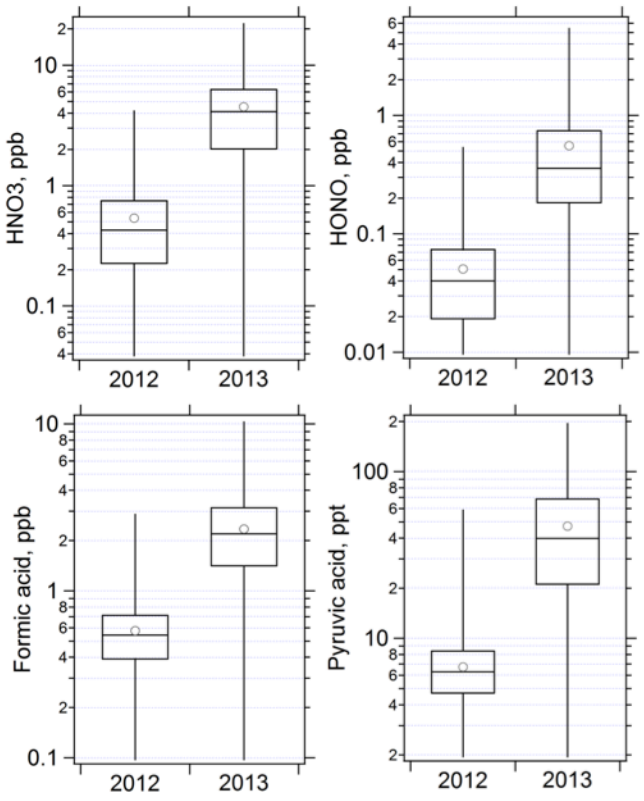

5-33. Comparison of the measured concentration of HNO_3, HONO, formic acid and Pyruvic+butyric acid between 2012 and 2013 at Horse Pool.

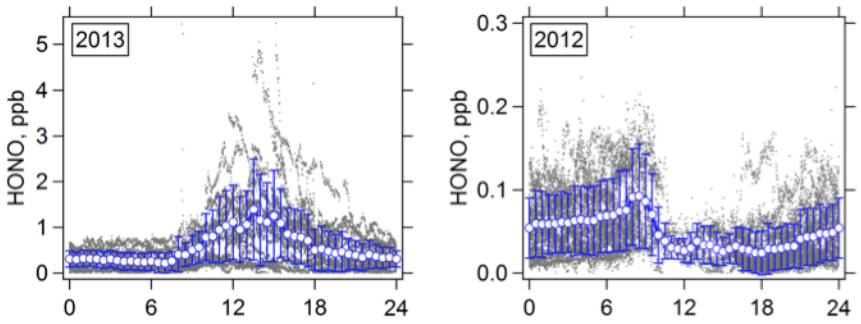

5-34. Diurnal variations of HONO in 2012 and 2013 at Horse Pool.

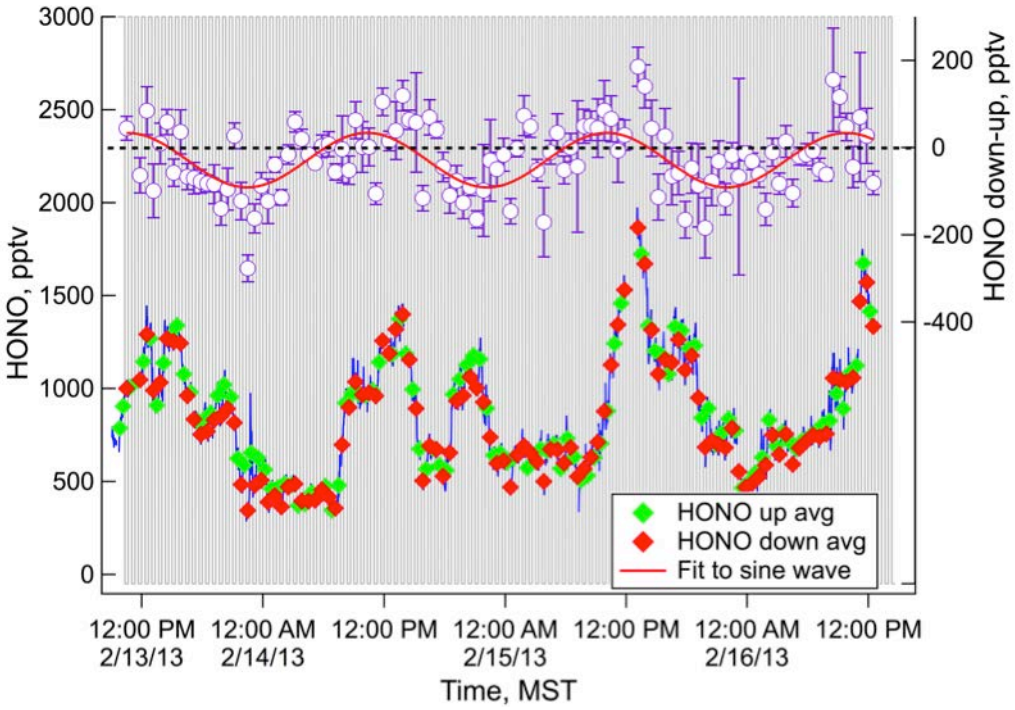

5-35. Measured HONO during the period when the inlet height was switching between 1m and 7.25 m (grey line). The blue line is the 1 minute average HONO, and the green and red points are the 20 minute averaged HONO measured while the inlet was up, or down, respectively. The difference between the HONO measured with the inlet down and the HONO measured with the inlet up interpolated between measurements is shown in the open purple circles with one standard deviation of the down measurement average shown as error bars.

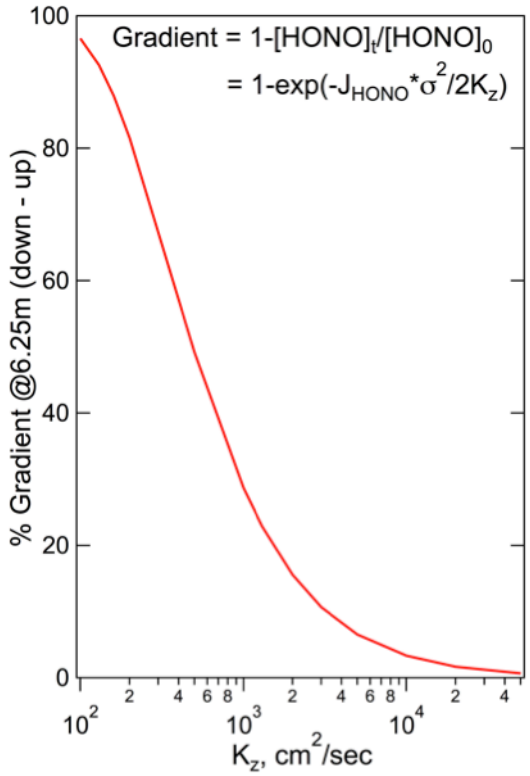

5-36. The percent gradient for a ΔH of 6.25m, calculated as a function of eddy diffusivity, K_z, based on an average photolysis rate of 0.0016 sec^{-1}.

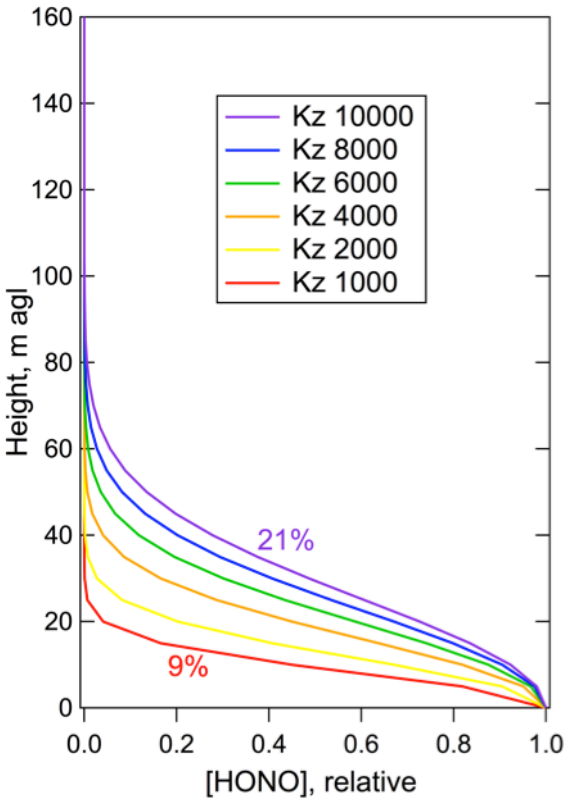

5-37. Concentration profiles predicted for the range of K_z that corresponded to gradients of ~0 to 15% as shown in Figure 5-36.

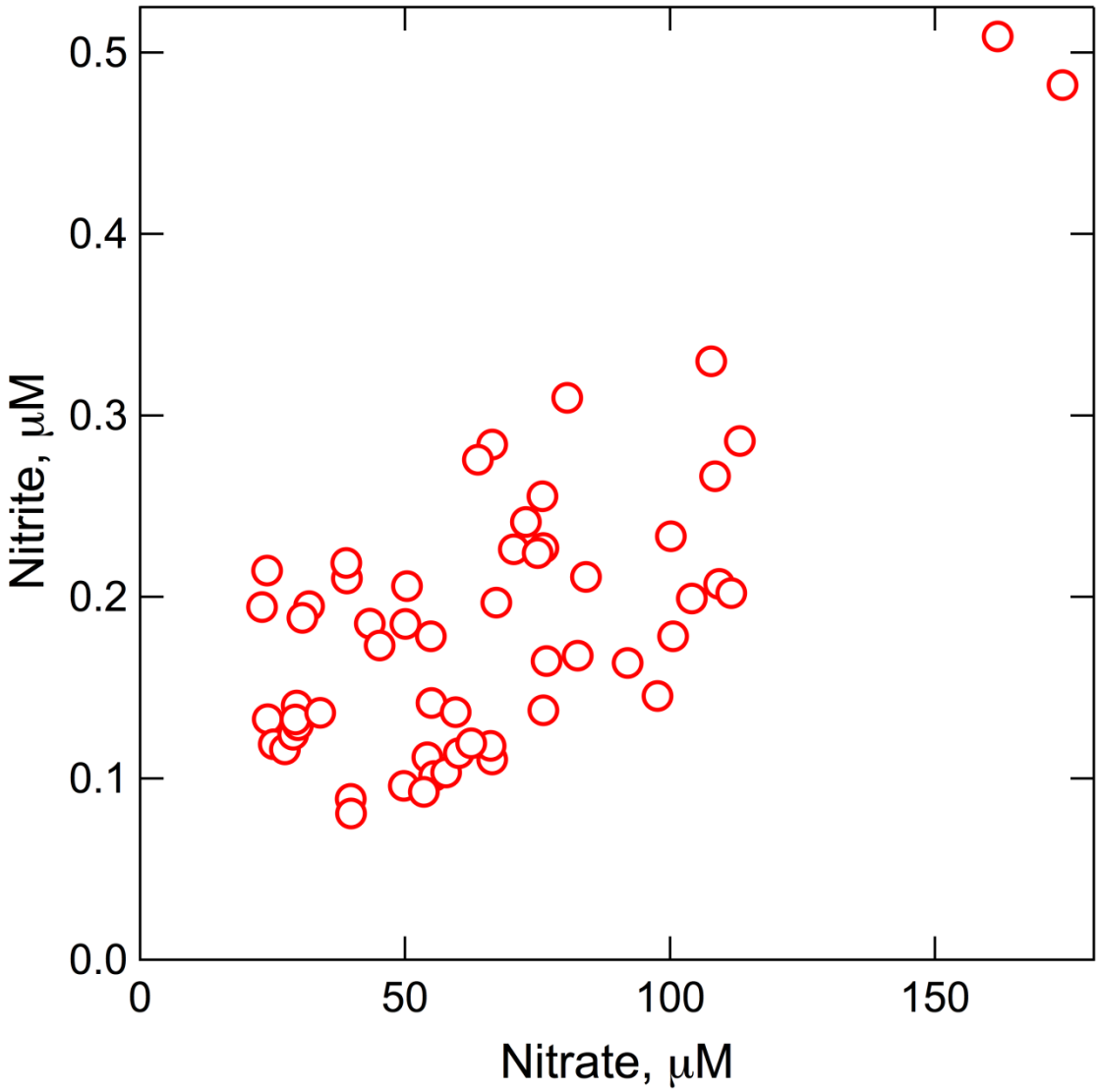

5-38. The concentration of nitrite in the top layer of snow, versus the concentration of nitrate.

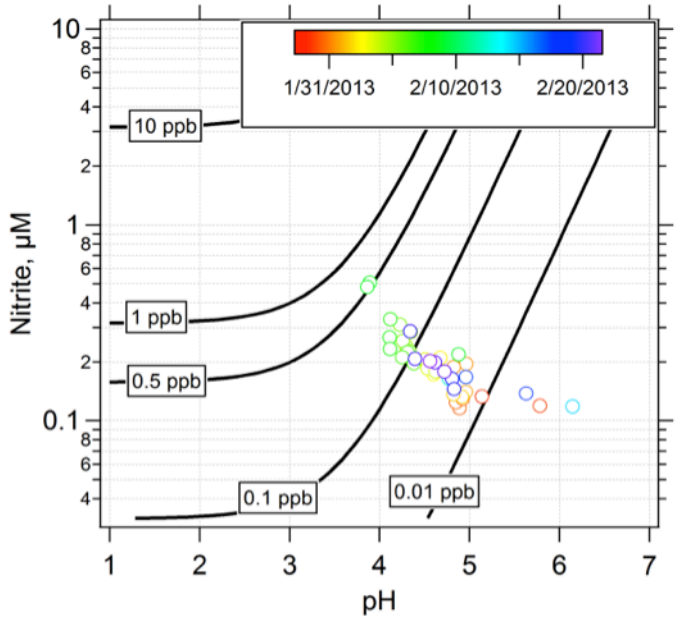

5-39. The dependency of equilibrium gas phase HONO (HONO*) with pH value and nitrite concentration in the snow. The contour lines are calculated at 268 K (assuming the presence of a liquid layer), which is a regular value for ambient temperature at noon time at Horse Pool site. The circles in the graph represent the measured snow results near Horse Pool site. The circles are color-coded with measurement time.

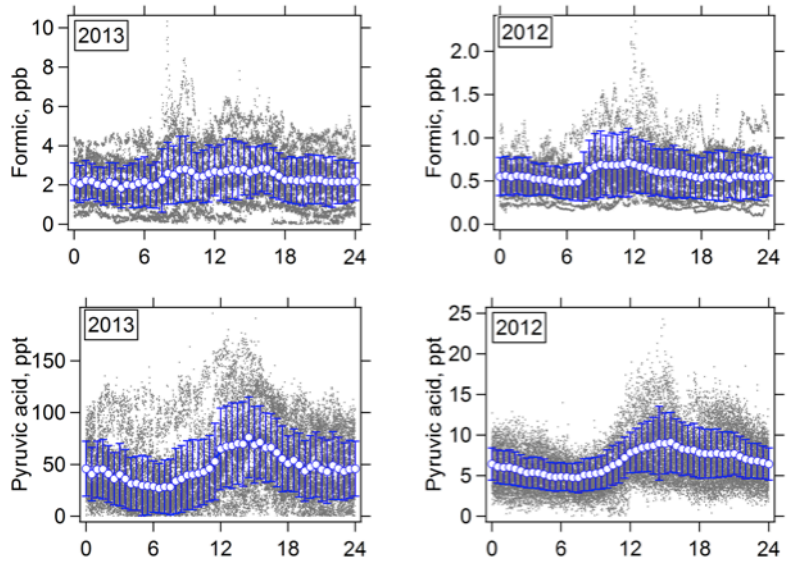

5-40. Diurnal variations of formic acid and pyruvic+butyric acid in 2012 and 2013 at Horse Pool.

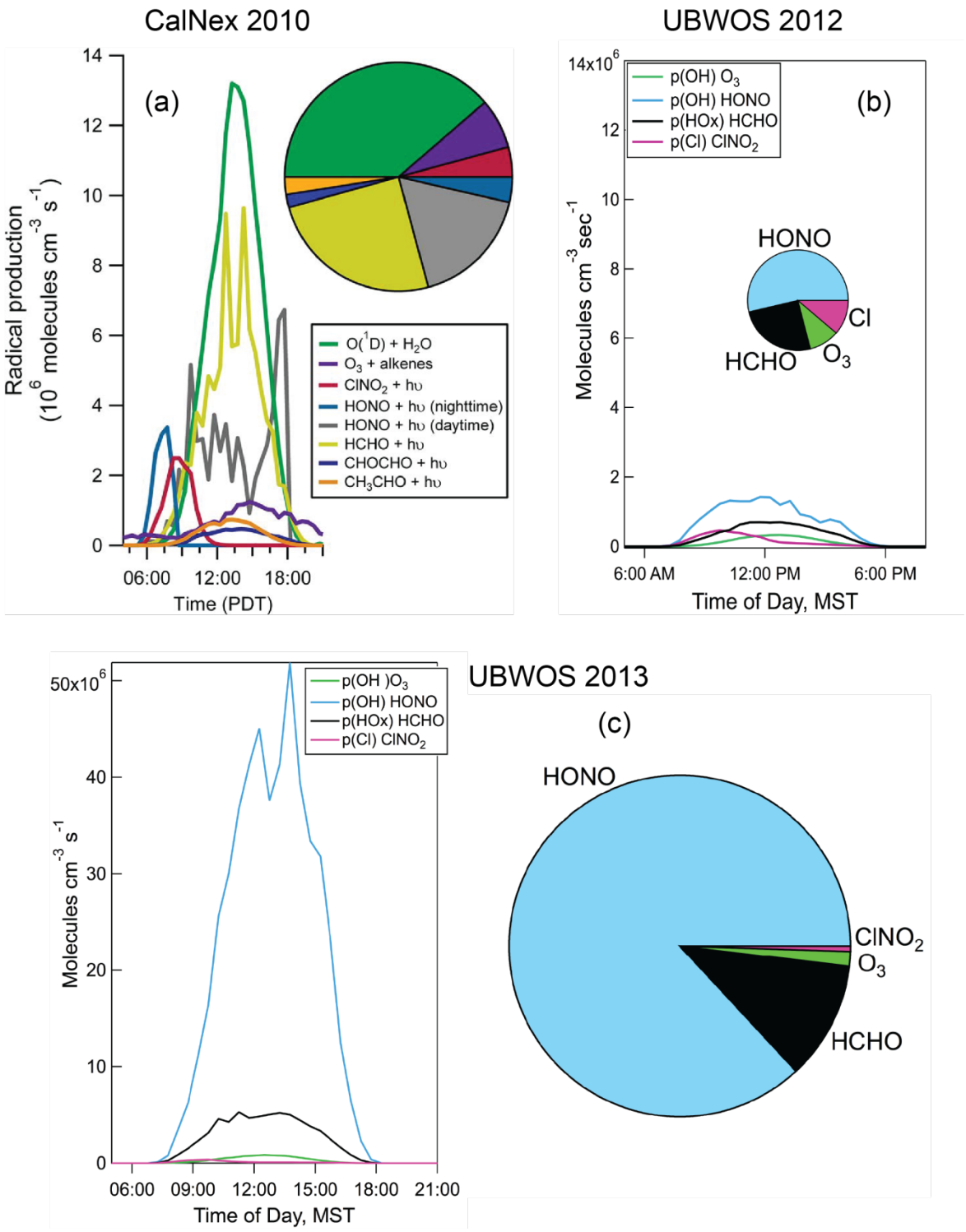

5-41. Summaries of the radical sources found during (a) CalNex2010, (b) UBOS 2012, and (c) UBOS 2013. Note that the CalNex and UBOS 2012 results are on the same scale, and the areas of the pie charts are scaled to the total of the radical sources.

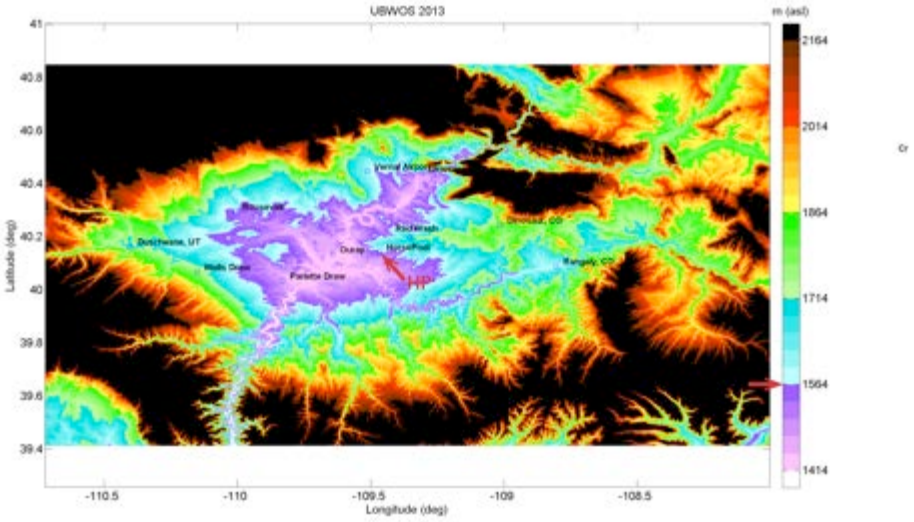

5-42. Terrain contour map of Uinta Basin region with color scale adjusted to emphasize the nature of the Basin topography. Color scale is adjusted so that elevation of the Horse Pool site (HP: red arrow on map) falls between purple and blue colors (red arrow on color bar).

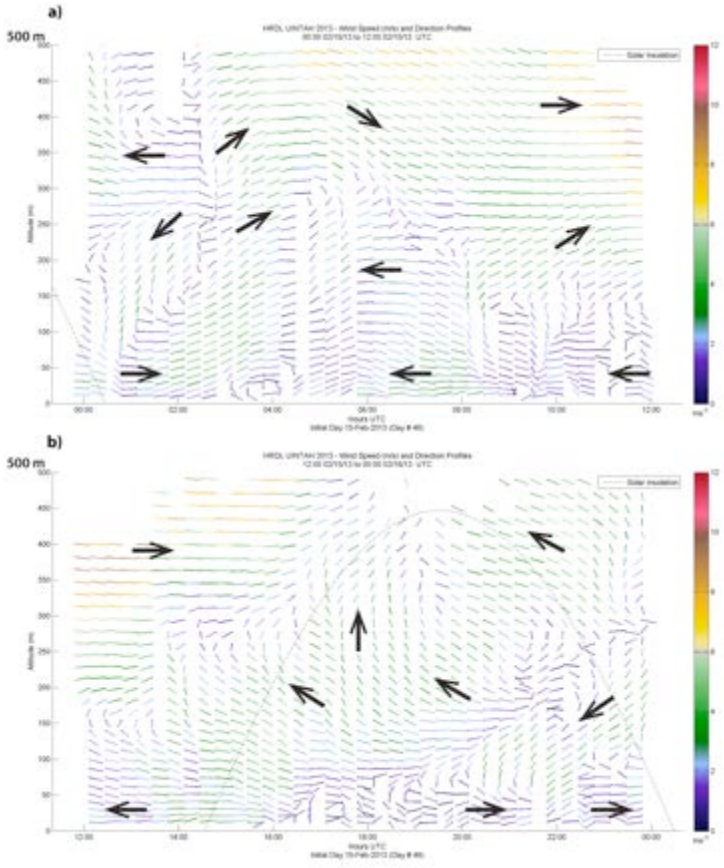

5-43. Time-height cross sections as in Figure 5-2, showing a 24-hr period on 15 Feb 2013. Dark arrows indicate predominant wind direction.

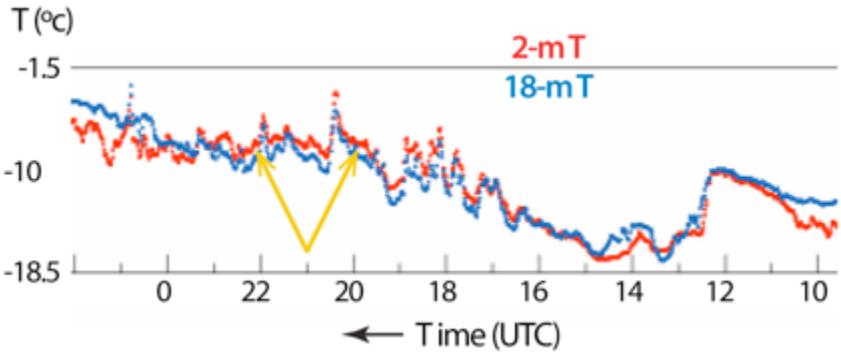

5-44. Temperature traces at the Horse Pool site at 2 and 18 m above ground on 30 January, showing temperatures 1-2° warmer at the lower level during the day (gold arrows).

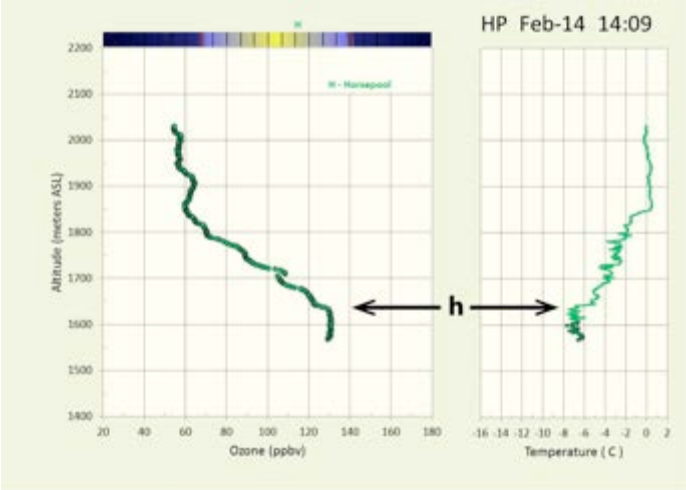

5-45. Tethered-balloon profiles of O_3 (left) and potential temperature θ (right) at the Horse Pool site at 1409 MST (2109 UTC) on 14 February.

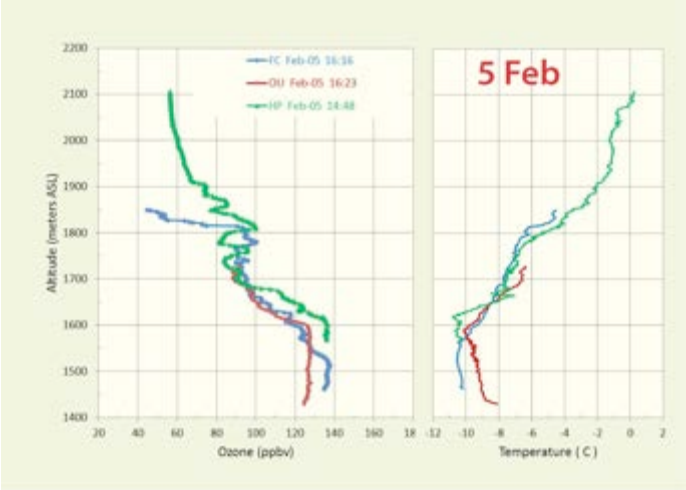

5-46. Tethered-balloon profiles of O_3 (left) and potential temperature θ (right), as in Figure 5-45, at the Horse Pool site (HP: green curves), the Fantasy Canyon site (FC: blue curves), and at the Ouray site (OU: red curves) at approximately 1620 MST (2320 UTC) on 5 February.

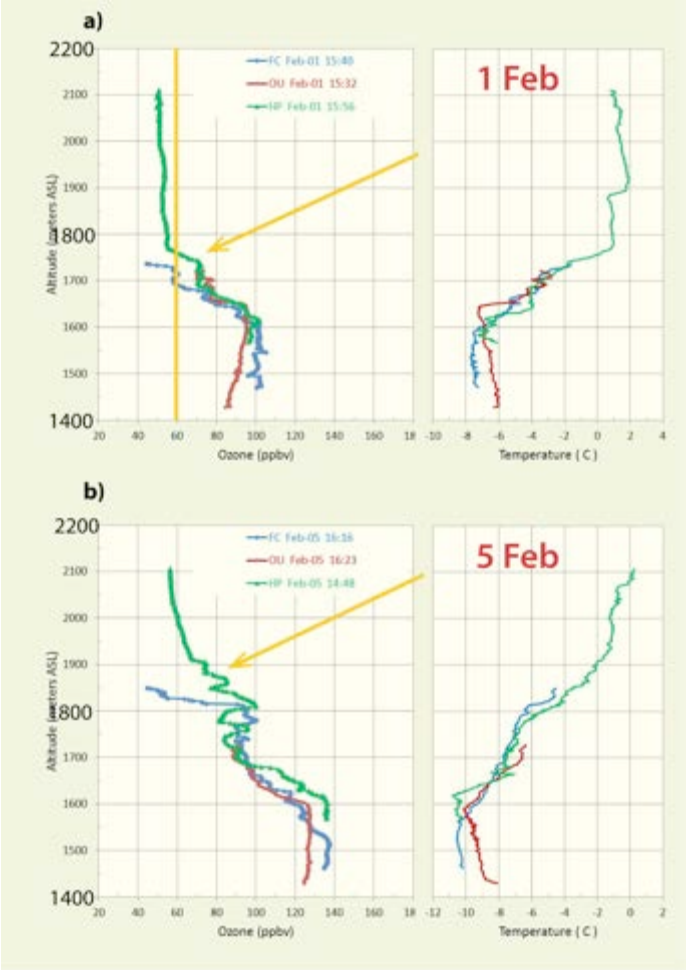

5-47. Tethered-balloon profiles of O_3 (left) and potential temperature θ (right), as in Figure 5-45, at the Horse Pool site (HP: green curves), the Fantasy Canyon site (FC: blue curves), and at the Ouray site (OU: red curves) at approximately 1545 MST on 1 February (top panels) and1620 MST on 5 February (bottom curves). Vertical exchange processes move O_3 higher into inversion layer as episode proceeds (gold arrows), but much variation is seen within days and from day to day.

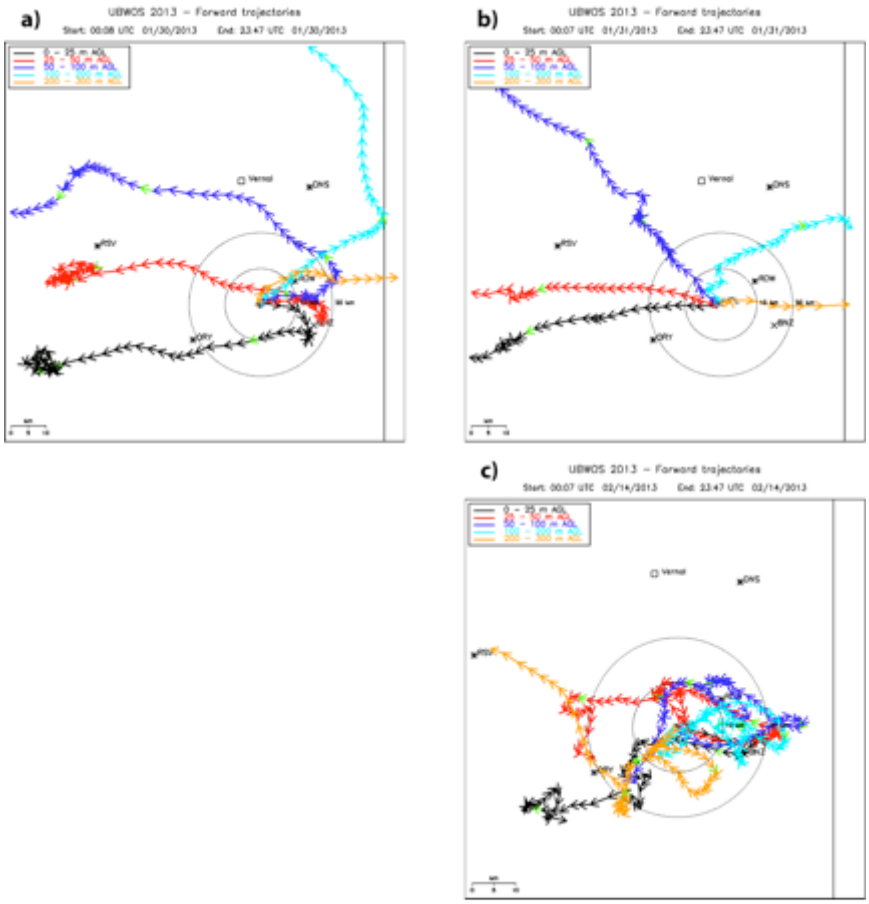

5-48. 24-hr, single-station trajectories starting at the Horse Pool site at ~0000UTC (1700 MST) for 5 atmospheric levels between 0 and 300 m AGL for 30 January (top left), 31 January (top right), and 14 February (bottom).

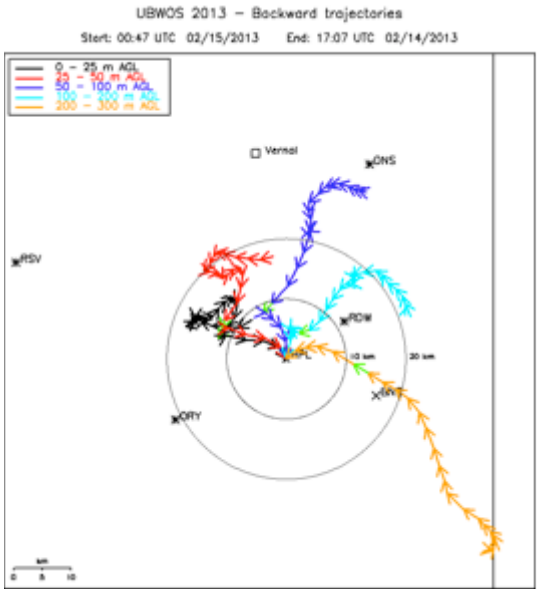

5-49. Backward trajectories starting at the Horse Pool site at 0047 UTC on 15 February (1747 MST, 14 February), when a marked O_3 deficit was observed over the site. The highest trajectory (gold) passed directly over the Bonanza Power Plant power plant (BNZ), whereas the lower profiles did not.

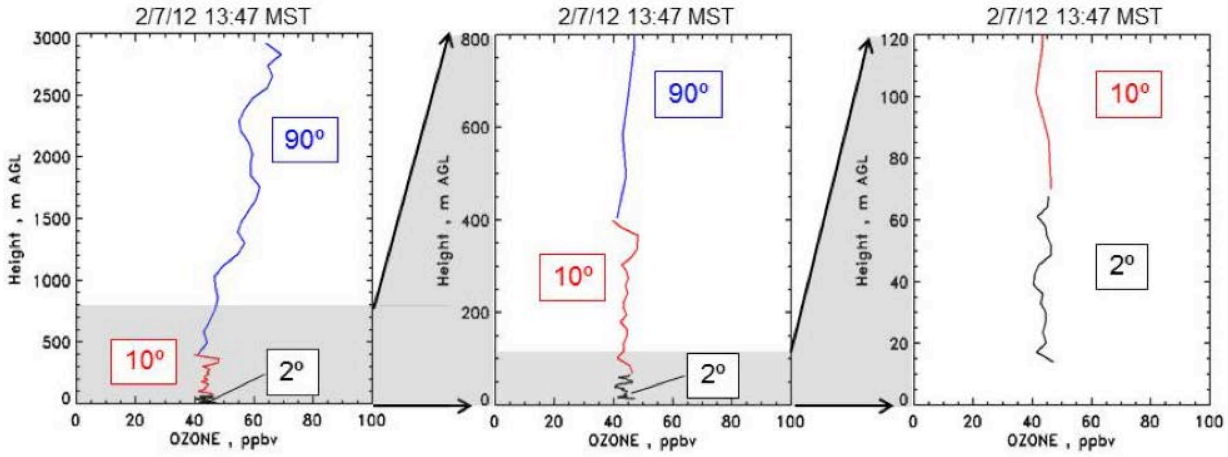

5-50. Lidar ozone profiles observed at elevations angles of 2°, 10°, and 90°, projected vertically and blended together. The entire profile is shown on the lefthand plot and the middle and righthand plots show successive expansions of the profile. The data were taken on 7 February 2012 during the first UBOS study.

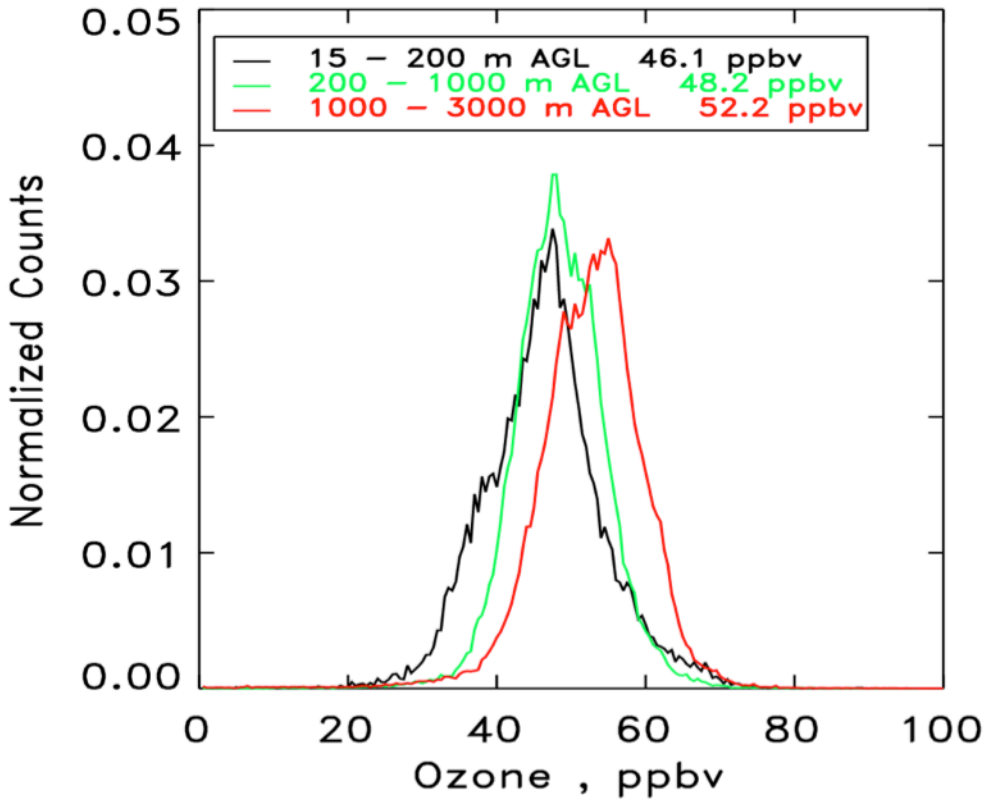

5-51. Normalized PDFs of all UBOS 2012 ozone lidar measurements for three altitude ranges. Mean ozone values for the different altitude bins are indicated in the legend.

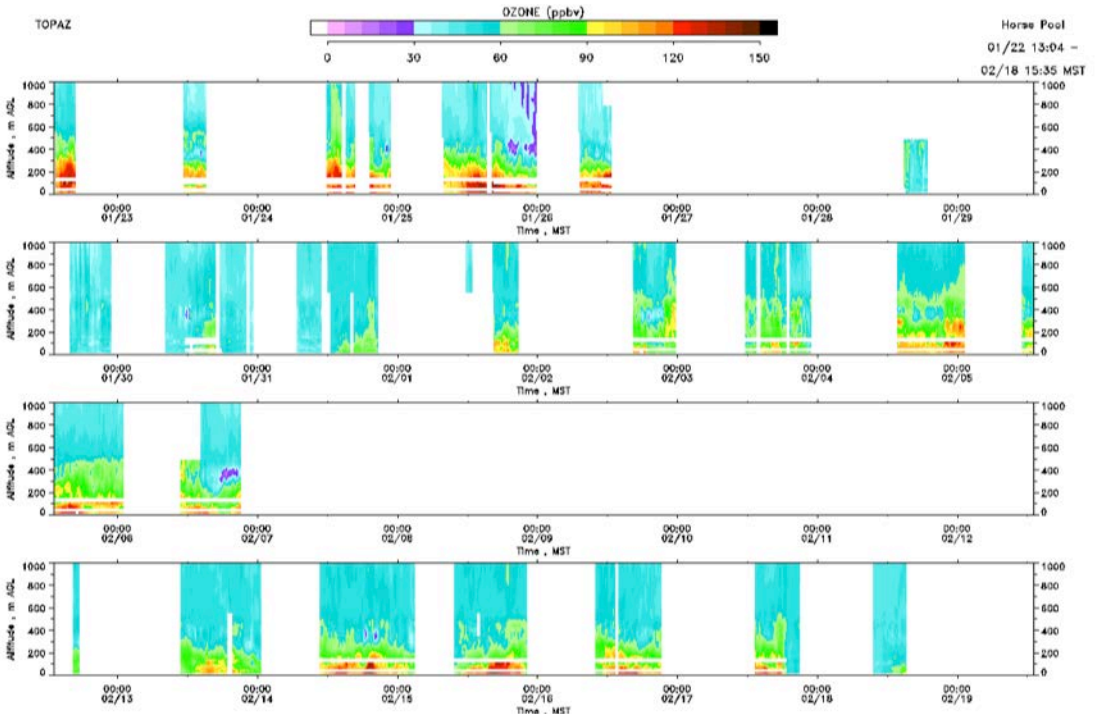

5.52. Overview of the TOPAZ ozone profile measurement from the UBOS 2013 study. Ozone profiles are only shown up to 1000 m AGL to better depict the ozone structure in the lowest few hundred meters.

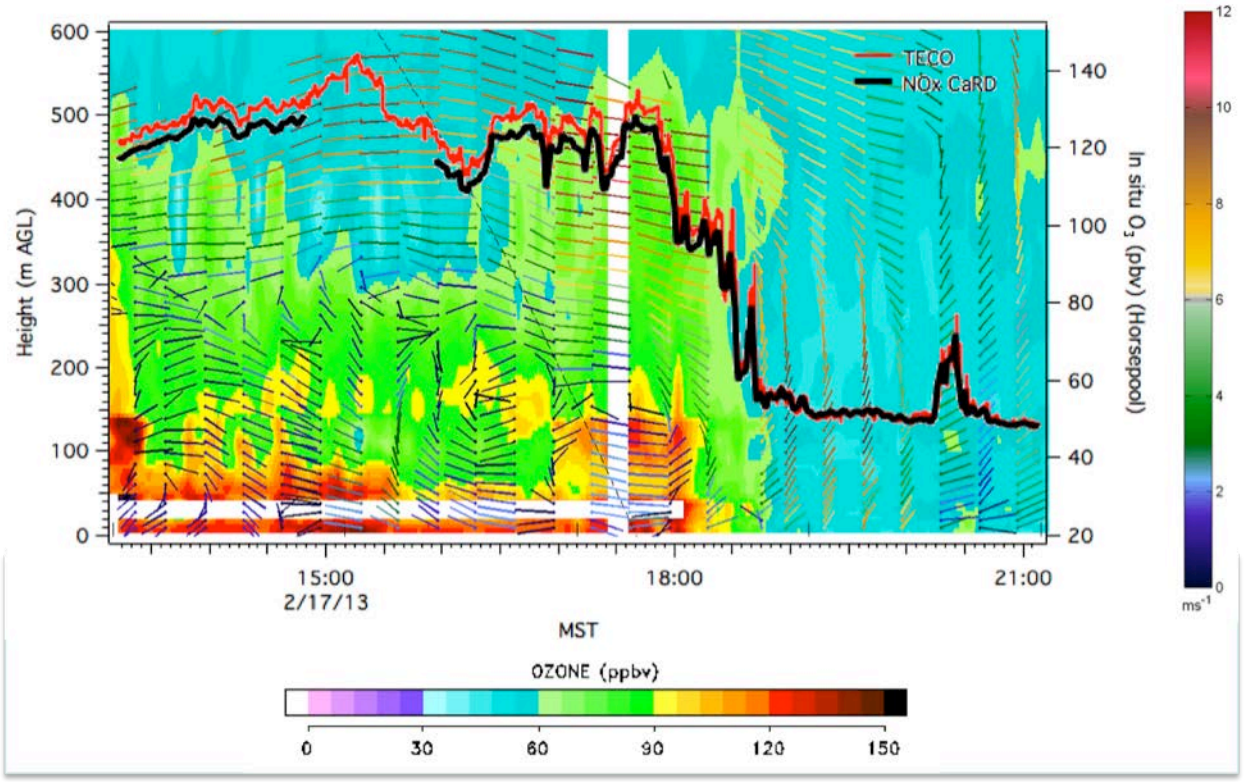

5-53. TOPAZ ozone time-height cross section up to 600 m AGL on 17 February 2013. HRDL lidar horizontal wind measurements (shown as colored wind barbs) and ozone observations from two in situ sensors (thick black and red lines) are overlaid. The dashed line indicates solar irradiance (arbitrary scale).

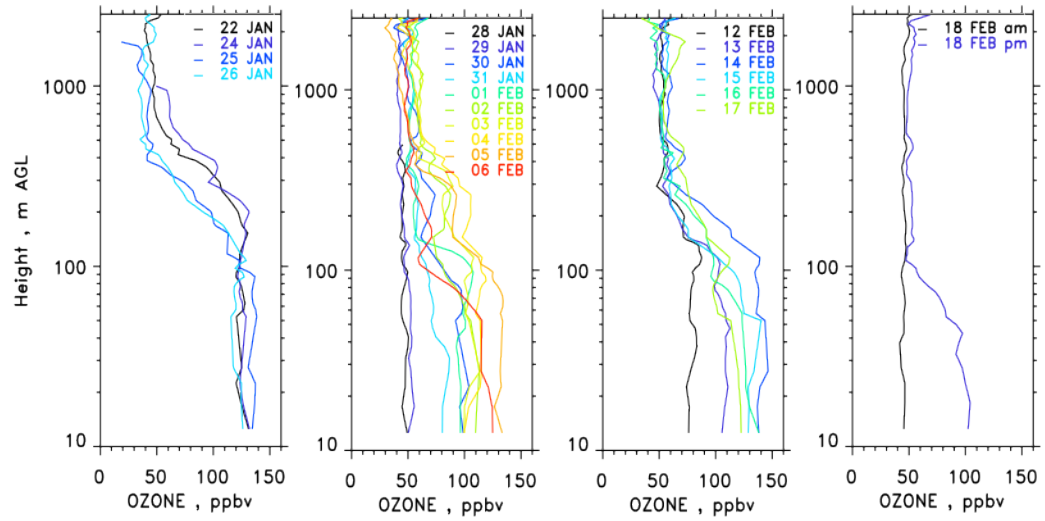

5-54. 15-min ozone profiles grouped by ozone episode for every day of TOPAZ observations. The profiles were measured when BL ozone peaked in the afternoons.

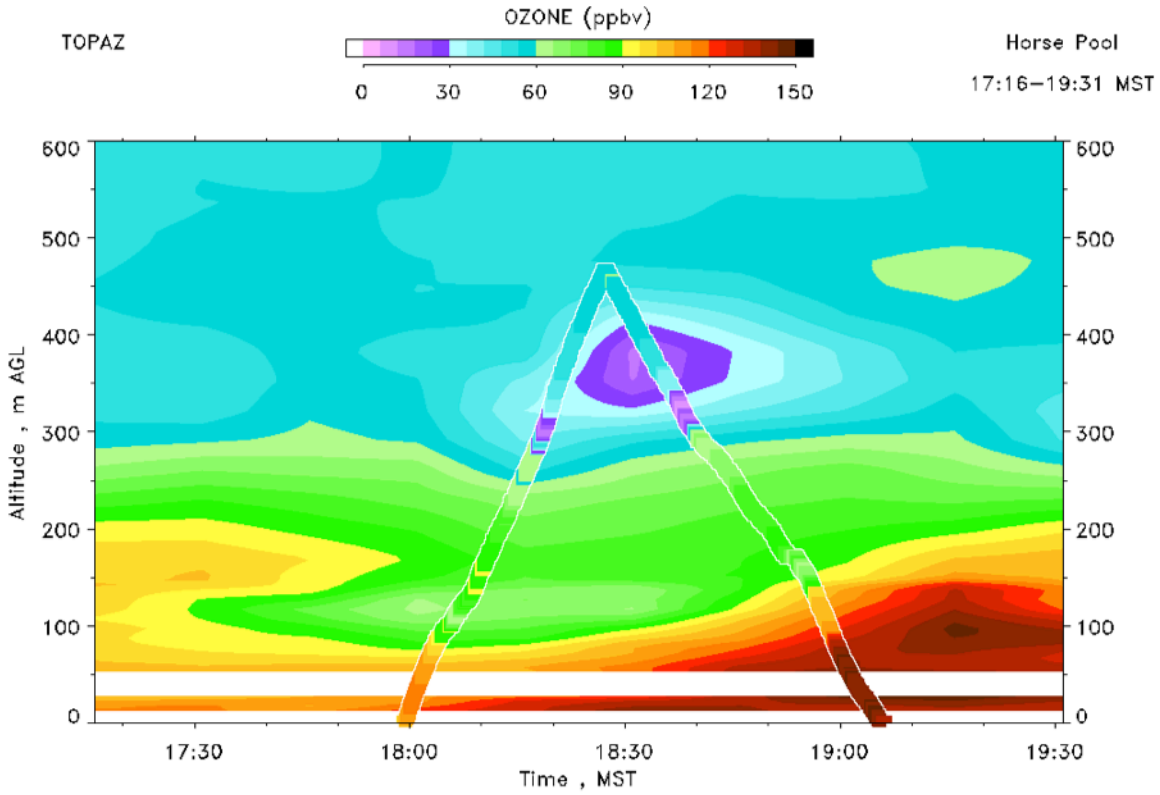

5-55. TOPAZ time-height cross section of ozone from near the surface to 600 m AGL for 17:16 – 19:31 MST on 14 February 2013. The colored line shaped like an inverted "V" represents the ozone measurements from the collocated tether sonde.

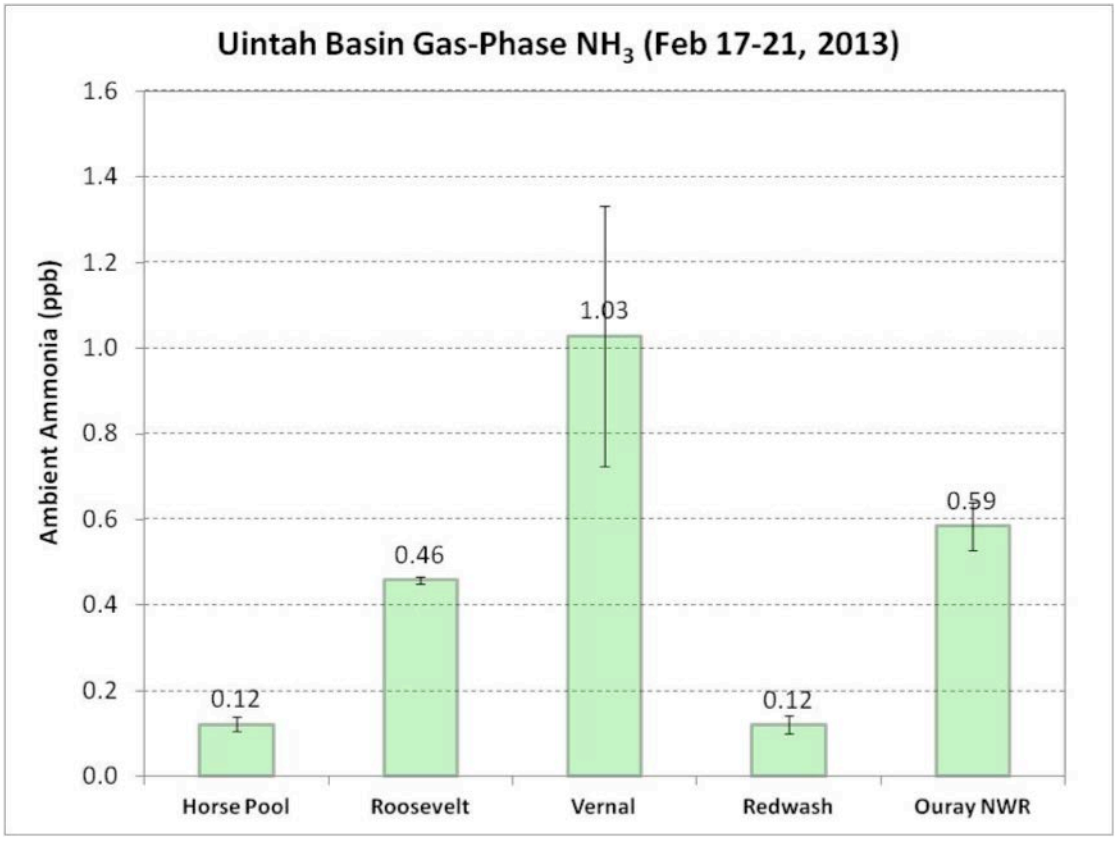

5-56. Ambient ammonia concentrations at various sites within the Uinta Basin. The error bars represent the range of duplicate measurements at each site.

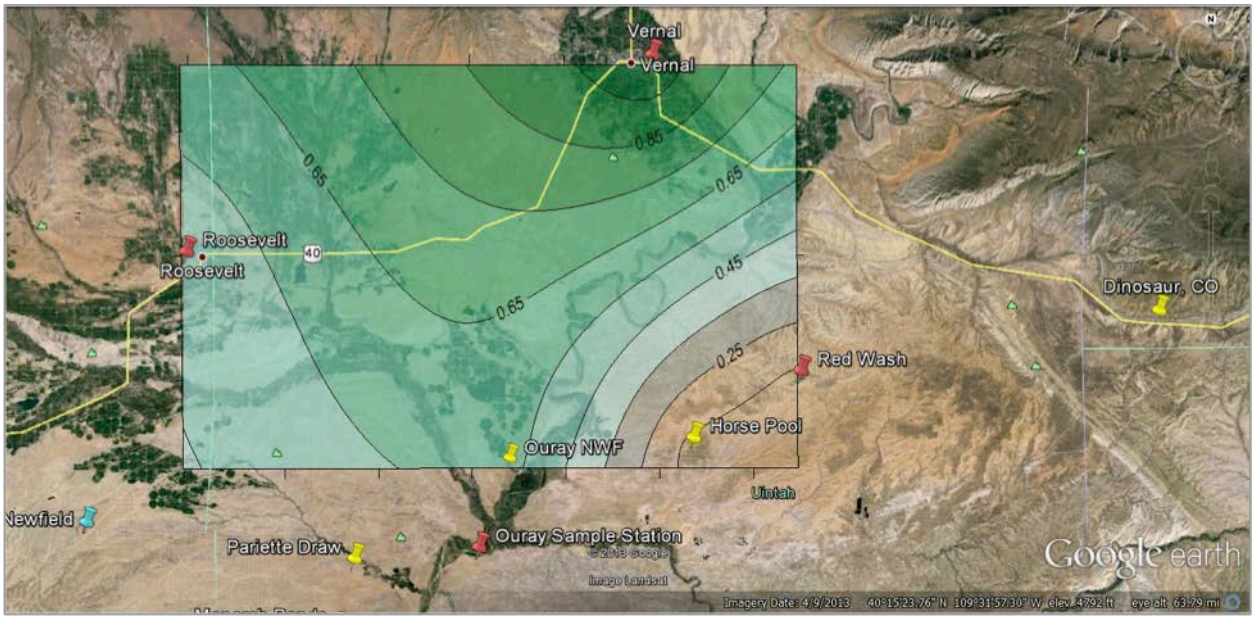

5-57. Contour plot of ambient ammonia concentrations within the Uinta Basin overlaid onto a Google Earth map.

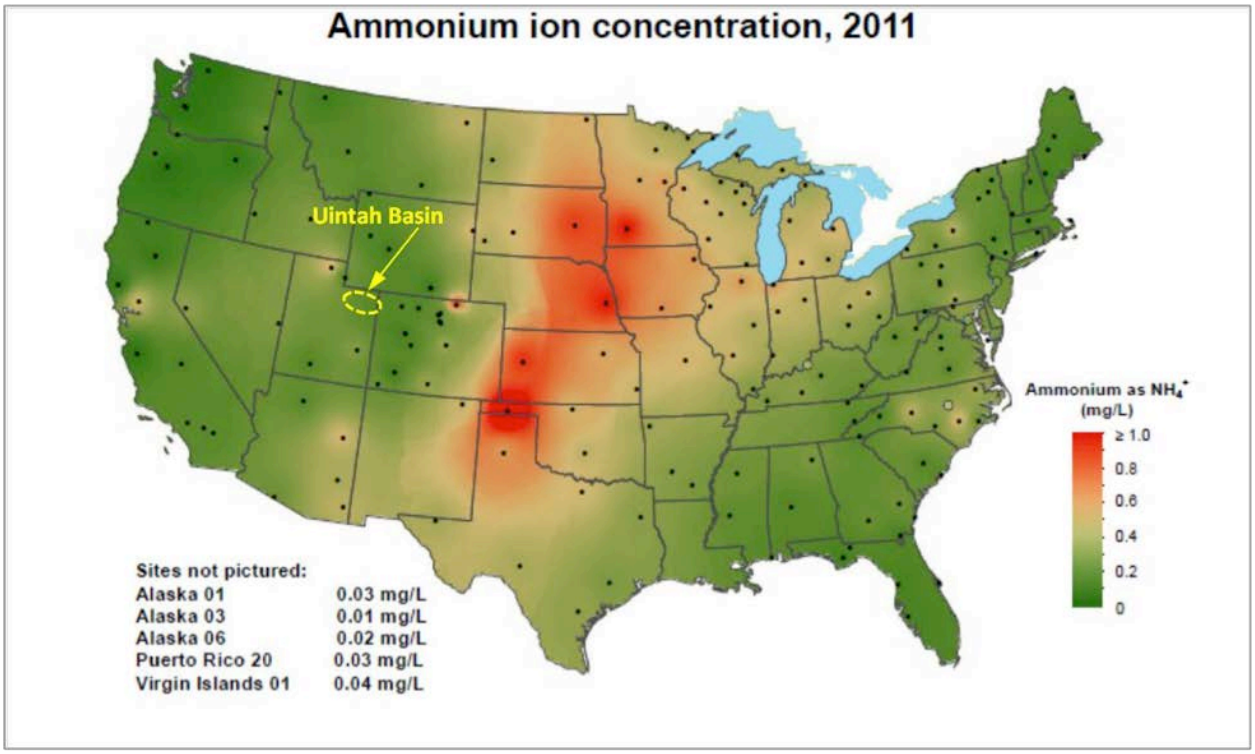

5-58. National ammonium ion (NH_4+) concentrations for 2011 as observed by the National Trends Network (NADP, 2013a).

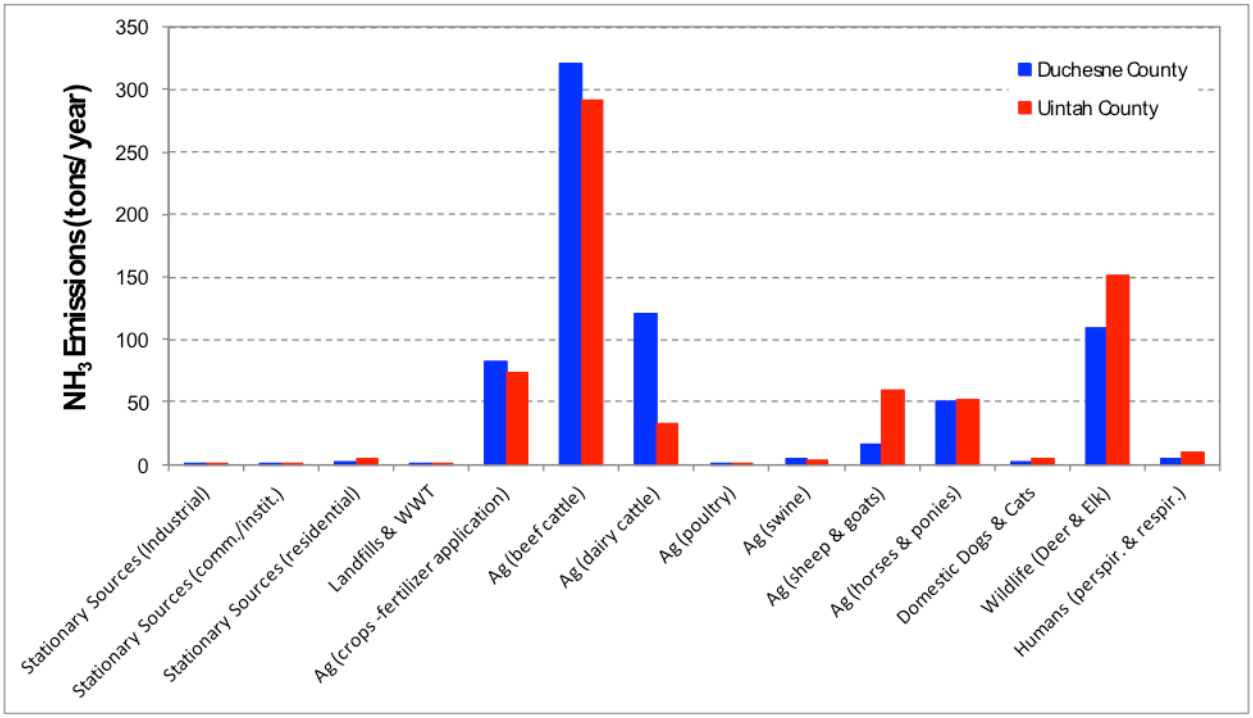

5-59. Estimated annual NH_3 emissions for the two counties making up Utah's Uinta Basin (UDAQ, 2013.)

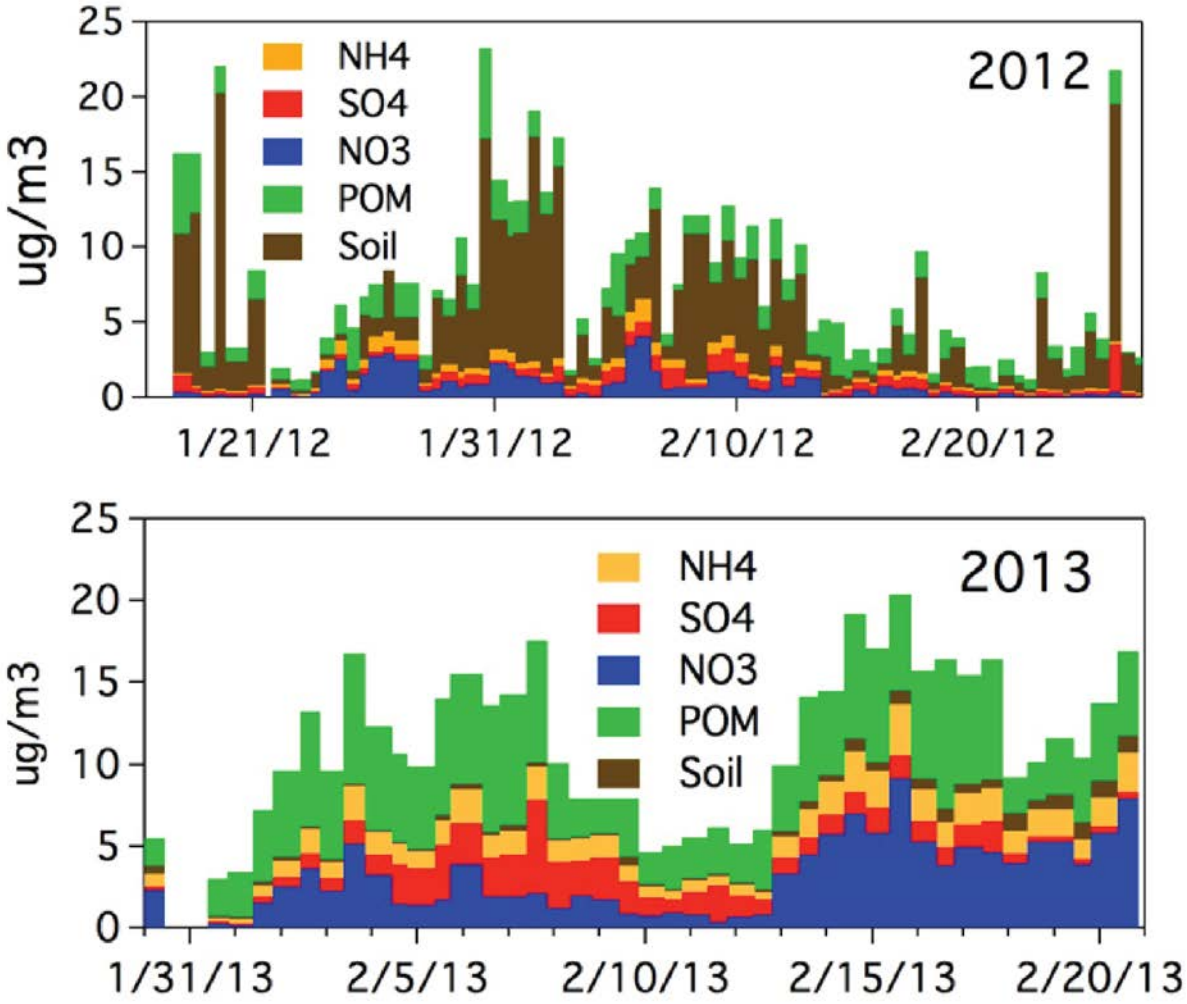

5-60. A comparison of the PM $_{2.5}$ aerosol mass concentrations between 2012 and 2013.

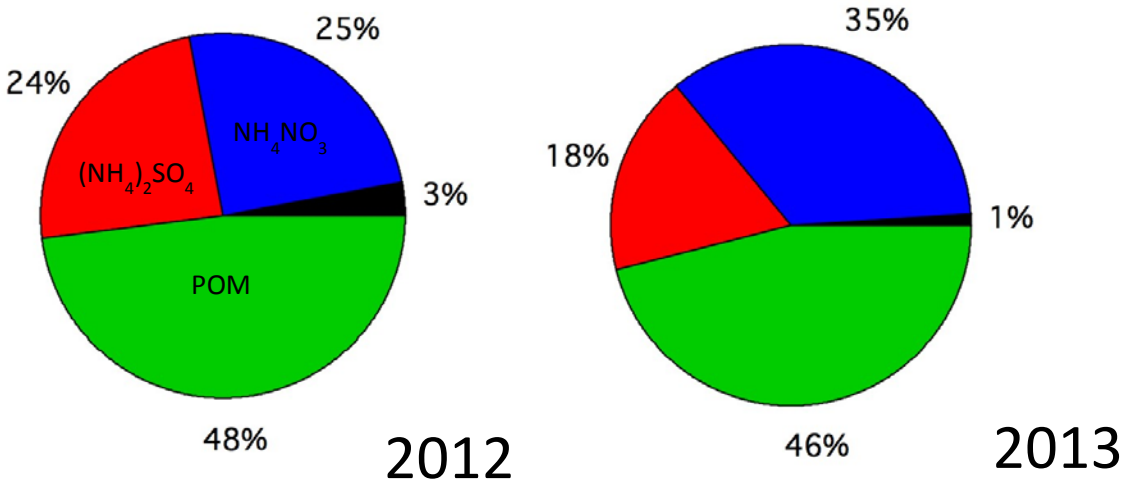

5-61. Mass fractions of the primary sub micrometer aerosol components in 2012 and 2013 (POM-green; $(NH_4)_2SO_4$ -red; and NH_4NO_3 -blue).

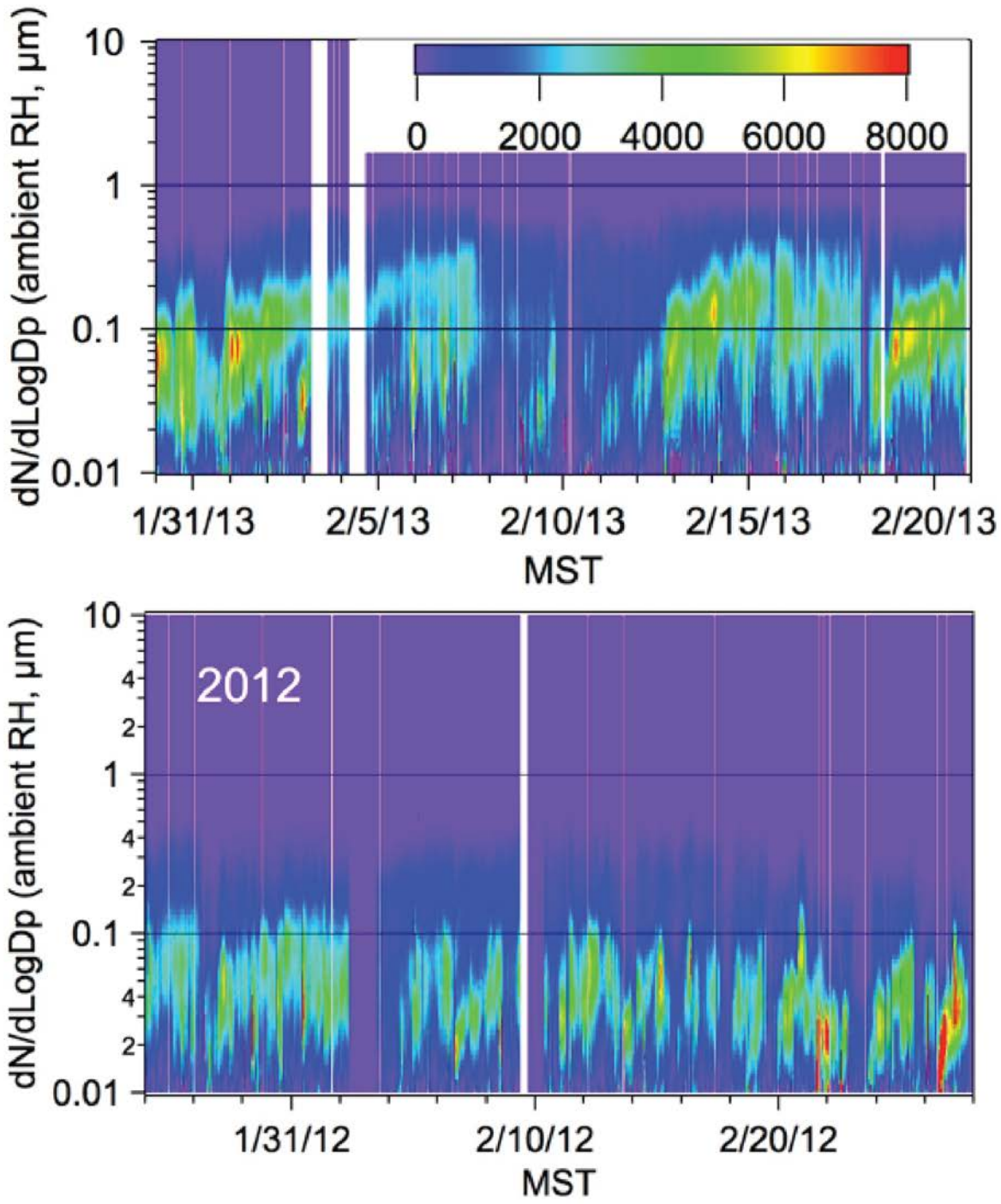

5-62. Aerosol number size distributions at ambient relative humidity in 2012 (bottom) and 2013 (top) showing the larger mean diameter in 2013.

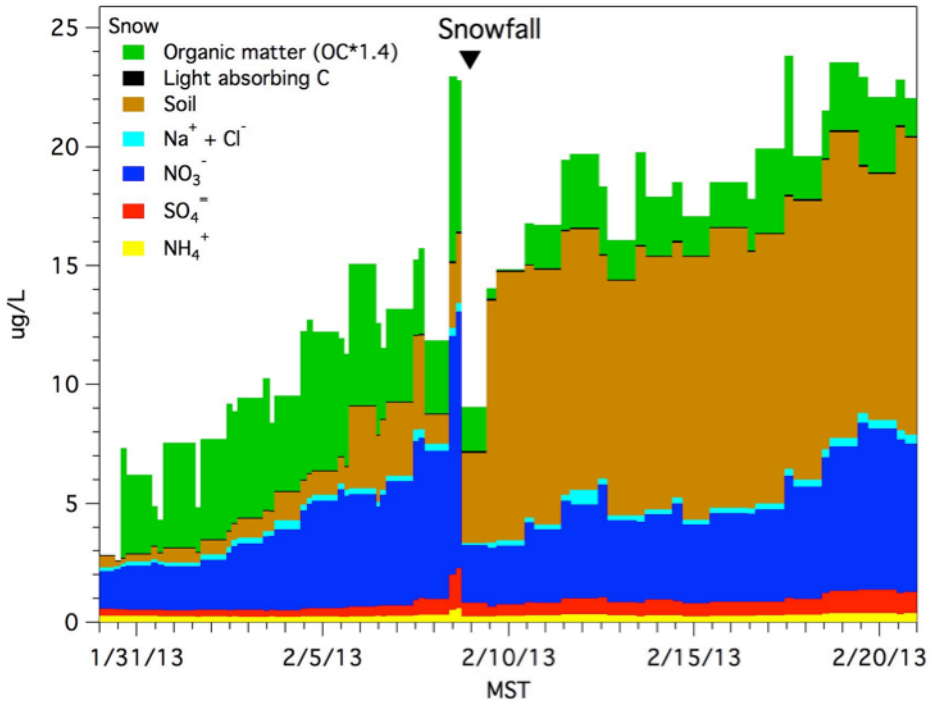

5-63. Inorganic and organic components in surface (0-3cm) snow measured within 1.3 km of Horse Pool in 2013. Nitrate and nitrite (not shown) concentrations increased in the surface snow with time. The snow fall on February 8 covered the surface snow and reduced the measurable inorganic ion concentrations.

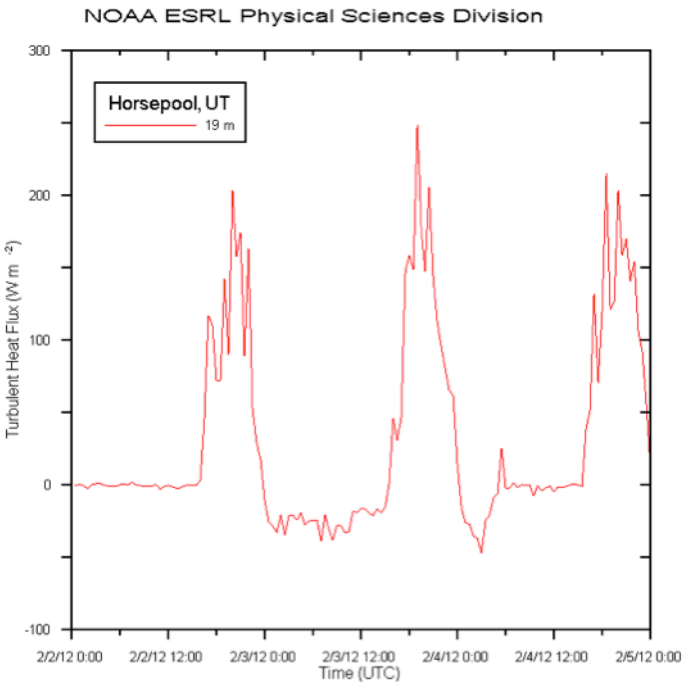

5-64. Typical surface sensible heat fluxes at the Horse Pool meteorological site during UBOS 2013.

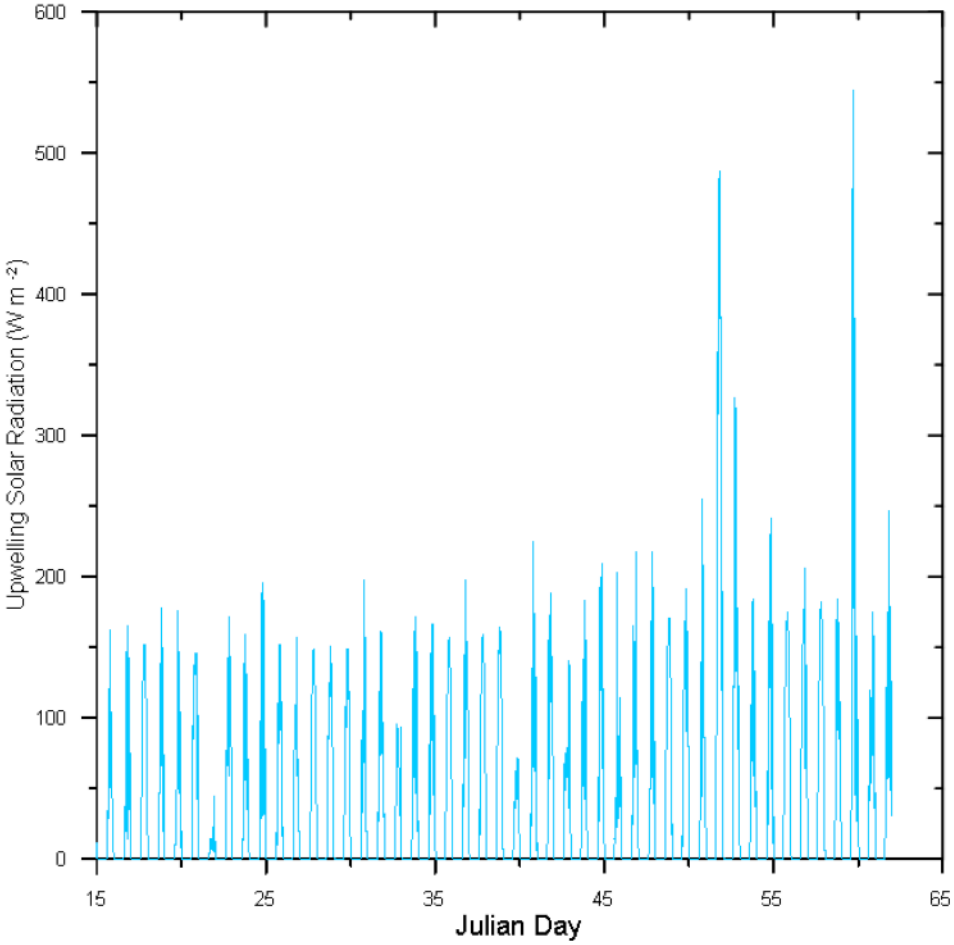

5-65. Upwelling solar radiation measured at Horse Pool during UBOS 2013.

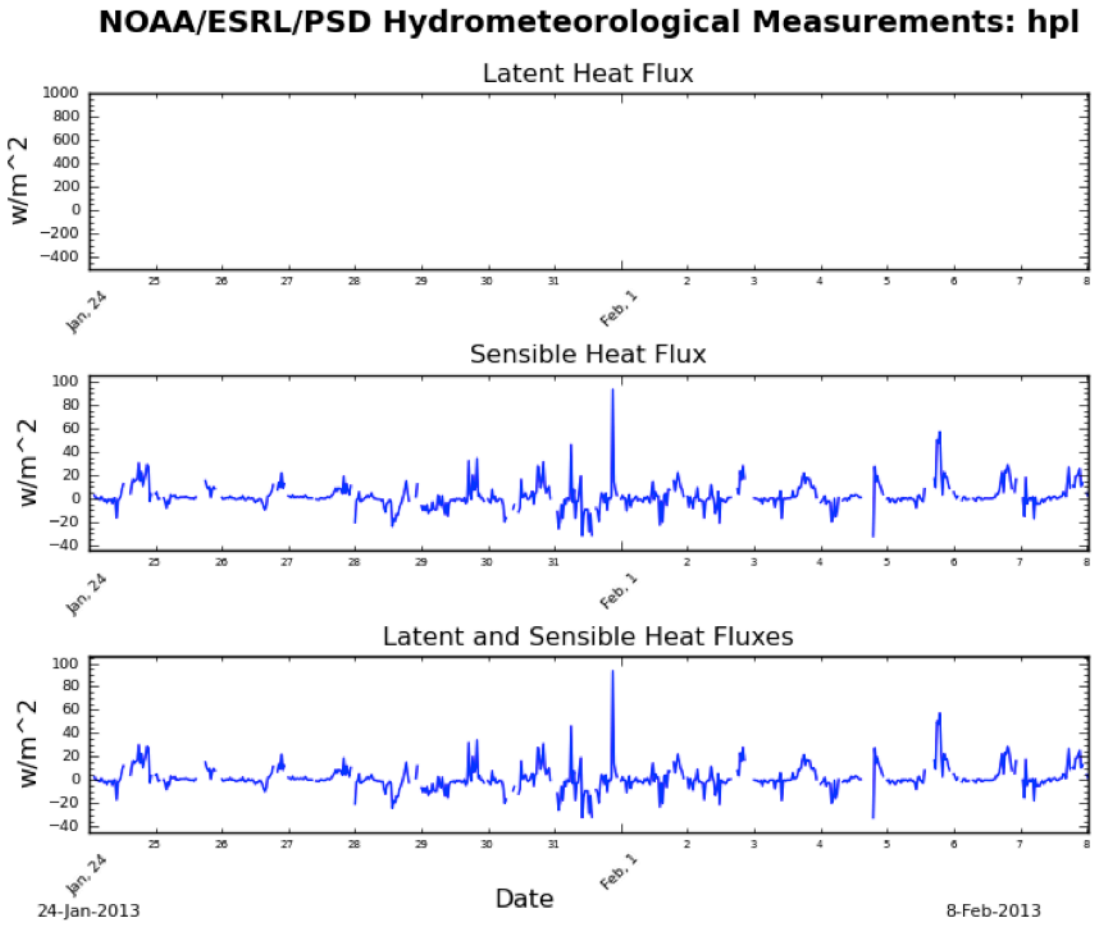

5-66. Heat fluxes measured at Horse Pool during UBOS 2013.

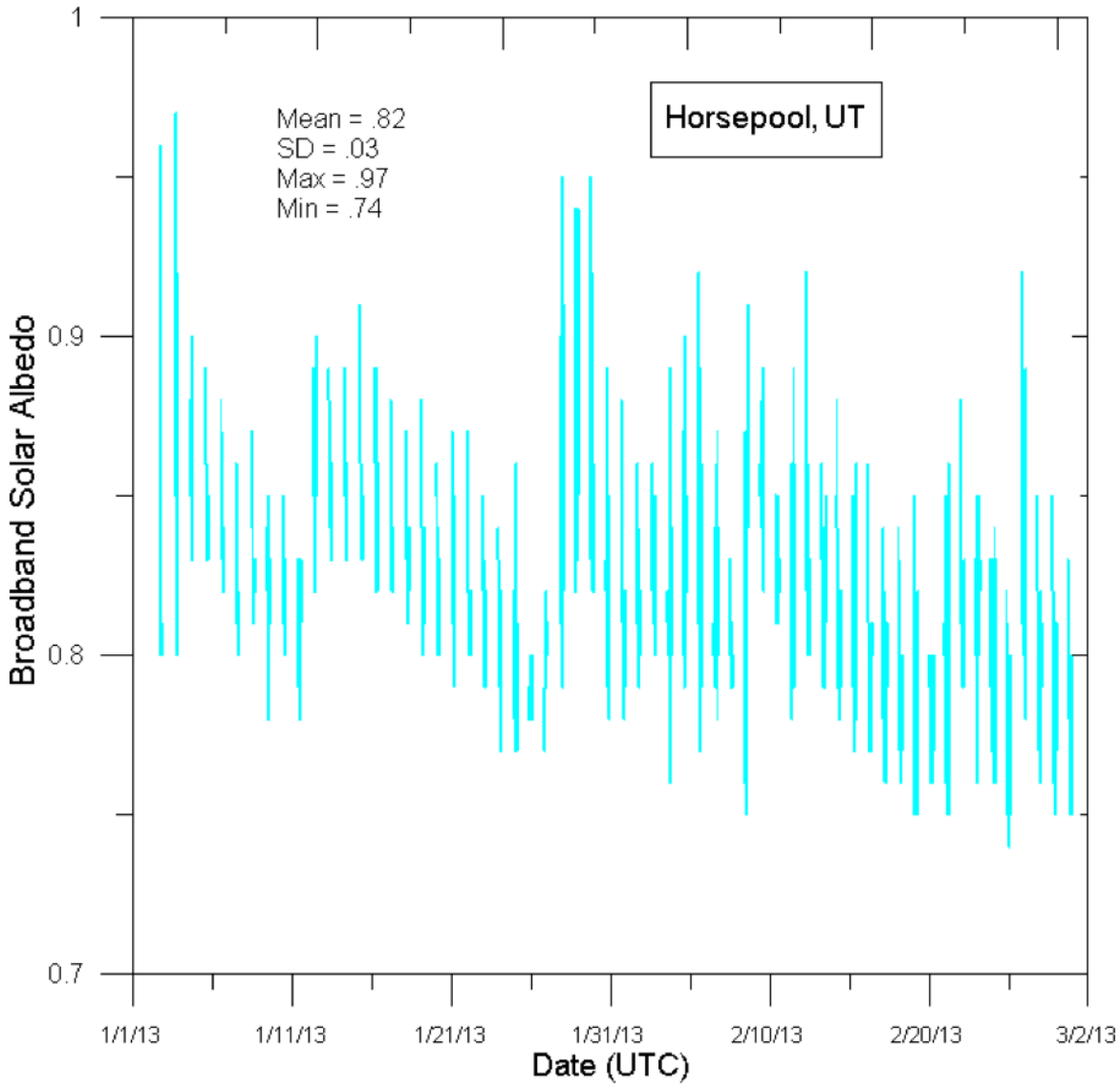

5-67. Broadband solar albedo at Horse Pool during UBOS 2013.

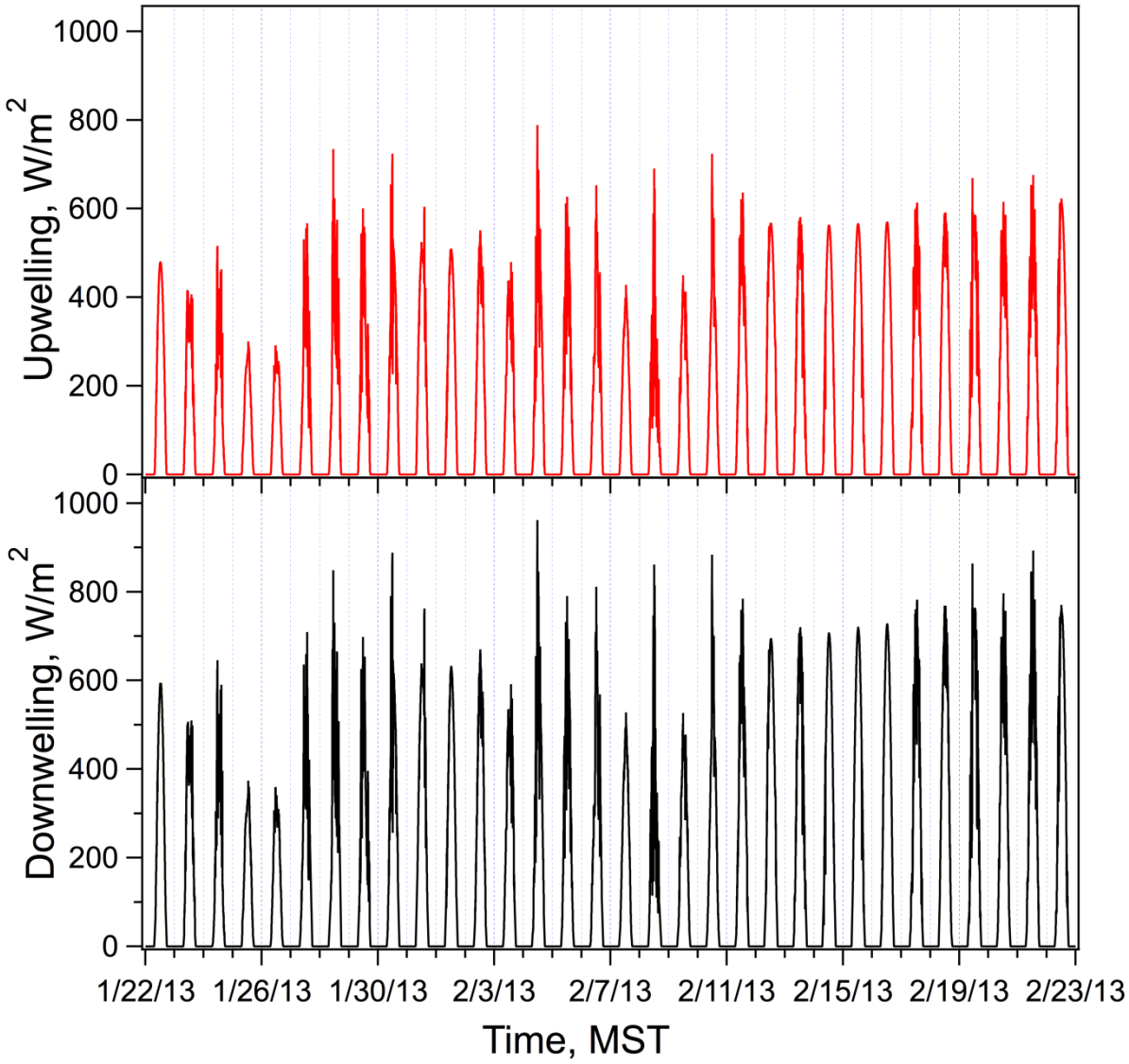

5-68. The downwelling (black) and upwelling (red) solar irradiances measured at Horse Pool during the UBOS 2013 experiment.

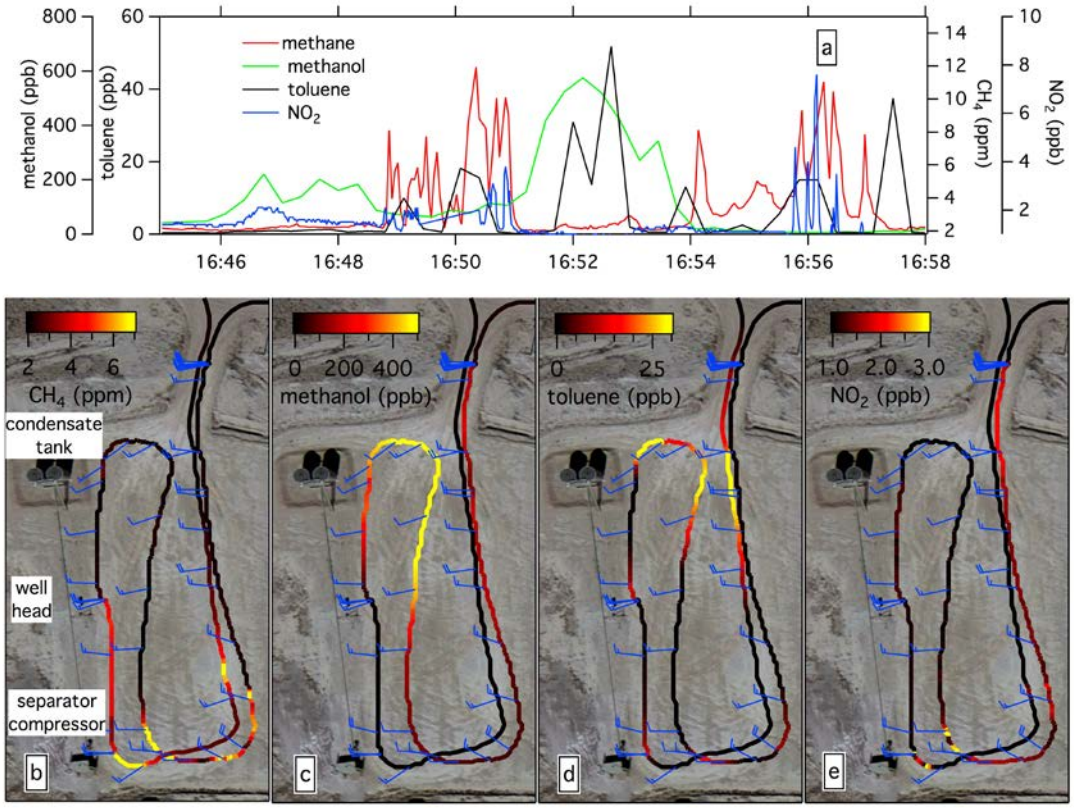

5-69. An example track close to a gas well, color coded by methane (b), methanol (c), toluene (d) and (e) NO_2. The wind barbs indicate prevailing wind direction. The time series during this period is shown in (a).

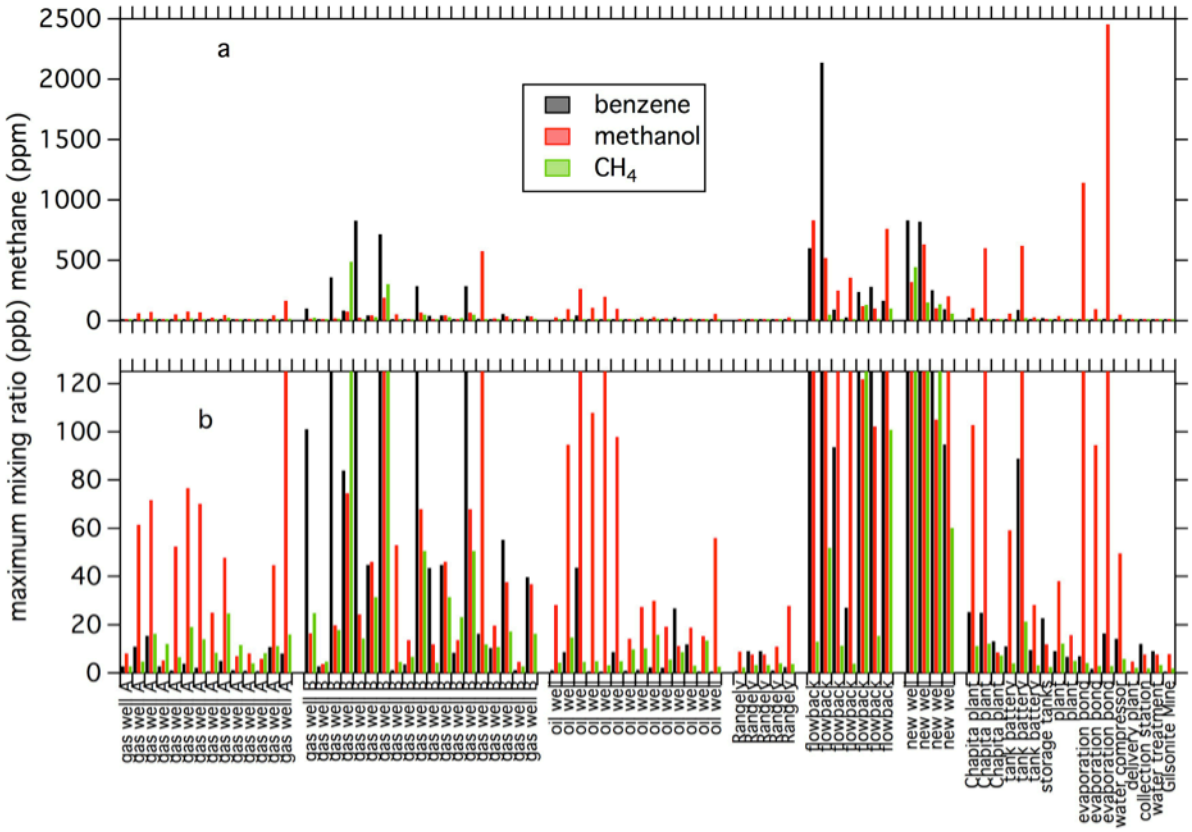

5-70. The maximum mixing ratios of benzene, methanol and methane observed close to the sources in the Uinta Basin and in Rangely, Colorado in both (a) full scale and (b) small scale.

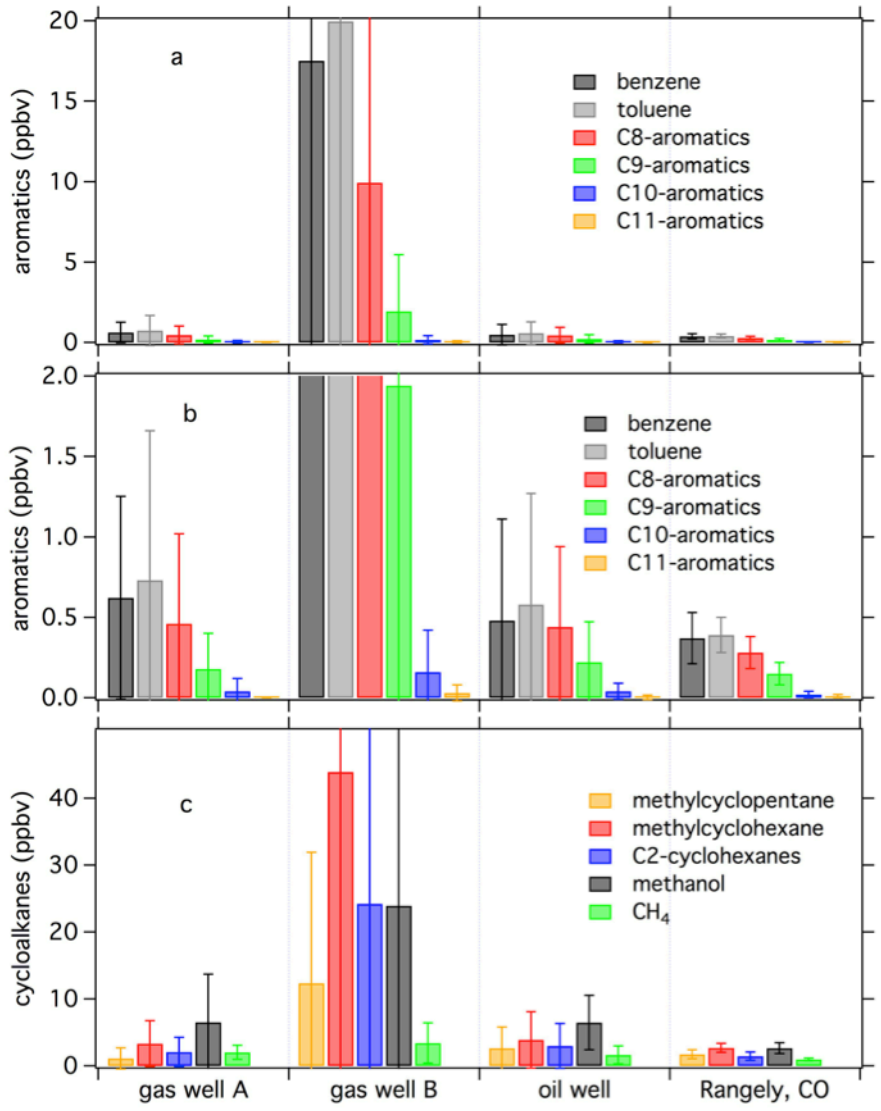

5-71. Average mixing ratios of the VOCs; aromatics, cycloalkanes, methanol and methane) measured near emission sources in the Uinta Basin, averaged for each category of point sources. The error bars are the standard deviation. All concentrations were normalized to an average wind speed of 2 m/s.